Synthesis and characterisation of FeSe superconductors

FCTUC FACULDADE DE CIÊNCIAS E TECNOLOGIA
UNIVERSIDADE DE COIMBRA

Marta Sofia da Costa Henriques

CFisUC, Department of Physics
University of Coimbra

Thesis advisor:
José António de Carvalho Paixão

A thesis submitted for the degree of
Master of Physics

Coimbra, 9th December, 2015

Dedico esta tese às três mulheres da minha vida, que tanto contribuiram para a minha forma de ser: a minha mãe, a minha querida avó Alzira e a minha tia e grande amiga Isabel. Amo-vos muito.

Acknowledgements

I would like to start by thanking my supervisor, Professor José Paixão, for all the help, guidance, patience and friendship during this thesis work.

To Professor Benilde I would like to thank for all the valuable help provided with the sample's sealing and valuable advice.

To Professor João Gil, I would like to thank for all the help provided and sorting out technical issues that came out during this year and for the friendly advice.

To my friends Marina, Mariana, Joana (Blue) and Monique I would like to thank them for the talks, friendship, support and patience during this year and for being the crazy, special friends that they have always been to me.

To Mario and Tiago I would like to thank for the many moments when they spoke nonsense in our conversations. Sometimes were those moments that made me smiling.

To Francisco, many thanks for the whole year of good moments and fellowship.

I also would like to thank Cruz, Eng. Nuno, Emanuel, Adélia and the girls from the Physics Department services. Many times they are kept in oblivion, specially by us students. To them many thanks for the friendship and help provided in many situations since I arrived at this department.

To Pedro, I am sorry for the many coffees I missed and I thank you for all your best patience and for you being such a great friend.

To my parents, thank you for all the support and care.

Support from CFisUC and access to TAIL-UC facility funded under QREN-Mais Centro Project ICT/2009/02/012/1890 is gratefully acknowledged.

Abstract

A study of the phase diagram of the $FeSe_{1-x}$ superconducting compound was performed around the composition 1:1 aiming to determine the best stoichiometry and synthesis conditions that maximise the amount of the superconducting β-FeSe phase and minimise the amount of impurity phases. In this study we used a solid-state synthesis procedure and characterised the samples with a variety of techniques: XRD, SEM/EDS, resistivity and VSM measurements, taking advantage of the new equipment recently installed at the Trace Analysis and Imaging Laboratory-UC. We succeeded in devising a method to obtain polycrystalline samples with a β-phase fraction larger than 90%. The major minority phases are the ferrimagnetic, non-superconducting, δ-FeSe and excess α-Fe that precipitates in the matrix, as the best nominal composition that maximises the β-FeSe phase demands a starting Se deficient composition, $FeSe_{1-x}$. Other observed minority phases are Fe_7Se_8 and Fe_3Se_4. Magnetite and fayalite may also develop in the presence of oxygen. The study of the hysteresis cycles at low temperature shows that the $(\beta + \delta)$-FeSe samples behave like a hard type-II superconductor ($T_{\text{onset}} = 10\,\text{K}$, $T_c = 7.5 - 9.2\,\text{K}$) that obeys the Bean's critical state model as the vortices are pinned in bulk and surface defects of the sample. The H_{c1} critical field extrapolated to 0 K is 330 Oe.

Resumo

Um estudo do diagrama de fases do composto supercondutor $FeSe_{1-x}$ foi realizado em torno da composição 1:1 com o objetivo de determinar a melhor estequiometria e condições de síntese que maximizam a produção da fase supercondutora de β-FeSe e minimizam a presença de outras fases ou impurezas. Neste trabalho utilizámos um método de síntese em fase sólida a partir dos elementos e caracterizámos as amostras com uma variedade de técnicas: XRD, SEM/EDS, resistividade e magnetização VSM, usufruindo do novo equipamento recentemente instalado na plataforma *Trace Analysis and Imaging Laboratory-UC*. Conseguimos desenvolver o método para obter amostras policristalinas com uma fração da fase β superior a 90 %. As fases minoritárias são essencialmente δ-FeSe, que é ferrimagnético e não supercondutor e o excesso de α-Fe que precipita na matriz, pois a melhor composição nominal que maximiza a fase β requer uma composição inicial deficiente em selénio, $FeSe_{1-x}$. Outras fases minoritárias que se encontram nas amostras são Fe_7Se_8 e Fe_3Se_4. Magnetite e fayalite podem também ocorrer na presença de oxigénio. O estudo dos ciclos de histerese a baixa temperatura mostra que as amostras ($\beta + \delta$)-FeSe se comportam como supercondutores duros do tipo II ($T_{\text{onset}} = 10\,\text{K}$, $T_c = 7.5 - 9.2\,\text{K}$) que obedecem ao modelo do estado crítico de Bean pois os vórtices ancoram em defeitos no volume e na superfície da amostra. O campo crítico H_{c1} extrapolado para 0 K é de 330 Oe.

Contents

List of figures **xiii**

List of tables **xix**

1 Introduction **1**

2 Iron-based superconductors **5**
2.1 Introduction to Superconductivity 5
2.2 The FeSe superconductor 7

3 The Fe-Se phase diagram **15**

4 Experimental Methods **21**
4.1 Synthesis 21
4.2 Structural characterization methods 22
4.2.1 Introduction 22
4.2.2 Elementary theory of XRD 23
4.2.3 XRD equipment 25
4.3 Scanning Electron Microscopy (SEM) 28
4.3.1 Introduction 28
4.3.2 Fundamental principles 29
4.3.3 Interaction of accelerated electrons with a sample 30
4.3.4 Description of the microscope used 34
4.4 Electrical and magnetic characterisation methods 39
4.4.1 Physical Properties Measurement System (PPMS) 39
4.4.2 Resistivity measurements 42
4.4.3 Magnetometry measurements 44

5 Results **47**
5.1 Exploratory work of the phase diagram 47

5.1.1 Synthesis 47
5.1.2 XRD analysis 48
5.1.3 Resistivity 53
5.1.4 Magnetic hysteresis cycles 56
5.1.5 Meissner effect 57
5.1.6 Critical field 60
5.1.7 The "dolphin effect" 62
5.2 Fine-tuning the synthesis of β-FeSe 65
5.2.1 Synthesis 65
5.2.2 XRD analysis 65
5.2.3 Resistivity 69
5.2.4 SEM/EDS 69
5.2.5 Magnetisation measurements 74
5.3 Results from sample annealing 77
5.3.1 XRD analysis 77
5.3.2 Resistivity 81
5.3.3 Magnetisation measurements 81

6 Conclusions and future work **85**

References **87**

Appendix A **91**

List of figures

1.1 Crystal structure of β-FeSe [7]. 2
1.2 Iron-based superconductors families [8]. 3

2.1 Magnetic phase diagram of (a) Type-I superconductors and (b) Type-II superconductors. 6
2.2 Iron-based family of superconducting compounds [9]. 8
2.3 Temperature dependence of electrical resistivity of $FeSe_{0.88}$. The left inset shows the resistivity measurement in magnetic fields (H) of 0, 1, 3, 5, 7, and 9T below 12 K. T_c decreases linearly with increasing magnetic field. The right inset displays the temperature dependence of upper critical field (Hc_2), with the fit shown in blue [7]. 8
2.4 Phase diagram of Fe_xSe close to the stoichiometric 1:1 composition according to McQueen *et al.* [10]. 9
2.5 Mössbauer spectra at 295 and 5 K for pure and poisoned samples by oxygen exposure. The pristine samples show no sign of magnetic order [10]. 10
2.6 (a) The structure of tetragonal iron selenide consists of two-dimensional layers of edge-sharing Fe-Se tetrahedra. (b) Superconducting $Fe_{1.01}Se$ has an orthorhombic distortion, indicated by the splitting of some peaks in SXRD (arrows), but non-superconducting $Fe_{1.03}Se$ does not. (c) On cooling, $Fe_{1.01}Se$ undergoes a twisting of the tetrahedra, splitting the Fe-Fe distances into two distinct sets. Non-superconducting $Fe_{1.03}Se$, in contrast, shows no transition by SXRD [11]. 11
2.7 Specific heat as a function of applied magnetic field of β-FeSe [12]. 12
2.8 (T-P) phase diagram of β-FeSe [13]. 12
2.9 ^{77}Se NMR spin-lattice relaxation rate T_1^{-1} in β-FeSe [14]. 13

3.1 Fe-Se phase diagram [21]. 17

3.2 (a) View of a transverse cross-section of a wire before annealing; (b) SEM picture showing details of the FeSe core after heat treatment on polished transverse cross-sections of samples used for the synchrotron runs - FeSe phase is clearly observed as well as large amounts of Fe [22]. 17

3.3 Diffraction patterns collected (a) during the heating ramp at: a: 25 °C, b: 190 °C, c: 364 °C, d: 394 °C and e: 486 °C ; (b) during the cooling ramp: $\beta = \beta$-FeSe, $\delta = \delta$-FeSe [22]. 18

3.4 Temperature dependence of the integrated intensity of selected diffraction peaks during heating at 2 °C/min [22]. 19

4.1 TERMOLAB furnace. 22

4.2 Illustration of Bragg reflection from a set of parallel planes [24]. 24

4.3 Bruker AXS D8 ADVANCE diffractometer. 26

4.4 Bragg-Brentano geometry. 27

4.5 Resolution function of the D8 diffractometer measured with a corundum sample. 28

4.6 SEM images of corroded metal acquired using backscattered electrons (left) and secondary electrons (right) [26]. 31

4.7 Inner shell ionisation and subsequent de-excitation by electron transitions. The difference in energy from an electron transition is expressed by the emission of an Auger electron or by the emission of a characteristic X-ray photon [27]. 32

4.8 Possible electron transitions generating X-ray emission [29]. . . . 33

4.9 Picture of the TESCAN VEGA3 SBH SEM equipment used in this work. 35

4.10 VEGA3 SEM cross section and schematic representation of the optical elements [30]. 37

4.11 Scheme of the deflection system inside the final lens. Working distance is represented here by W [27]. 37

4.12 PPMS DynaCool magnetometer. 39

4.13 The DynaCool Cryostat showing the components of the Cryostat, Chamber Temperature, and Magnetic Field Control Systems [31]. 41

4.14 Scheme of a circuit for the 4-wire mode [32]. 42

4.15 Left: $G(z)$ function for coils with radius a_0, separate by $2z_0$, in the gradiometer configuration. In the case of DynaCool VSM, $z_0 = \sqrt{3}a_0/2$. [36]; Right: View of a sample (red) positioned in the VSM gradiometer with the large bore coil set shown as an example. Below is shown the coil response function (sample's reported magnetic moment as a function of its location in the coils) [37]. 45

5.1 Diffraction patterns of samples #1, #2 and #3, showing the phases and respective percentage determined by the Rietveld method. . 49

5.2 Diffraction pattern of sample #2, after one month of air exposition. 50

5.3 Diffraction pattern of sample #1, after the second heating/cooling cycle. 53

5.4 Puck containing a FeSe sample showing the 4-point contacts made between the sample and puck using a gold wire and silver paint. 54

5.5 Resistivity measurement performed from 1.8 to 300 K for sample #2. The inset shows the data between 1.8 and 15 K. 54

5.6 Temperature derivative of the resistivity using a numerical 5-point centred formula. It shows (a) a large peak at $T_c = 9.2$ K and a small peak at 26.5 K and (b) a small broad peak at ~ 120 K. . . 55

5.7 Magnetic hysteresis cycle measured at 1.8 K for sample #1. . . . 56

5.8 Magnetic hysteresis cycle measured at 1.8 K for sample #2. 57

5.9 Magnetic hysteresis cycle measured at 1.8 K for sample #3. 57

5.10 Magnetic hysteresis cycle measured at 100 K for sample #3. . . 58

5.11 From top to bottom: ZFC and FC curves for samples #1, #2 and #3 showing the Meissner effect. 59

5.12 Low-field magnetic hysteresis cycle of sample #3 at 1.8 K. . . . 60

5.13 Low-field magnetic hysteresis cycle of sample #3 from 1.8 K to 6.5 K. 61

5.14 Critical field H_{c1} as function of temperature for sample #3. 61

5.15 Hysteresis cycle of sample #3 measured up to 10 kOe at 1.8 K. . 62

5.16 Sequence of funny-looking hysteresis cycles showing the transformation into normal cycles with increasing temperature. 63

5.17 Diffraction patterns of samples #1 and #2, showing the phases and respective percentage determined by the Rietveld method (run #1). 66

5.18 Diffraction patterns of samples #3 and #4, showing the phases and respective percentage determined by the Rietveld method (run #1). 67
5.19 Diffraction patterns of samples #5 and #6, showing the phases and respective percentage determined by the Rietveld method (run #1). 68
5.20 Weight percentage of the phases present in the six samples of run #1 as function of the nominal composition. In addition, the curve of the β over δ ratio is also shown. 69
5.21 Resistivity curves in the temperature range from 1.8 to 15 K in samples #2 (top) and #5 (bottom). 70
5.22 SEM images of (a) sample #2 at the surface and (b) sample #6 in its inside, taken with a magnification of 1kx. 71
5.23 SEM images of (a) sample #2 at surface, (b) sample #4 and (c) sample #6 in its inside, showing the size of particles that covers a range from ~ 4 to $\sim 8\,\mu m$. 72
5.24 EDS mapping of: (a) sample #1 and (c) sample #4 at its inside; for the other samples, #2, #5 and #6 (with label b, d, e) the mapping was performed at the surface. In sample #4 one can visualise how the particles organise in depth. 73
5.25 From top to bottom: ZFC and FC curves for samples #2, #4 and #5 of run #1. 75
5.26 Full hysteresis cycles of samples #1 to #6 of run #1, measured at 130 K. 76
5.27 Saturation magnetic moment in μ_B per formula unit of samples #1 to #6 of run #1. 76
5.28 Diffraction patterns of samples #1 and #2, showing the phases and respective percentage determined by the Rietveld method (run #2). 78
5.29 Diffraction patterns of samples #3 and #4, showing the phases and respective percentage determined by the Rietveld method (run #2). 79
5.30 Diffraction patterns of samples #5 and #6, showing the phases and respective percentage determined by the Rietveld method (run #2). 80
5.31 From top to bottom: Resistivity measurements on samples #4, #5 and #6, run#2. 82

5.32 From top to bottom: ZFC and FC curves of samples #1 and #6 after annealing, run #2. 83

A.1 Poster presented at the 41st Conference on Phase Equilibria, Coimbra. 92

List of tables

5.1 Summary of the results from the Rietveld refinement of the XRD data for sample #1 to #3 after the preliminary run in furnace. D, z, o, GOF and R_{wp} stand for crystallite size, fractional coordinate, site occupancy factor, goodness of fit and weighted pattern reliability factor, respectively. 51
5.2 Summary of the results from the Rietveld refinement of the XRD data for sample #1 after annealing and sample #2 after one month exposure to air. 52
5.3 Brief summary of the results from the Rietveld refinement of the XRD data for sample #1 to #6, run #1. 67
5.4 Comparison of the β-FeSe phase content of the samples before (run#1) and after (run#2) annealing. 77
5.5 Brief summary of the results from the Rietveld refinement of the XRD data for sample #1 to #6, run #2. 81

Chapter 1

Introduction

The first iron-based compound having superconducting properties (LaFeOP) was discovered in 2006 by Kamihara and his collaborators when studying its semiconductor properties [1].Two years later, a critical temperature of 26 K was attained in $La[O_{1-x}F_x]FeAs$ ($x = 0.05 - 0.11$) [2], and a superconductivity up to 55 K in $Sm[O_{1-x}F_x]FeAs$, another compound of the same family [3]. This temperature is beyond the upper limit of $T_c = 25$ K that was believed to exist for conventional superconductivity, which triggered the attention of the high-T_c superconductivity community. Moreover, many scientists had dismissed the possibility of iron-based superconductivity because the large magnetic moment of iron was believed to be strong enough to disrupt the pairing of electrons (Cooper pairs) responsible for superconductivity. Such an unexpected discovery led to many worldwide attempts to synthesise and characterise materials with a similar structure based on the same FeAs atomic planes believed to be responsible for the superconductivity in iron-based superconductors. Subsequent works were performed revealing superconductivity in other iron-based compounds such as the AFe_2As_2 (with A standing for an alkali or earth alkaline element) [4, 5], LiFeAs [6], etc., called iron-based pnictides because of the presence of a pnictogen element (an element of the group 15 of the periodic table). The discovery of such a high-T_c in this new family of compounds was a celebrated proof that high-temperature superconductivity was not exclusive of Cu oxides.

In the same year of 2008, a group searching for the existence of superconductivity in other similar Fe based compounds succeeded in discovering superconductivity in a different compound, the PbO-type structure α-FeSe[1] (Fig.1.1) [7], with a transition temperature of 8 K. Since then, several families of iron-based superconductors have been discovered and are still under study, being mainly

[1]later the PbO-type structure α-FeSe started to be called β-FeSe

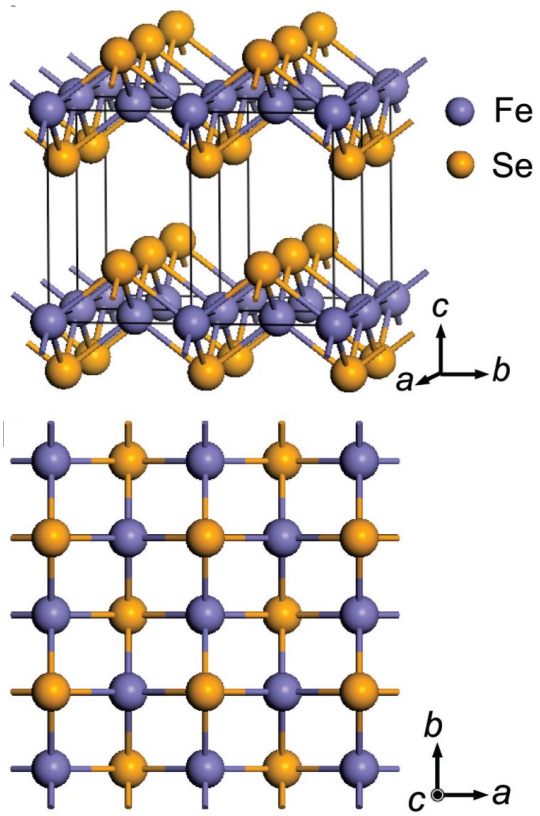

Fig. 1.1 Crystal structure of β-FeSe [7].

categorised into '11' [7], '111' [6], '122' [4, 5] and '1111' [2] systems according to their crystal structure, where the number denotes the atomic ratio in constituting the compound (Fig.1.2). The FeSe itself shows properties (electronic, magnetic and structural) relevant to superconductivity similar to those in iron-based pnictides and, similarly, doping these compounds can affect their superconducting properties. What made this compound so attractive and captured all the attention to it, was its deceptively simple layered structure, each layer based on the simple motif of $FeSe_4$, as depicted in Figure1.1. FeSe, with no intercalating plane of atoms between the FeSe layers, is the simplest material in the iron-based superconductors family, providing a great opportunity to fully understand the mechanism of superconductivity in these compounds. It is believed that the superconducting process takes place in FeX tetrahedral layers (X=pnictogen or chalcogen) and that the intercalate layers, that exist in the 111, 122 and 1111 systems are inert, which makes the FeSe series (where Se can be replaced by other chalcogens, such as S or Te) the most important compounds to be studied, as they may have the key to uncover some mysteries of the high temperature superconductivity. Unfortunately, the synthesis of good quality samples of FeSe

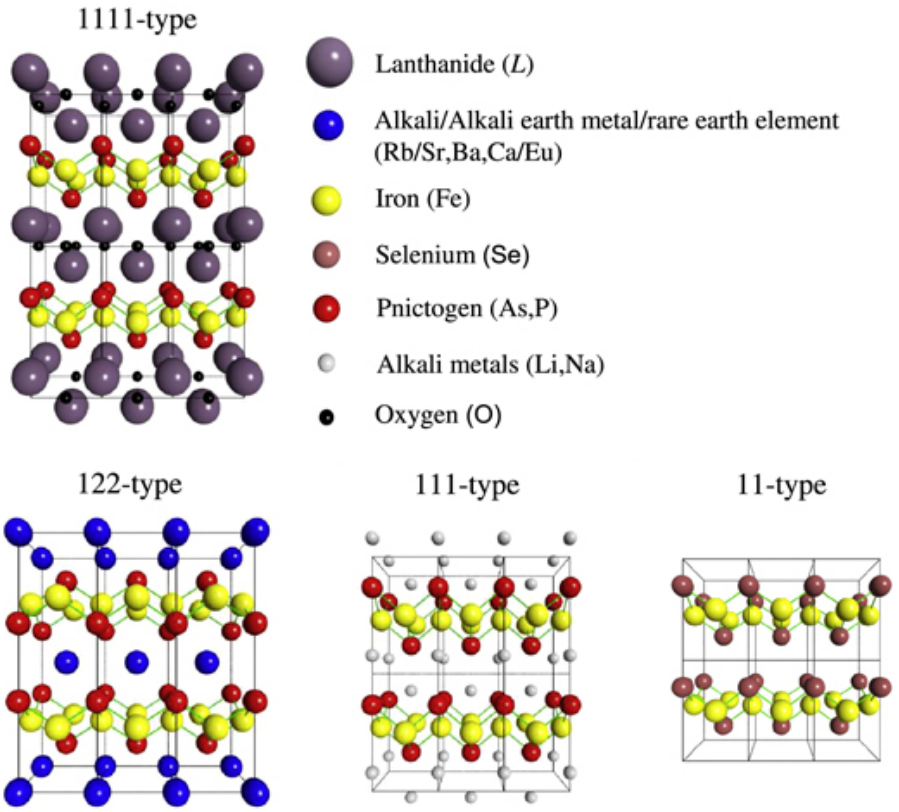

Fig. 1.2 Iron-based superconductors families [8].

compounds is not without difficulties and challenges, because of the existence of several polymorphic and closely related non-superconducting phases with similar composition in the Fe-Se phase diagram. Therefore, devising the best synthetic method to produce FeSe superconducting materials needs a closer look at the phase diagram of this system, around 50% : 50% atom composition. Indeed, even small deviations from the optimal composition as well as oxidation problems have been reported as detrimental to the superconducting properties, whereas doping with some other elements might enhance T_c. This is also the motivation for this thesis project: the synthesis of FeSe superconductors, by the solid-state method, which allow us to obtain polycrystalline samples, and its further characterisation by Powder X-ray Diffraction, Scanning Electron Microscopy and by electrical and magnetic measurements performed on a magnetometer, taking the advantage of using the equipment of the new analytical platform Trace Analysis and Imaging Laboratory-UC, TAIL-UC, from University of Coimbra.

This thesis is structured as follows: in the second chapter, we present some theoretical background for superconductivity and the most general concepts of

unconventional superconductivity, present in iron-based compounds. The third chapter contains a discussion of the Fe-Se phase diagram. Then we proceed to a description of the experimental methods, starting with the synthesis procedure and later with the characterisation methods, the equipment used in this work and its operational principle. Further the discussion of our results is presented and finally we draw some conclusions and prospects for future work.

Chapter 2

Iron-based superconductors

2.1 Introduction to Superconductivity

Superconductivity is a phenomenon experienced by some materials, occurring at temperatures below a given critical temperature, where the electrical resistance drops to zero and the material expels magnetic fields from its inside. This effect, called the Meissner-Ochsenfell effect, states that a magnetic field cannot penetrate into a superconductor, when its temperature is below the transition (or critical) temperature. In the superconducting state, when the material is exposed to a magnetic field, non-dissipative surface currents are generated in order to cancel the magnetic field in the interior. For superconductors with a critical temperature above the temperature of the liquid nitrogen, the Meissner-Ochsenfell effect can be demonstrated by putting an initially stationary magnet over the superconductor and observe the former being repelled by the latter as it is cooled through the critical temperature. The observation of persistent currents is a proof that these superconducting currents do not dissipate energy so that the current never decays. As stated, in the presence of an applied magnetic field, surface screening currents are formed to cancel the field inside the sample. When the applied field is large enough, it becomes energetically advantageous for the sample to go back to its normal state. The field penetration depends on the geometry of the sample, but even for the simplest geometry (samples with a cylindrical shape placed with their axes parallel to the applied field) we can distinguish two types of behaviour that gives origin to the characterisation of superconductor materials as being of Type-I or Type-II (Fig. 2.1):

- In Type-I superconductors, for an applied field below a certain maximum value (the critical field $H_c\,(\mathrm{T})$) there is no penetration of flux. When that value is exceeded, the entire sample reverts to the normal state with the

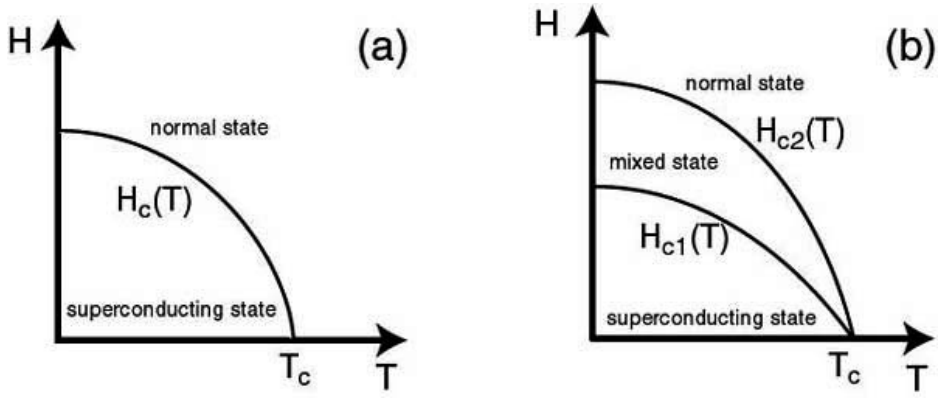

Fig. 2.1 Magnetic phase diagram of (a) Type-I superconductors and (b) Type-II superconductors.

occurrence of total field penetration and, simultaneously, the reappearance of resistivity.

- In Type-II superconductors we need to take into account two critical fields, H_{c1} and H_{c2}, with $H_{c1} < H_{c2}$. For an applied field higher than H_{c2} value, the sample behaves like the Type-I, with the change to the normal state and total field penetration. When the value of the applied field is between H_{c1} and H_{c2}, there is a partial penetration of flux and the sample develops a mixed (Shubnikov) state , where both normal and superconducting regions coexist. In that situation the partial penetration of flux is in the form of thin filaments, named vortices. Inside the vortices, the magnetic field is high and there is no superconductivity; outside its core, the material still remains superconductor. The Meissner effect can be described by the *phenomenological* London equation relating the superconducting current density vector inside a superconductor, $\vec{j}_s$, to the vector potential $\vec{A}$:

$$\vec{j}_s = -\frac{n_s e^2}{m}\vec{A} \tag{2.1}$$

where n_s is the density of superconducting carriers, and e and m are the charge and mass of an electron, respectively. The explanation of superconductivity relies ultimately in quantum mechanics. A weak interaction between electrons mediated by an exchange of virtual particles like phonons binds pair of electrons together that behave as a boson particle. The coherent state of the boson particles (Cooper pairs) that condensate in a common wave function explains the superconducting current, as the many-body state is very stable against any perturbation field

such as that of scattering by impurities, phonons, etc. The macroscopic electron current arising from such quantum phenomenon also explains the Meissner effect and the beautiful coherent effects observed in superconductors, e.g., superconducting tunnelling junctions and Superconducting Quantum Interference Devices (SQUIDs). Such superconducting devices are found today in many technological applications. The mechanism of pairing of the electron Cooper pairs and the symmetry of the macroscopic wave function are still a matter of debate for many superconductors.

Superconductivity was discovered in 1911 by Kamerlingh Onnes while studying the low-temperature properties of Hg. Since then, many elements and compounds have been found to become superconducting at a sufficiently low temperature. Even if superconductivity is not a rare property, most superconductors only exhibit this property at cryogenic temperatures, the exception being the most celebrated high-temperature ceramic compounds for which T_c lies above the boiling point of liquid nitrogen.

The current standard theory of superconductivity relies on a phonon-exchange mechanism to bind the Cooper pairs in a *s*-wave function. It was formulated by Bardeen, Cooper and Schrieffer in 1957 and is known as BCS theory. Broadly speaking, superconductors that do not fit into this theory, either because the mechanism is likely not phonon-based or because the symmetry of the wave function of the Cooper pairs has a higher angular momentum are named unconventional superconductors.

2.2 The FeSe superconductor

In the family of iron-based superconductors, FeSe plays a special role because of its simple crystal structure that is the basic building-block of all iron-based superconductors (Fig. 2.2). A simple structure is of course ideal for both experimental and theoretical studies. β-FeSe is a Type-II superconductor with a T_c of $\sim 8\,\mathrm{K}$ (at ambient pressure). The estimated upper critical field, H_{c2}, determined from the measurement of the resistivity curves of this material under an applied magnetic field is 16.3 T, extrapolated to 0 K (Fig. 2.3) [7].

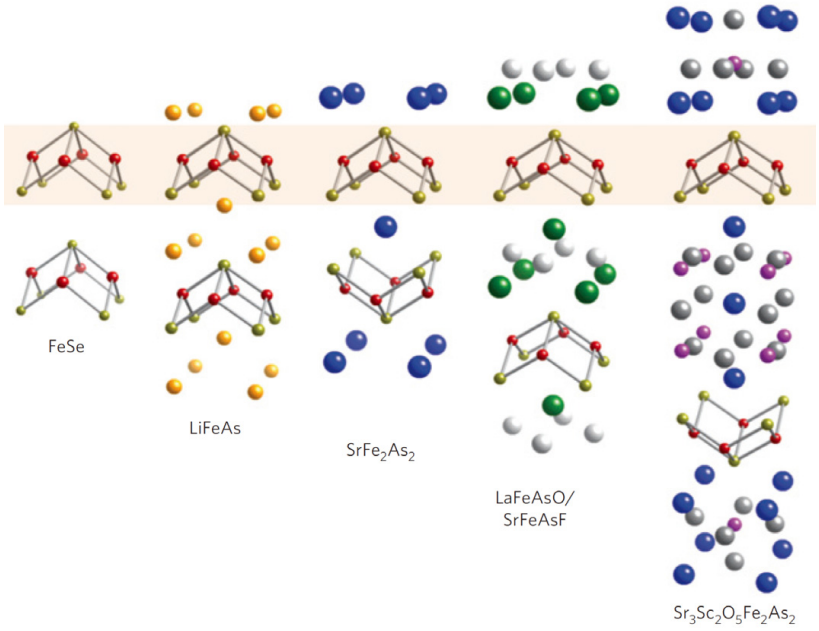

Fig. 2.2 Iron-based family of superconducting compounds [9].

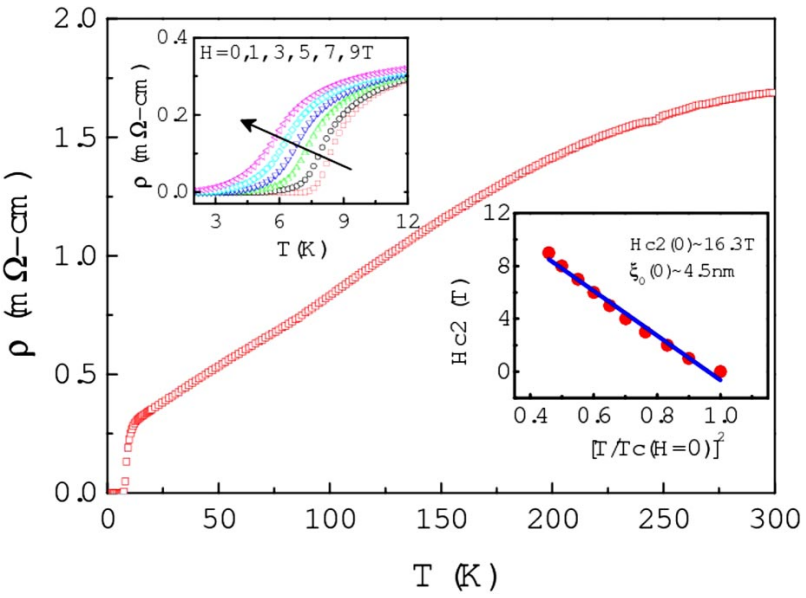

Fig. 2.3 Temperature dependence of electrical resistivity of $FeSe_{0.88}$. The left inset shows the resistivity measurement in magnetic fields (H) of 0, 1, 3, 5, 7, and 9T below 12 K. T_c decreases linearly with increasing magnetic field. The right inset displays the temperature dependence of upper critical field (Hc_2), with the fit shown in blue [7].

An observation made by many authors, is that the superconducting phase occurs only in samples prepared with intentional Se deficiency. Moreover, it appears that tetragonal β-phase exists only in a narrow composition with slight Se deficiency or Fe excess (Fig. 2.4) [10].

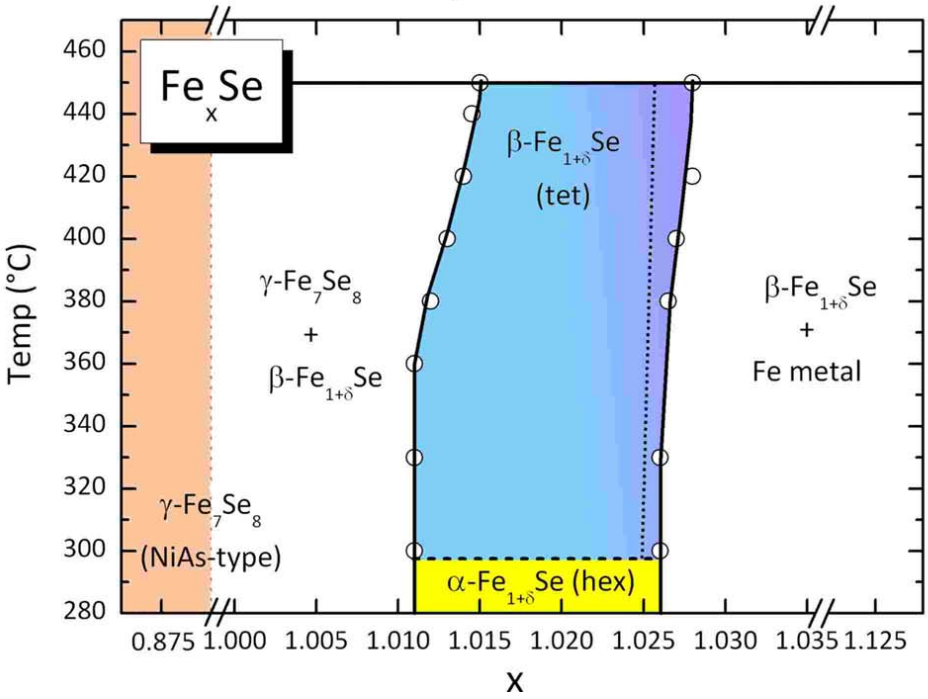

Fig. 2.4 Phase diagram of Fe_xSe close to the stoichiometric 1:1 composition according to McQueen *et al.* [10].

Many experiments confirmed that β-FeSe is not magnetic down to very low temperatures. The δ-polymorph of FeSe which is non-superconducting, is on the other hand a ferrimagnet. The inexistence of magnetic long-range order in β-FeSe has been shown for instance in Mössbauer measurements (Fig. 2.5). The β-FeSe features a phase transition from the tetragonal room temperature structure into an orthorhombic low-temperature form at $\sim 100\,\mathrm{K}$. This structural transition can be disclosed by high-resolution XRD experiments (Fig. 2.6). The transition corresponds to a twisting of the FeSe tetrahedra that split the Fe-Fe distances into two distinct sets. This structural transition shows up indirectly in other techniques such as magnetisation versus temperature curves, resistivity and Mössbauer measurements.

The bulk nature of superconductivity in β-FeSe was confirmed by specific heat measurements that give a normalised specific heat jump at T_c of $\Delta C/\gamma T_c = 1.3(1)$, a value in good agreement with the BCS expected value of 1.4 (Fig. 2.7). The FeSe superconductivity is strongly dependent on pressure (Fig. 2.8). The onset

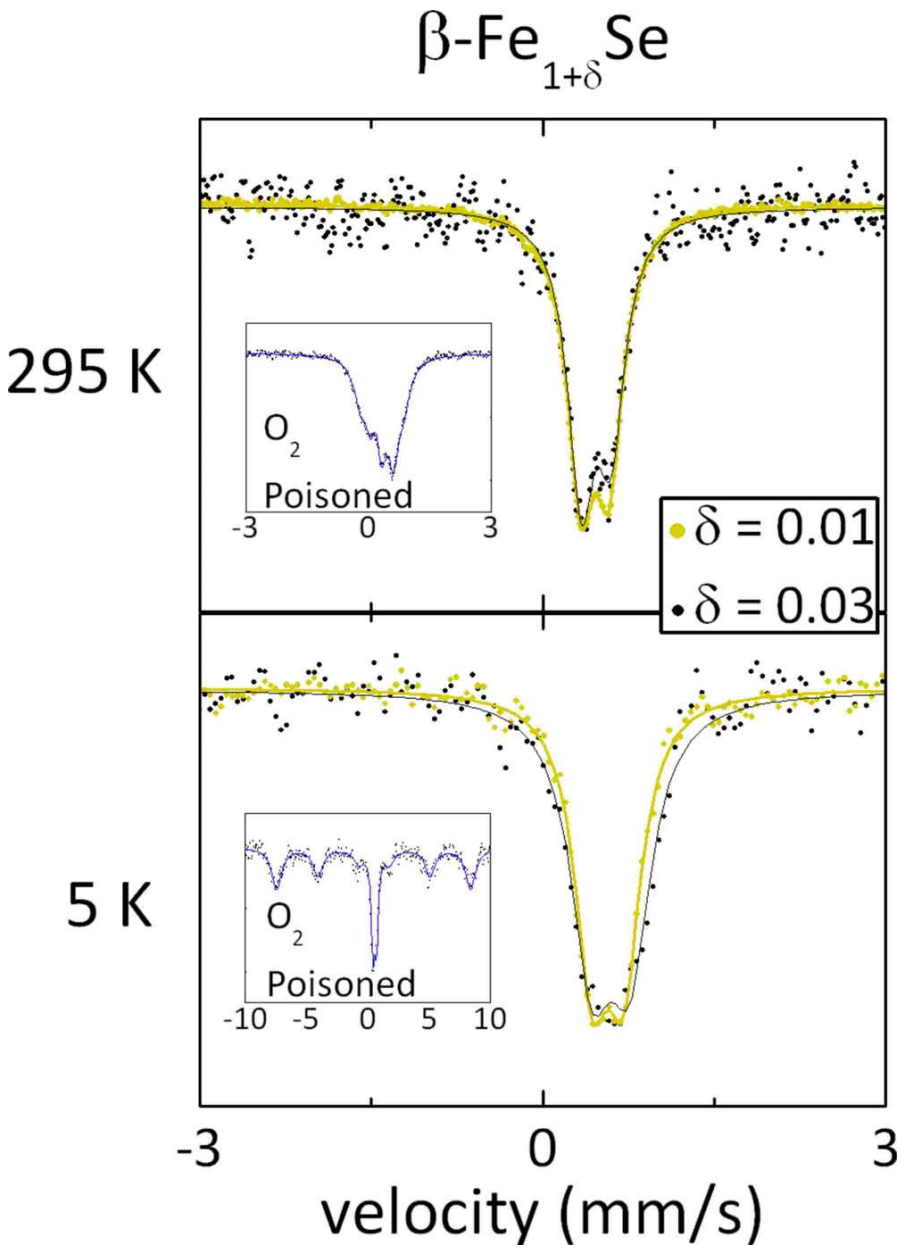

Fig. 2.5 Mössbauer spectra at 295 and 5 K for pure and poisoned samples by oxygen exposure. The pristine samples show no sign of magnetic order [10].

of T_c increases continuously with increasing pressure up to 8.9 GPa, attaining a maximum value of 37 K. Increasing the pressure above this value decreases again the critical temperature. It should be stressed that under pressure, the tetragonal form transforms into the hexagonal form at around the same pressure where a maximum of T_c was observed. There is evidence that β-FeSe although

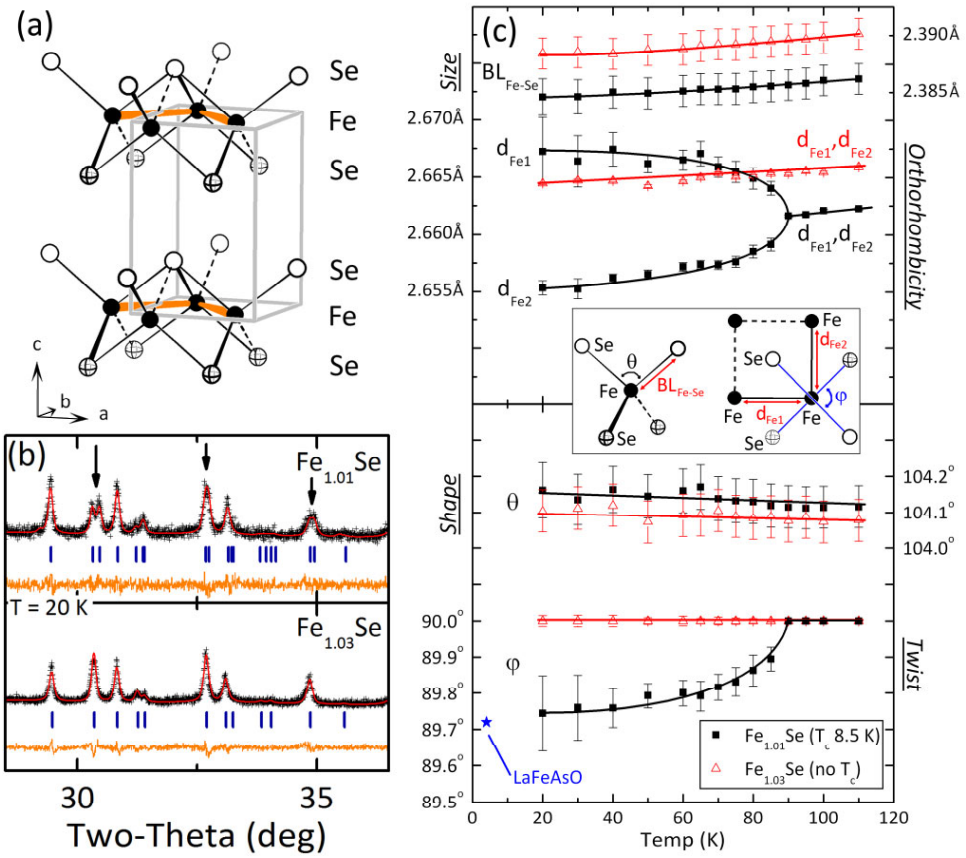

Fig. 2.6 (a) The structure of tetragonal iron selenide consists of two-dimensional layers of edge-sharing Fe-Se tetrahedra. (b) Superconducting $Fe_{1.01}Se$ has an orthorhombic distortion, indicated by the splitting of some peaks in SXRD (arrows), but non-superconducting $Fe_{1.03}Se$ does not. (c) On cooling, $Fe_{1.01}Se$ undergoes a twisting of the tetrahedra, splitting the Fe-Fe distances into two distinct sets. Non-superconducting $Fe_{1.03}Se$, in contrast, shows no transition by SXRD [11].

non-magnetic, is actually on the verge of a spin density wave antiferromagnetic ordering. There is a strong enhancement towards T_c of antiferromagnetic spin fluctuations. This was proved by measurements of the ^{77}Se NMR spin-lattice relaxation rate, T_1^{-1}. These spin fluctuations are enhanced by application of an hydrostatic pressure (Fig. 2.9). It appears that β-FeSe is an "anomalous metal" in the normal phase, classified as a "relatively correlated" electron system. The electronic structure of β-FeSe has been investigated by ARPES and SdH measurements. The mechanism of superconductivity in this compound is still not clear despite many theoretical and experimental efforts. The most favourable pairing mechanism today is either antiferromagnetic spin fluctuations mediating

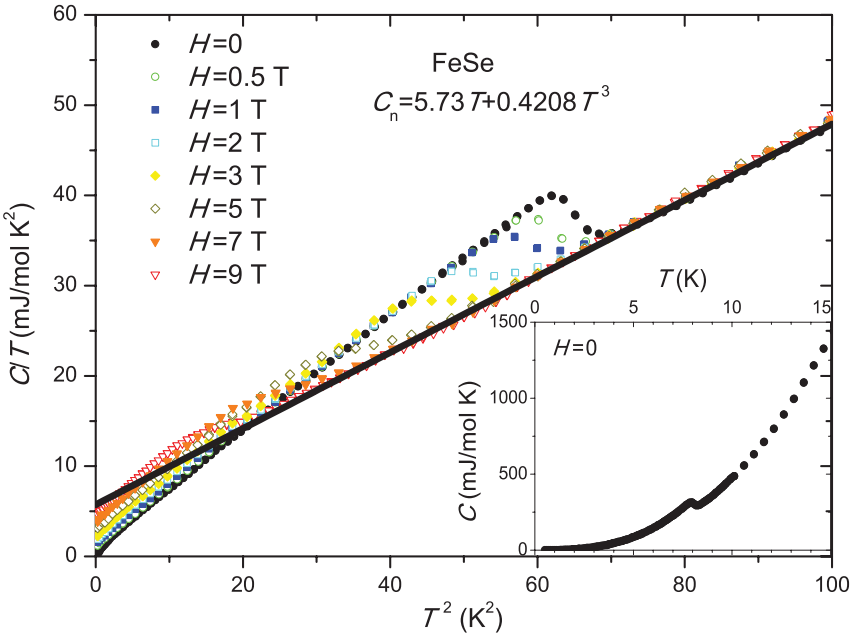

Fig. 2.7 Specific heat as a function of applied magnetic field of β-FeSe [12].

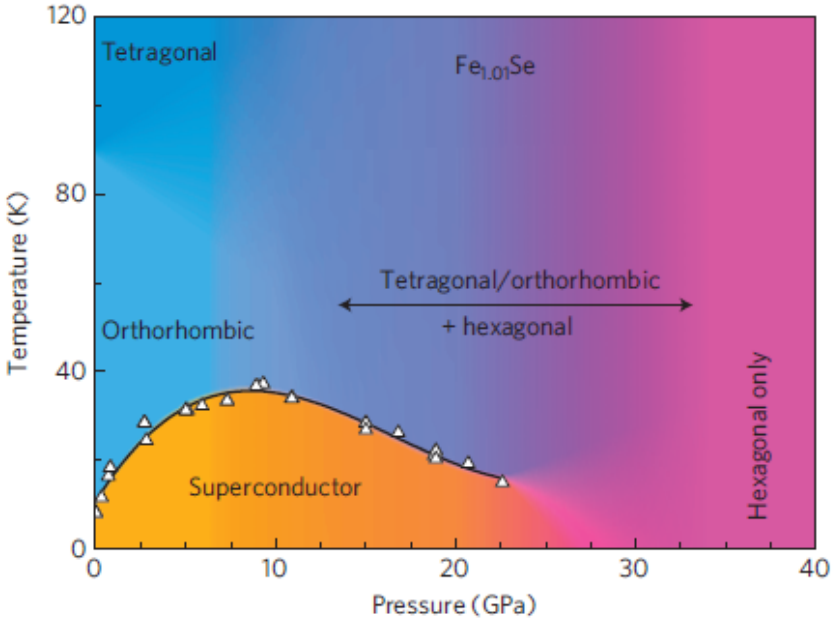

Fig. 2.8 (T-P) phase diagram of β-FeSe [13].

a $s+-$ wave state or Fe 3d orbital fluctuations mediating a $s++$ wave state, as evidence from both spin fluctuations and orbital ordering. The latter is the most favourable model according to the most recent measurements.

The observation of superconductivity above 30 K in FeSe nanoparticles suggested the possible existence of closely related compounds with higher critical

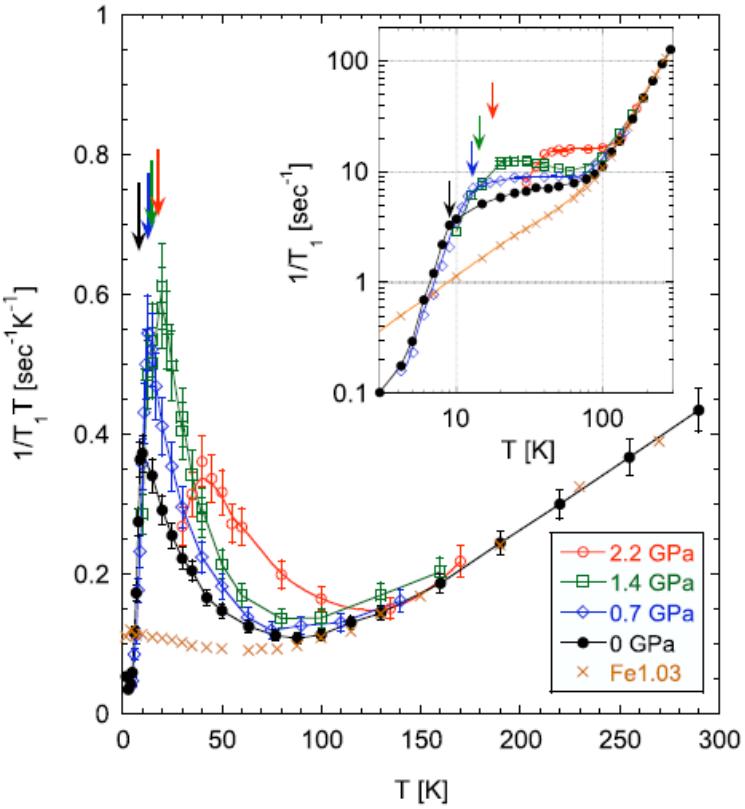

Fig. 2.9 ^{77}Se NMR spin-lattice relaxation rate T_1^{-1} in β-FeSe [14].

temperature [15]. Indeed, there was a discovery of high T_c in FeSe doped with alkaline atoms. This intercalated compounds of general formula $A_xFe_{2-y}Se_2$, with A standing for an alkali/alkali earth metal, exhibit a T_c higher than 30 K. The recent observation of high-temperature superconductivity in a single layer of FeSe deposited on top of $SrTiO_3$ ($T_c = 100$ K) generated great excitement that has driven FeSe superconductivity into an even hotter topic of research [16, 17].

Chapter 3

The Fe-Se phase diagram

Although the Fe-Se phase diagram has been studied quite extensively in the 70's, the best stoichiometry and the optimum synthesis conditions to produce single-phase FeSe samples with the best superconducting properties, are far from being consensual in the literature. This issue arises from the fact that a number of distinct FeSe stable phases with stoichiometry close to 1:1 are known to exist in the Fe-Se phase diagram below the *liquidus* line ($\sim 1075\,^{\circ}\mathrm{C}$) (Fig. 3.1).

The identified FeSe phases close to 1:1 composition are (by order of starting temperature of formation):

- α- Fe_7Se_8, an hexagonal structure ($P3_121$, $a = 7.2613$ Å, $c = 17.675$ Å) in the temperature range $\sim 240 - 380\,^{\circ}\mathrm{C}$.

- β- Fe_7Se_8, a high-temperature orthorhombic polymorph that has a triclinic, low-temperature modification. The α and β phases are also known as 3C- Fe_7Se_8 and 4C- Fe_7Se_8, this notation referring to the number of times the NiAs-type subcell repeats along the c-axis.

- β-FeSe, a tetragonal phase - the one that features superconductivity. It crystallizes in the PbO structure with a Fe-based planar sub-lattice similar to the layered iron-based quaternary oxypnictides, with the $P4/nmm$ space group ($a = 3.779$ Å, $c = 5.511$ Å). This phase has been observed in the temperature range $\sim 300 - 450\,^{\circ}\mathrm{C}$, in the Fe-rich side close to 1:1, the homogeneity range of this phase having been reported to be around 49.0 to 49.4 at.%Se.

- δ-FeSe, a high-temperature ($> 450\,^{\circ}\mathrm{C}$) polymorph of β-FeSe with the NiAs-type hexagonal structure ($P6_3/mmc$ space group, $a = 3.63$ Å, $c = 5.88$ Å).

- γ and γ'- Fe_3Se_4, two slightly Se-rich phases, the former with a monoclinic structure ($I112/m$, $a = 6.20$ Å$, b = 3.53$ Å$, c = 11.31$ Å$, \beta = 92\,°$) and the latter a rarer, higher symmetry polymorph, that has not been fully characterised.

- $FeSe_2$, with the marcasite orthorhombic structure ($Pnnm$ space group, $a = 4.8001$ Å$, b = 5.776$ Å$, c = 3.585$ Å). This phase is obviously far from the 1:1 composition but it is mentioned here as it plays a significant role during the solid state synthesis of FeSe.

It should be stressed again that superconductivity has only been found in β-FeSe phase, but most polycrystalline samples of FeSe that have been reported in the literature feature the presence of other "parasitic" phases (most notably δ-FeSe and Fe_7Se_8) to some extent. Not all such phases have been found (at a small percentage level) detrimental to superconductivity. This will be discussed later on. However, we should stress now that Fe_7Se_8, Fe_3Se_4 and δ-FeSe phases are ferrimagnetic and α-Fe is ferromagnetic. In addition, oxides of Fe and Se can form when the samples are exposed to air, either during or after the synthesis. Therefore, all care during the synthesis procedure to avoid oxidation but also the best stoichiometry and temperature profiles for the solid state synthesis should be carefully addressed. In our work we have been guided by the published Fe-Se phase diagram (Fig.3.1) and many hints reported on previously published work that promise the best synthesis procedure [18–20]. These hints are often contradictory on fundamental questions such as best stoichiometry and one may conclude that the best samples are sometimes produced serendipitously.

An important study that shed light into the mechanisms of formation of FeSe by solid state synthesis was reported by Grivel and collaborators [22]. They have conducted an *in situ* observation of the formation of FeSe by means of a high-energy, synchrotron X-ray diffraction experiment. They followed the formation of different phases in the cooling and heating cycles, starting from a mixture of Fe : Se = 1.0 : 0.9. They have chosen a slight Se deficiency because reportedly it was best for the synthesis of β-FeSe phase. The two elements were ground and packed into a composite Cu/Nb protective metal sheath in order to preserve the powders, since the low melting point (221 °C) and high vapour pressure of Se turns difficult the study on unsealed samples. The set, deformed into a wire (Fig. 3.2a), was cut and a short sample piece was clamped and inserted in a quartz tube and then placed in a high-temperature furnace equipped with kapton windows and a stainless steel heat shield with holes for the beam entrance and exit. The heating was performed at a rate of 2 °C/min

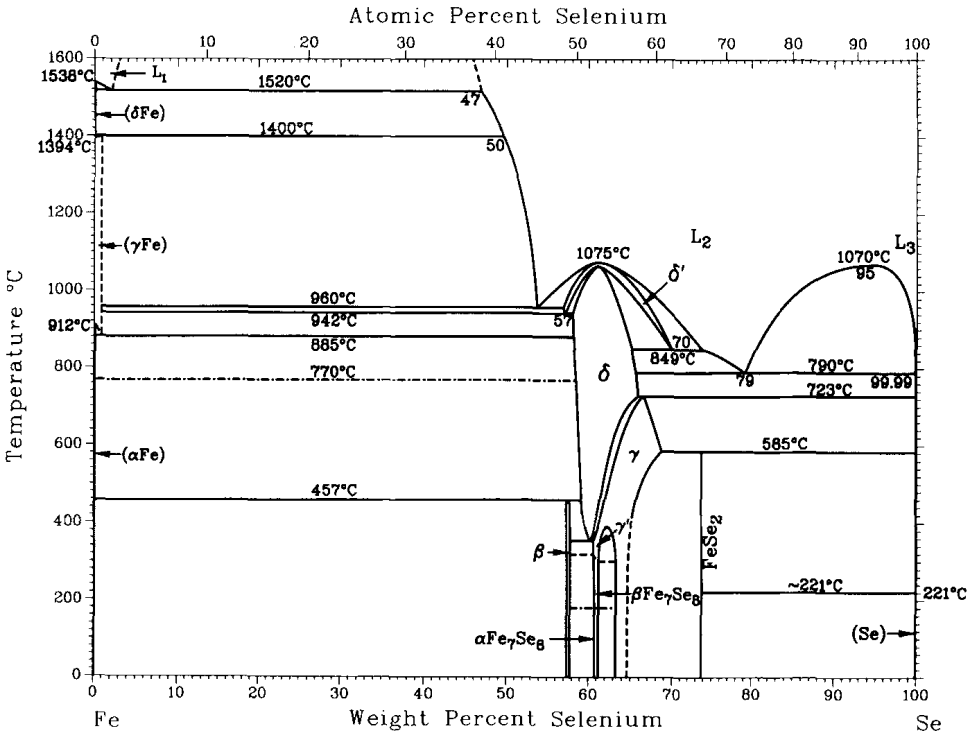

Fig. 3.1 Fe-Se phase diagram [21].

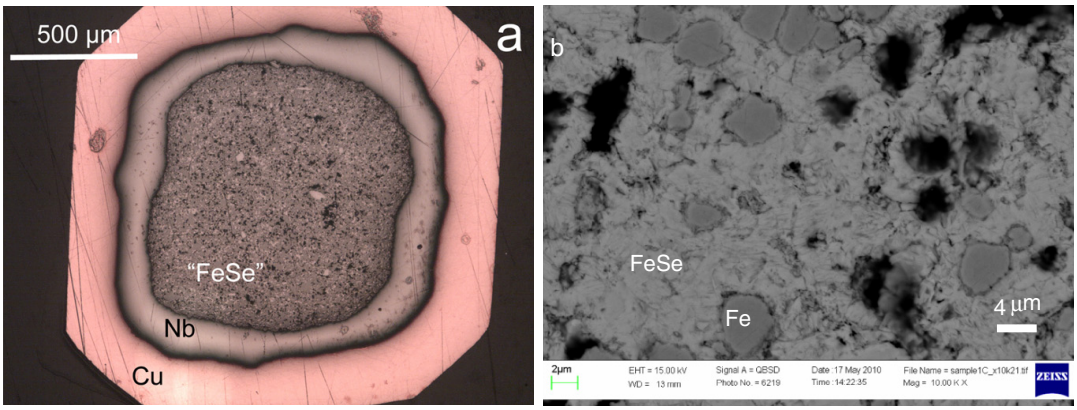

(a) (b)

Fig. 3.2 (a) View of a transverse cross-section of a wire before annealing; (b) SEM picture showing details of the FeSe core after heat treatment on polished transverse cross-sections of samples used for the synchrotron runs - FeSe phase is clearly observed as well as large amounts of Fe [22].

to reach the maximum temperature of 584 °C and the cooling was performed at 5 °C/min. The high-energy X-rays could reach inside the protective Cu/Nb shielding and produced good quality XRD patterns to identify and quantify the phases. The results of such analysis are shown in Figure 3.3.

During the heating process several Fe-Se phases were detected. As can be

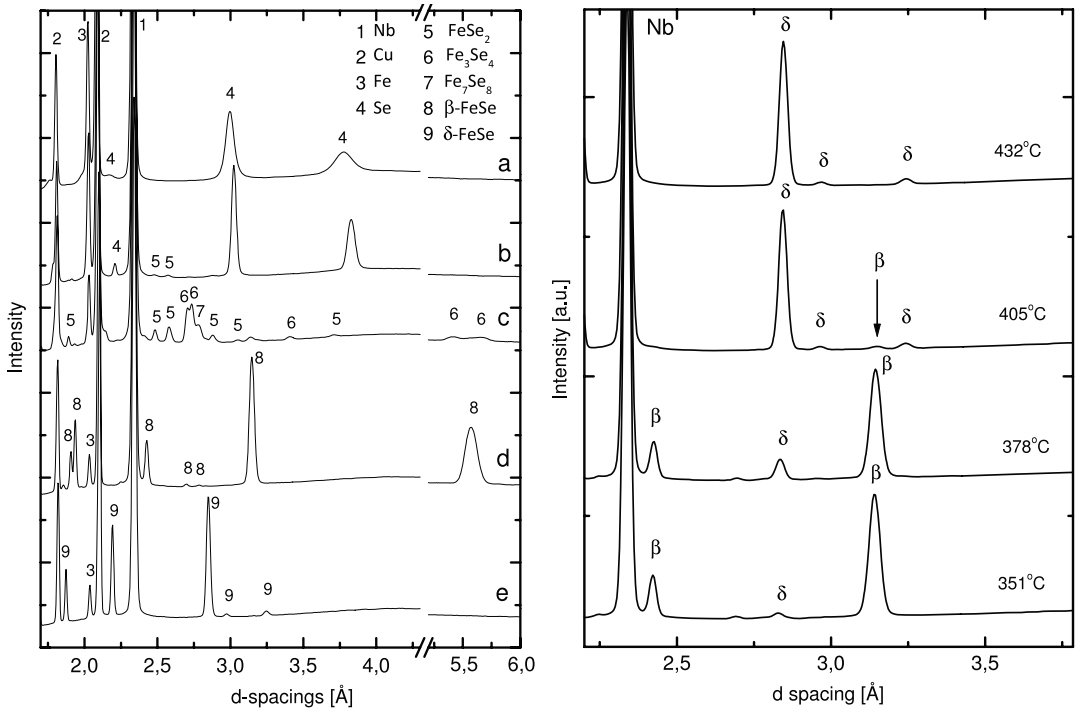

(a) (b)

Fig. 3.3 Diffraction patterns collected (a) during the heating ramp at: a: 25 °C, b: 190 °C, c: 364 °C, d: 394 °C and e: 486 °C ; (b) during the cooling ramp: $\beta = \beta$-FeSe, $\delta = \delta$-FeSe [22].

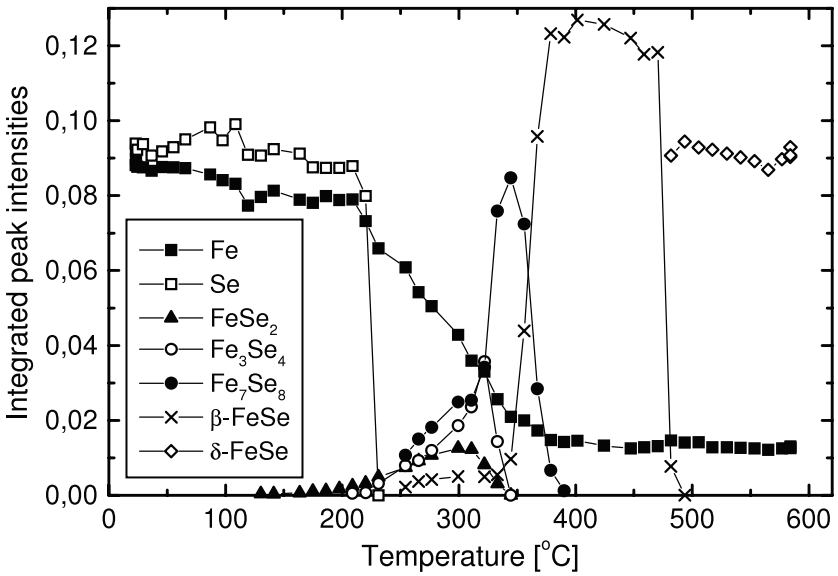

Fig. 3.4 Temperature dependence of the integrated intensity of selected diffraction peaks during heating at 2 °C/min [22].

observed in Figures 3.3a and 3.4, Fe and Se start reacting in the solid state at $\sim$ 125 °C with the formation of a tiny amount of $FeSe_2$, which increases faster after the melting temperature of Se (221 °C) and is accompanied by the formation of Fe_3Se_4. The $FeSe_2$ amount reaches a maximum value at $\sim$ 300 °C whereas Fe_3Se_4 peaks at $\sim$ 320 °C. At $\sim$ 200 °C another phase, Fe_7Se_8, starts growing, first with the same rate as Fe_3Se_4 and then, when Fe_3Se_4 and $FeSe_2$ are consumed, it increases rather fast, reaching a maximum at 340 °C. From that temperature on Fe_7Se_8 itself quickly disappears. Over that same temperature interval ($340 - 380$ °C) the β-FeSe phase forms at a fast rate, leaving a mixture of β-FeSe and unreacted Fe. In Figure 3.4 one can see β-FeSe has a rate of formation almost equal to the rate of diminishing of Fe_7Se_8 and that it reaches a constant value at the same temperature the latter disappears. This strongly suggests that β-FeSe forms essentially through a reaction between Fe_7Se_8 and the still unreacted Fe. A transformation from β-FeSe to the δ-FeSe occurs at $\sim$ 465 °C which in turn transforms back to β-FeSe upon cooling as shown in Figure 3.3b. After cooling, a significant amount of unreacted Fe was found in the sample both by XRD and by SEM/EDS imaging. Because of this, or because of some exposure to air, Grivel reported that no sign for superconductivity down to 1.6 K was found in their (β-FeSe/Fe) sample. Another alternative explanation could be a large deviation from the allowed range of stoichiometry, as this authors have not analysed the exact stoichiometry of the final β-FeSe phase they

obtained. This is one of many studies that shows that not always the synthesis of superconducting FeSe samples succeeds. However, even if their sample turned out to be non-superconducting, from this detailed synchrotron study one can conclude in solid grounds that the formation of the β-FeSe phase involves the successive formation of $FeSe_2$, Fe_3Se_4 and Fe_7Se_8 as intermediate products.

Based on this and on the other published work referred above, we have chosen a maximum heating temperature of 650 °C and different rates of heating and cooling as well as different stoichiometries close to 1:1 were tested in order to obtain the β-FeSe as majority phase.

Chapter 4

Experimental Methods

4.1 Synthesis

Many well known methods can be used to produce FeSe compounds such as the solid-state synthesis (e.g. mechanosynthesis), sol-gel, Bridgman, high-pressure, and other methods [23], depending if one aims at obtaining a single crystal, polycrystalline or even nanocrystalline sample. Since the laboratory is not equipped with all the equipment required for some of these methods, in particular the growth of single crystals, the *solid-state method* for polycrystalline material synthesis was the chosen one in this work.

The solid-state method is commonly used in the preparation of polycrystalline solids from a mixture of solid starting materials and involves high and extended heating of the molar proportions of the solid reactants in powder form. Since impurities are impossible to remove at the end of the reaction, the powders should be as pure as possible. The reaction occurs in the solid state (no melting involved), requiring the diffusion of ions across the grain boundaries. Grinding should be done to improve homogeneity and to reduce particle size and the powder mixture can be palletised in order to improve grain contact and lessen voids. In addition, if these materials are air sensitive during the reaction, as in our case, so unlike the cuprates, the synthesis is not so easy since the materials need to be sealed in vacuum or inert atmospheres.

In this work all samples were prepared by solid-state reaction method in quartz tubes (chemically inert to the reactants), sealed under vacuum, using high purity powders of iron (99.998 % Alfa Aesar) and selenium (99.999 % Alfa Aesar) ground with an appropriate stoichiometry according to the equation:

$$\mathrm{Fe} + (1 - x)\,\mathrm{Se} \rightarrow \mathrm{FeSe}_{1-x} \tag{4.1}$$

Different cycles involving different temperatures as well as heating and cooling ramps were performed using a TERMOLAB furnace (Fig. 4.1). The furnace, through Kanthal A-1 wire resistances, attains temperatures up to a maximum of 1150 °C; different cycles of heating/cooling can be performed with different ramps of temperature programmed in an Eurotherm temperature controller. Weighing of the powders for synthesis and further characterisation was carried out on a RADWAG analytical balance, with a precision of 0.03 mg.

Fig. 4.1 TERMOLAB furnace.

4.2 Structural characterization methods

Powder X-ray Diffraction (XRD)

4.2.1 Introduction

Since its discovery in 1895 by W. C. Roentgen, X-rays have been playing an important role in many areas, and one of them certainly is materials science. The fact the interatomic distances in a crystalline material have the same order of magnitude as X-rays wavelength makes it possible for crystals to diffract an X-ray beam. From an analysis of the diffraction pattern, structural information

can be obtained about the sample; therefore, X-rays are an ideal radiation for this type of studies.

Many materials either natural or synthesised are obtained, not as a single crystal, but as a polycrystalline material and often not even as a single phase but as a mixture of phases. Thus, there is a need to characterise the sample beyond its elemental composition, identify the phases and, if possible, quantify them. Indeed, the purity of the sample often impacts on its properties as well as its suitability for an intended use. Powder X-ray diffraction (XRD) offers a convenient method to characterise these materials. What makes this technique so powerful is that different structural features of a material (unit cell metrics, unit cell contents, crystalline grain size, microstrains, etc.) have different effects on the powder diffraction pattern.

After the first powder diffraction camera, conceived by Debye and Scherrer (1916), a huge progress on the creation of new equipment occurred and it was even more noticeable with the great advances in electronics, computers and software. One of the systems that came out was the Bragg-Brentano parafocusing system (Lindemann and Trost, 1940; Friedman, 1945) and this system will be mentioned in detail later. In this work, the powder XRD was used for qualitative and quantitative analysis of the different phases present at room temperature in our samples that were synthesised under different conditions and with different stoichiometries.

4.2.2 Elementary theory of XRD

Protons and electrons are charged particles which interact with electromagnetic waves such as X-rays. Since the electrons are much lighter particles, its contribution for scattering of X-rays will be much stronger than that of the protons (nuclei). The amplitude of the scattered X-rays is given in scattering theory by the Fourier transform of the electron density. In this way, the distribution of electron density is probed in a XRD experiment and since the crystal structure is periodic, one can therefore determine the contents of a unit cell from the XRD diffraction pattern.

The diffraction from a crystalline sample can be explained and visualised by using the simplified version, described by Bragg father and son, of the theory developed by von Laue, in which an incident X-ray beam would be reflected by sets of parallel planes (h, k, l) of atoms, equally spaced by a distance d. The

condition for diffraction from such set of planes is

$$2d \sin\theta = n\lambda \tag{4.2}$$

which states that in order to get a constructive interference condition, the path length difference between two incident waves in consecutive planes must be a multiple number of the wavelength, λ, as can be seen in Figure 4.2; the angle θ is the angle of incidence of the beam to the planes and n is the order of reflection such that for $n = 1, 2, ...$, we get reflections of first, second order, etc., relative to the same set of planes (h, k, l). As the diffracted beam exits the sample with the same angle θ to the reflecting planes, 2θ is the diffracted angle, the angle between the diffracted and incident beams.

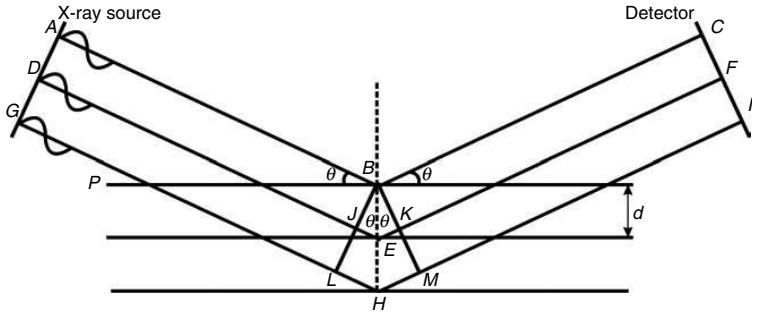

Fig. 4.2 Illustration of Bragg reflection from a set of parallel planes [24].

The scattered amplitude from one unit cell is the structure factor F_{hkl}, defined as

$$F_{hkl} = \sum_j f_j e^{[2i\pi(hx_j + ky_j + lz_j)]} e^{-W_j} \tag{4.3}$$

where f_j is the atomic scattering factor for atom j in the unit cell with fractional coordinates x_j, y_j, z_j and W_j is the thermal displacement parameter (Debye-Waller factor), a smearing factor due to the atomic motion. The intensity of the diffracted beam, I_{hkl}, is proportional to the square of the magnitude of the structure factor:

$$I_{hkl} \propto |F_{hkl}|^2 \tag{4.4}$$

The experiment consists in measuring the scattered intensity as a function of the scattering angle. The above is valid for elastic scattering of X-rays that is responsible for Bragg reflections. In addition to this, other inelastic processes also occur but they are incoherent and do not contribute to diffraction. In the treatment of experimental data, corrections need however to be applied for

processes such as absorption of the incoming and outgoing beams, extinction, etc.

One can say that there are two crystallographic parameters that essentially define the structure of every powder diffraction pattern: the unit cell and its contents. Thus, the pattern can be constructed as follows:

- Positions of the Bragg peaks are established from Bragg's law as a function of λ and d-spacing, the latter being calculated from the unit cell dimensions.
- The intensities are calculated for individual Bragg peaks from the structural model, which includes the coordinates of atoms in the unit cell and their thermal displacement parameters.
- The shape of the Bragg peaks is represented by the so-called peak shape function (a convolution of the instrumental broadening, wavelength dispersion and intrinsic specimen broadening due to crystalline size and strain).
- The result pattern is a sum of the individual peaks and a background function.

For polycrystalline materials with complex unit cells or with different mixed phases, one of the major problems is the overlap of the many Bragg peaks. Therefore, a fit of a model to the whole pattern is often more appropriate than extracting the scattering amplitudes from the data from a deconvolution of superimposed peaks. Having a reasonable model as a starting point, this model can be refined against experimental pattern, the $I(\theta)$ function. The refinement can be performed by least-squares or other minimisation technique. The quantity minimised is usually a weighted sum of the squares of the residuals between the calculated and observed patterns. Such an approach called *full profile fitting* is also known as the *Rietveld method*.

4.2.3 XRD equipment

The equipment used in this work was a Bruker AXS D8 ADVANCE diffractometer, with a DAVINCI (automatic change of optics between parallel and divergent beams) design (Fig. 4.3).

Some of its components are:

- a ceramic sealed tube with a Copper ampoule ($K_{\bar{\alpha}} = 1.5418\,\text{Å}$) which generates the X-rays; the anode must be continuously cooled with chilled water to avoid meltdown.

Fig. 4.3 Bruker AXS D8 ADVANCE diffractometer.

- for Bragg-Brentano geometry: a variable divergence slit (0.1 to 1°), computer-controlled by a stepper motor and two sets of Soller slits that limit the divergence of the incident beam, one in the direction perpendicular to direction along the axis of the goniometer - the axial divergence - and another to reduce the divergence of the diffracted beam before it reaches the detector.

- for parallel beam geometry: a Göbel mirror with 40 mm graded multi-layer optics tuned for Cu radiation, creating a highly parallel beam while suppressing white radiation and K_β radiation.

- a Ni filter is used in Bragg-Brentano mode in order to filter the Cu K_β radiation. To do so, a Ni foil is ideal as it has an absorption edge below the wavelength of the K_α line and just above the wavelength of the K_β line [25]. The filter used has a 0.02 mm thickness and reduces the K_β intensity to less than 0.5% of the K_α intensity.

- a compact XYZ table, which provides adjustment in the position of the sample related to the incident beam.

- a vertical goniometer (with an horizontal rotation axis, and a diameter of 560 mm), with powerful stepping motors, optical positioning encoding and precise counterbalancing, can move both arms where the source and the detector are placed; it can work in the $\theta - \theta$ (default) or $\theta - 2\theta$ modes.

- a silicon drift LYNXEYE detector, which is a one-dimensional (compound silicon strip) detector with 192 strips covering an angular range of $\sim 3°$. It has a global maximum count rate of 10^8 cps and an energy resolution of $\sim 25\%$ at the Cu K_α energy, useful to discriminate against fluorescence. The detector can also work in the 0-D (point detector) mode by integrating the counts of all the strips.

This equipment has the possibility to operate in more than one geometry: parallel beam and the Bragg-Brentano parafocusing geometry (Fig. 4.4), the last one used for this work. In this geometry, the diffractometer operates in the scanning mode with incident and diffracted beams forming the same angle θ with the surface of a flat sample. The divergence of the latter, as referred above, is limited by a Soller slit before interacting with the sample, and after that it converges (self-focus) at a receiving slit and then goes through another Soller slit before reaching the detector.

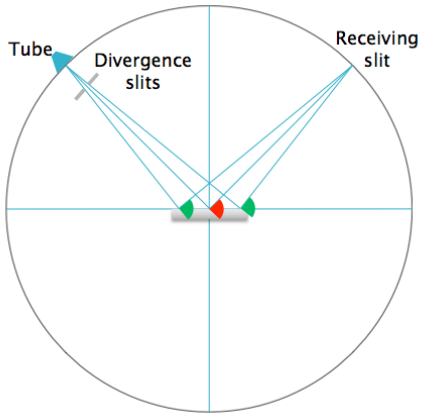

Fig. 4.4 Bragg-Brentano geometry.

It should be pointed out that this diffractometer has an excellent angular resolution, the instrumental line broadening being less than 0.05° of FWHM for 2θ angles less than 60°, as shown in Figure 4.5. Therefore, size broadening effects are detectable for grain sizes less than 250 nm.

For phases analysis, a first attempt to identify them was conducted using the ICDD-JCPDS database installed in the DIFFRAC.SUITE EVA software. After successful phase identification, a quantitative analysis was performed using

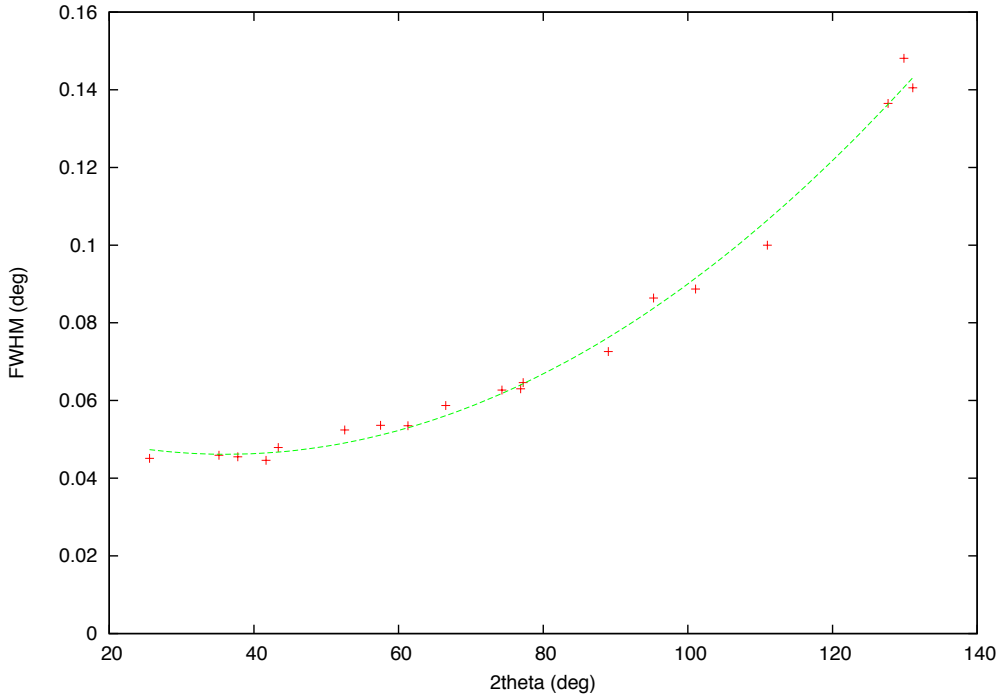

Fig. 4.5 Resolution function of the D8 diffractometer measured with a corundum sample.

the DIFFRAC.SUITE TOPAS Rietveld Analysis Software; for the most difficult cases only a qualitative analysis was performed by profile matching using the Pawley method.

4.3 Scanning Electron Microscopy (SEM)

4.3.1 Introduction

The scanning electron microscopy, since its invention in 1937 by Von Ardenne, has achieved a great impact in different fields such as physics, nanotechnology, medicine, biology, etc. Its popularity comes from the observation and characterization of organic and inorganic materials that can be provided in the micro to nanometer range going far beyond optical instruments. A wise choice of parameters like the beam energy, intensity, width and preparation of the sample in study is of extreme importance since these (and other) parameters play a role in the information one can obtain, in the form of images, about the sample. In the case of superconductor materials, SEM can be a useful tool to probe its microstructure and the properties related to it. Coupled to the SEM, Energy Dispersive X-Ray

Spectrometry provides important information about the chemical composition of this type of compounds.

4.3.2 Fundamental principles

In electron microscopes, electrons have very short wavelengths which change according to the applied voltage. Based on de Broglie's theory of the wave-particle duality, the wavelength λ of an electron can be related to its momentum $p = mv$ by:

$$\lambda = \frac{h}{p} = \frac{h}{mv} \tag{4.5}$$

where $h = 6.626 \times 10^{-34}$ Js is the Planck constant and m and v are the mass and velocity of the electron, respectively. Applying an accelerating voltage, V, the electron acquires a kinetic energy which must equal the potential energy. Thus,

$$eV = \frac{mv^2}{2} \tag{4.6}$$

Using this result one can rewrite the expression for momentum:

$$p = (2meV)^{1/2} \tag{4.7}$$

Substituing this result on equation (4.5) one gets the relationship between the electron wavelength and the accelerating voltage:

$$\lambda = \frac{h}{p} = \frac{h}{(2meV)^{1/2}} \tag{4.8}$$

For electron microscopy, since an electron can reach high velocities (nearly the velocity of light), relativistic effects have to be considered, so this latter equation should be modified:

$$\lambda = \frac{h}{[(2m_0eV)(1 + \frac{eV}{2m_0c^2})]^{1/2}} \tag{4.9}$$

As an example, for an accelerating voltage of 10 kV one should get a wavelength of 0.0122 nm. With such small wavelengths it is therefore possible to see atomic structures. However, SEM resolution hardly attains 5 nm, which precludes visualisation of individual atoms. TEM (transmission electron microscopy) has an intrinsic higher resolution and individual atoms can be resolved.

4.3.3 Interaction of accelerated electrons with a sample

When the interaction between the electron beam and the sample takes place, it is not only confined to the surface layers but also occurs in atoms in the bulk of the sample. That leads to useful information about the sample such as surface features and its size and shape, composition and crystalline structure. The interaction with the sample can arise in different ways. Since electrons can undergo change in momentum and/or in energy in those interactions, for simplicity we can classify them into two major ones, the elastic and inelastic interactions:

- **Elastic interactions**

  This process involves no loss of energy, i.e., no energy is transferred from the incident electron to the sample. As a result, the electron which leaves the sample still has its original energy and will contribute to the direct beam. This happens only if the electron does not suffer any interaction at all. Furthermore, it is required that the electron is deflected from its path as a result of a coulombic interaction, F, with the positive potential of the nucleus:

  $$F = \frac{Q_1 Q_2}{4\pi\epsilon_0 r^2} \tag{4.10}$$

  As can be seen by the equation, for smaller r, i.e., the closer the electron passes by the nucleus, the larger is F and consequently the scattering angle, being, in general, a strong interaction. Because of its dependence on the charge, the force F with which an atom attracts an electron is stronger for atoms containing more protons. Therefore, one can conclude the Coulomb force increases with increasing atomic number Z of the respective element.

  The electron, when it passes through the sample, may be scattered not only once but several times. That possibility will depend on the probability of a scattering event, determined by the interaction cross-section, and on the mean free path, i.e., the average distance an electron travels between two collisions. A consequence of all that has been told so far is the observation of contrast between different materials. Since the Coulomb force increases with increasing atomic number Z, the areas where heavy atoms are localised will appear with darker contrast than the others comprising light atoms. One application of high angle scattering is the use of the backscattered electrons by SEM:

  - Backscattered electrons (BSE)

When high-energy incident electrons hit, typically, a sample atom's nucleus, they will be reflected or back-scattered by elastic scattering. Since electrons are emitted from the depth of the sample, the resolution of the image will not be as good as the one obtained by secondary electrons (SE). However, a contrast in image can be determined by the atomic numbers of the elements in the sample as well as the distribution of the different chemical elements (Fig.4.6). The electron beam can actually penetrate to a significant fraction of the range before it reverses its course and returns to surface to escape as a backscattered electron. Such electrons can carry other information, like structure's information, due to the influence of its subsurface features (e.g.: inclusions of different composition, voids, etc.).

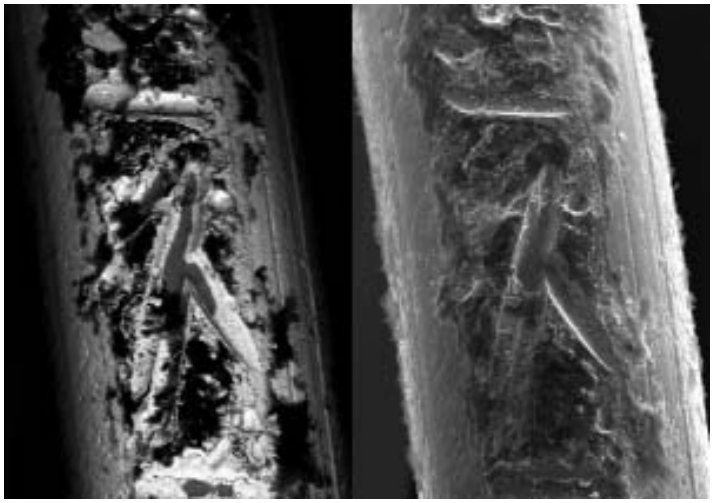

Fig. 4.6 SEM images of corroded metal acquired using backscattered electrons (left) and secondary electrons (right) [26].

- **Inelastic interactions**

  In inelastic interactions, there is a transfer of energy from the incident electron to the sample which means the electron after interaction will have a reduction on its energy. The energy transferred to the sample during the interaction can produce different signals such as secondary electrons (SE), phonons, X-rays, Auger electrons, etc.
  From the many ways an electron can lose some of its energy in the sample, those useful for imaging are the ones that result in radiative or non radiative processes. This happens when the energy is transferred to one of the inner shell electrons, leading to ionisation or electronic rearrangement.

When the sample is bombarded by the beam and electrons are ejected from atoms that make up the sample's surface, the latter are left in an excited state due to the resulting electron vacancies. In order to return to the ground state, those vacancies are filled by electrons from a higher shell. The energy difference between the two shells can be released from the atom in one of two ways:

– In the Auger process, the energy difference can be transmitted to another outer shell electron, ejecting it from the atom with a specific kinetic energy. That energy corresponds to the difference between the excitation energy and that of the electron shell from which the Auger electron originates. It is an energy similar to the one of corresponding X-rays and thus rather low. The absorption of these electrons in the material occurs more easily than that of X-rays, a reason why only Auger electrons created close to the surface are capable to leave the specimen.

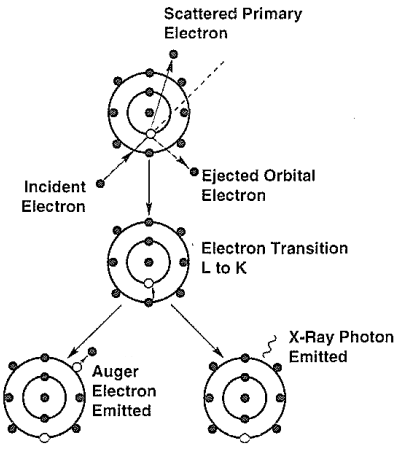

Fig. 4.7 Inner shell ionisation and subsequent de-excitation by electron transitions. The difference in energy from an electron transition is expressed by the emission of an Auger electron or by the emission of a characteristic X-ray photon [27].

– In the X-ray process, the energy difference turns into the emission of a photon of electromagnetic radiation with a sharply defined energy, characteristic of each element present in the sample (each element has a characteristic number of electrons localised in well-defined energy states). With increasing Z, the number of electrons increases as well as the energy levels. Thus, more transitions are possible. Let us consider an element in the third row of the periodic table (with electrons in the K, L and M shells) as an example: if an electron is

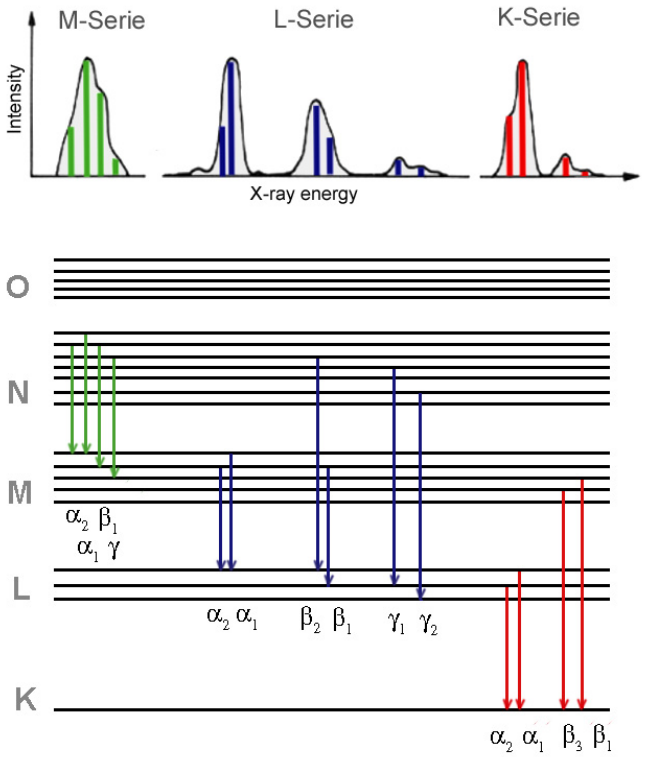

Fig. 4.8 Possible electron transitions generating X-ray emission [29].

ejected from the K shell, it may be replaced by an electron from the L shell or M shell generating K_α or K_β radiation, respectively. Different transitions might come from the same shell because diverse energy levels are possible, i.e., the energy levels depend on hybridisation and coordination of the atom. The transitions are then numbered with increasing energy difference. Transitions into the K shell might occur from the levels L_2 and L_3 but not from the L_1 (corresponding to the level 2s) since this is a quantum mechanically forbidden transition [28]. A forbidden transition also happens from the M_1 level to the K shell (Fig. 4.8). In conclusion: this kind of processes allows to obtain the elemental composition of the sample, using the so-called Energy Dispersive X-Ray Spectrometry (EDS or EDX) technique.

Besides these two latter processes, another two should be referred:

– Continuum X-Ray Production (Bremsstrahlung)

  An incident electron undergoes deceleration in the Coulomb field of the sample's atom, giving origin to x-rays due to the loss in energy. Owing to the fact that the interactions are random, the electron may

lose any amount of energy in a single event. Therefore, the intensity of this braking radiation, often designated as "Bremsstrahlung", can take on any value from zero up to the incident energy of the electron of the primary beam. This is the main constituent of the continuous background in a X-ray spectrum.

– Secondary electrons (SE)

Secondary electrons (SE) are low-energy electrons, some ejected from the K-shell of the sample's atoms where substantial energy loss occurs, and others loosely bounded to the outer shell that are ejected from the atom as a result of an inelastic scattering interaction with the electron beam. With an energy typically of 50 eV or less, only those within a few nanometers from the sample surface will escape from it and can be detected and used for the sample's surface topography. Secondary electrons usually provide better image resolution than backscattered electrons.

4.3.4 Description of the microscope used

The scanning electron microscope (SEM) displays the examined object by sweeping a thin electron probe (beam) over the sample inside the microscope chamber. The imaging quality depends on the electron probe parameters: *spot size*, *aperture angle* and *beam intensity*.

The **spot size** determines the resolution of the microscope as well as usable magnification, being smaller at shorter working distances[1]. The **aperture angle** is the vertex angle of the cone-shaped incident beam. The wider the cone, the lower the depth of focus. **The beam intensity** is the number of electrons that passes through the probe in a specific time. There is a relation between the image noise of the microscope and the number of electrons used for the information that arises from each picture element, so a larger time for image scanning is necessary at low beam intensity and vice versa. A combination of these three parameters allows the optical system to operate in different modes such as the two examples below:

- *Work on high magnification* - provides a high resolution, therefore low beam intensity, short working distance and a slow scanning speed are necessary.

[1] working distance: the distance between the lower objective pole piece and the focused sample's surface

- *Work with high depth of focus* - the aperture angle is lower but the spot size is bigger in comparison with the resolution mode, providing a greater depth of focus but also a good resolution.

The SEM can be said as being composed by two main parts, the electron column, where the electron probe is formed, and the detection system. These are the common parts to any kind of SEM; other components may vary from SEM to SEM. As an example, many SEMs still use tungsten or LaB_6 thermionic emitters while others, more expensive microscopes, may have cold, thermal, or Schottky field emission sources in order to enhance performance and lifetime. The type of vacuum may also vary as well as the type of detector. In the following will be described the experimental system used in this work, the TESCAN VEGA3 SBH SEM.

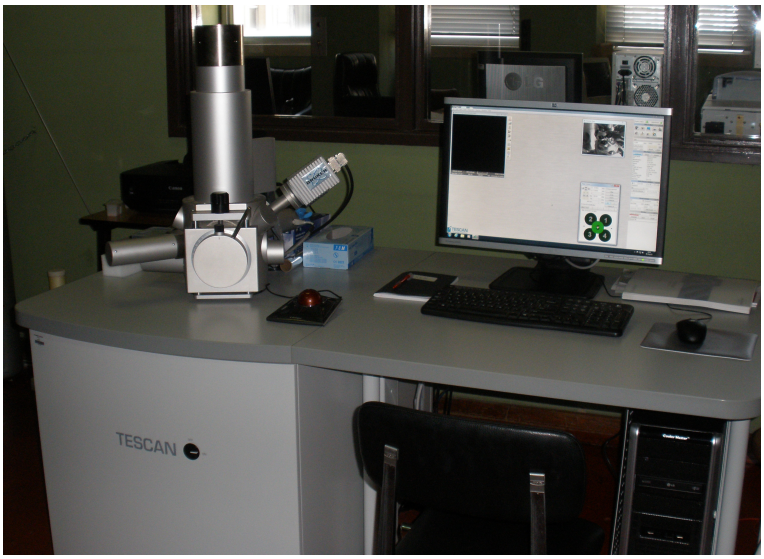

Fig. 4.9 Picture of the TESCAN VEGA3 SBH SEM equipment used in this work.

The ***column*** of the microscope (Fig. 4.10) consists of the following parts[2]:

- **The electron gun** has three components: a tungsten wire filament, acting as the cathode, the grid cap or Wehnelt cylinder, and the anode. The filament and Wehnelt cylinder are connected to the negative electric potential; the anode and the remaining part of the column are on the earth potential. In order to cause emission of free electrons, the filament needs to be heated to a temperature of $2000 - 2700\,\mathrm{K}$. Those electrons after emission are spread out into a broad cone; the Wehnelt cylinder, is maintained at a

[2]The following description of the column parts was based on the manual *Scanning Electron Microscope VEGA 3 SEM.*

voltage slightly more negative than the filament, providing a controlled and focused beam inside the gun. The voltage between the Wehnelt cylinder and the anode determines the accelerating voltage of electrons and thus their energy. A hole in the anode allows a fraction of these electrons to proceed down the column. With this system it is possible to obtain an electron beam with the following specifications: a dimension of $25 - 50\,\mu$m, an energy from 200 eV up to 30 keV, an emission current up to $300\,\mu$A and a brightness of 10^6 A/cm^{2}sr.

- **The gun centering**, formed by a system of electromagnetic deflection coils under the gun, ensures that the electron beam, which is tilted, enters the axis of the optical system of the column.
- **The spray aperture** placed under the deflection coils referred above, helps to collimate the electron beam emitted by the gun.
- **The condensers C1 and C2**, strong magnetic lenses, are used to demagnify the spot size the electron beam produces and place a much smaller one in the sample (the higher the excitation of the condenser, the shorter its focal length and the higher its demagnification).
- **The final aperture** cuts the size of the final incident beam, before it reaches the last parts of the column. As a consequence, the use of an **intermediate lens (IML)** is necessary for the aperture change of the beam.
- **The stigmator**, an electromagnetic octupole, compensates for any astigmatism that might arise in all displaying modes.
- **The scanning coils**, formed by two stages of deflection coils, are used first, to deflect the beam off the optical axis of the column and second, to bend it back onto the axis at the pivot point of the scan (Fig. 4.11). The coils are connected by a scanning ramp; the ramp frequency provides the scanning speed of the electron beam and the amplitude gives the microscope's field of view and the magnification.
- **The objective** is the last magnetic lens that forms the resulting electron beam and is in general determined by the working distance.

The ***detection system*** contains three different detectors, the SE, BSE and EDS detectors:

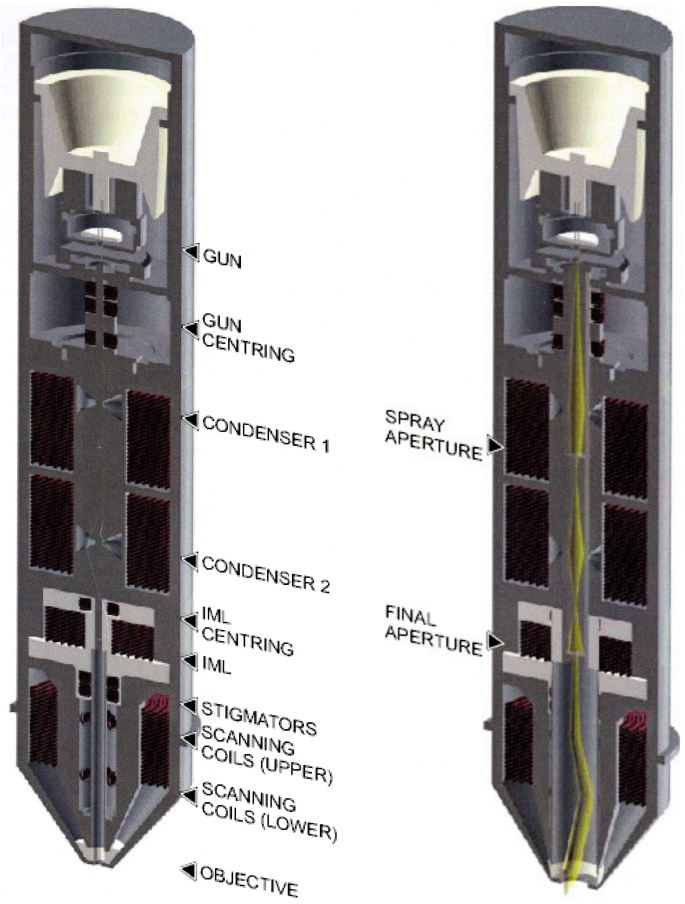

Fig. 4.10 VEGA3 SEM cross section and schematic representation of the optical elements [30].

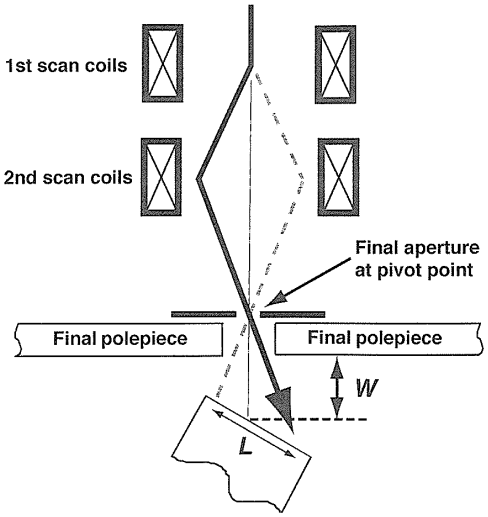

Fig. 4.11 Scheme of the deflection system inside the final lens. Working distance is represented here by W [27].

- **The secondary electron (SE) detector** is of Everhart-Thornley type. It consists of a scintillator inside a Faraday cage which is inside the microscope's chamber. In order to attract the low-energy secondary electrons that come from the sample surface, a low positive voltage is applied to the Faraday cage; the scintillator, with a high positive voltage, accelerates and converts the incoming electrons into photons. After this, the resulting photons are transferred through a light guide to the photomultiplier outside the chamber.
- **The backscattered electrons (BSE) detector** is of the scintillator type; it has an annular (YAG) mono-crystal scintillator with a conductive surface placed in the optical axis under the lower objective pole extension. Without any extra acceleration, the backscattered electrons touch the scintillator and excite its atoms, leading to a successive production of photons which are then sent to the photomultiplier and processed in the same way as the signal coming from the secondary electrons [30].
- The **EDS detector** is a silicon drift detector (SDD). Many EDS systems equipping electron microscopes are based on silicon crystals doped with lithium. However this type of detector have some disadvantages: the impurity compensation is far from ideal and the detector in order to work properly has to be cooled below liquid nitrogen temperature. In the case of our equipment, the VEGA3 SBH SEM, which is equipped with a modern Bruker XFlash® 410 M detector, the latter does not need to be cooled with LN_2; it is only moderately cooled by vibration free thermoelectric coolers. Any heat generated is dissipated by unforced convection with no need for external cooling means. It has 10 mm^2 active area and a resolution of 133 eV at Mn K_α energy, a counting rate of 100000 cps and can detect all elements from B to Am [29]. This system has a very thin radiation entrance window which separates the sensitive detector area from the ambient atmosphere and guarantees a good transmission of the X-rays of interest. Software is available for elemental analysis, quantification by the PB-ZAF method, and to perform quantitative profile and mapping.

One should refer that this kind of microscope operates in a clean environment, so a high vacuum and an extreme care with the sample mounting should be taken: besides all the procedure related to cleanness, the samples have to be conductive or, if not, they have to be made conductive by a surface coating of Au or other conducting material.

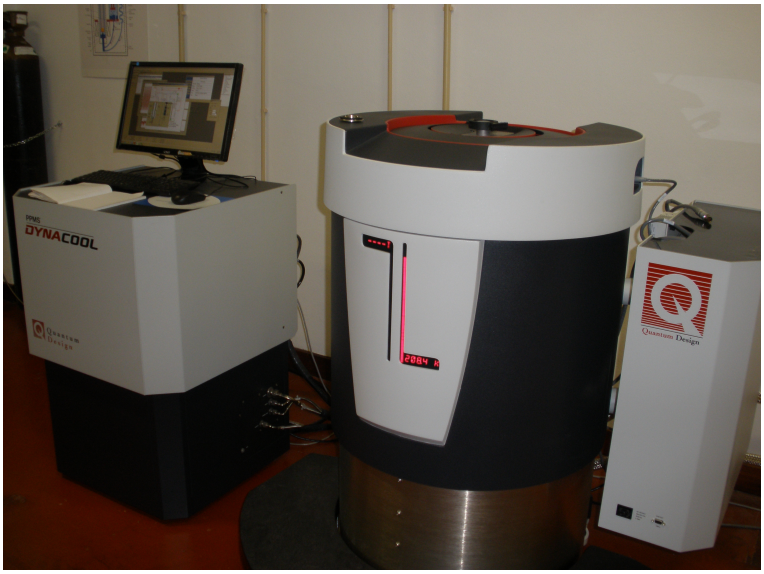

Fig. 4.12 PPMS DynaCool magnetometer.

4.4 Electrical and magnetic characterisation methods

4.4.1 Physical Properties Measurement System (PPMS)

Superconductor materials are well-known for their property of offering no resistance to current flow. However, the superconductivity can only be proved by the verification of $R = 0$ and, more important, by the existence of the Meissner effect. In some cases, when the critical temperature, T_c, of the material is higher than the boiling point of liquid nitrogen (77 K), the Meissner effect can be observed at sight by the levitation of a magnet in a cooled superconductor material, but in the majority of cases this is not possible since the materials have lower T_c. An equipment capable of providing us that knowledge by measuring the temperature dependence of the magnetic response is the magnetometer.

In this work we used a Physical Property Measurement System (PPMS), the 9T PPMS DynaCool, from Quantum Design (Fig. 4.12). This equipment enables us to measure properties such as the magnetic moment, resistivity, specific heat, etc., from 1.8 K up to 400 K in applied magnetic fields up to 9 T, with no need to be supplied with any liquid cryogens as it operates using a closed-cycle He cryostat. A two-stage pulse tube cryocooler is used for both the superconducting magnet and the temperature control system, providing lower maintenance costs and also a low vibration environment for sample measurements. The sample chamber's temperature is controlled by a minimum amount ($\sim$ 150 cc) of liquid

helium produced by the cryocooler (see Fig. 4.13). This liquid helium flows up, to cool the sample chamber (in contact with the cooling annulus), due to the pressure difference between the cooling annulus, at moderated vacuum, and the bucket (which controls the 4 K plate), at 1 atm. Two cooling flow modes are available in DynaCool: the *main flow mode* and the *low temperature flow*.

In the **main flow mode** helium gas (at 4.2 K) in the bucket flows up through the counter-flow heat exchanger (CFE), reaches the mass flow controller - at room temperature - and then back down the CFE into the cooling annulus. With this mode temperatures of 10 K are possible to attain. When lower temperatures are needed and the system reaches the 10 K, the **low temperature mode** is activated instead of the main flow mode and the liquid at 4.2 K from the bucket is expanded through the capillary flow impedance. Since there are different pressures at the inlet and outlet of the impedance (1 atm and 10 Torr, respectively), some of the helium evaporates resulting in a mixture of liquid and gas at about 1.7 K that flows to the bottom of the cooling annulus (also known as pot) [31]. The system, as the pot begins to fill, is simultaneously controlling the level of liquid in the pot as well as the flow rate of gas, by the use of a liquid level sensor (in the cooling annulus), a heater on the impedance and a heater on the pot. The helium, using the circulation pump, is returned to the bucket, being cooled again by the cryocooler and reused. The DynaCool also features an integrated cryopump for high-vacuum and a vacuum gauge for controlling the sample environment.

The magnet system is a TiNb 9T superconducting coil conducting-cooled one (by the second stage at the cryocooler), whose current is controlled with precision by a hybrid digital/analog magnet controller. Both temperature of the magnet and the cryostat is monitored with the help of three thermometers localised at three different places of the PPMS. In addition, extra thermometers can also be monitored for particular applications. A very effective integrated magnetic shield screens the user and nearby instrumentation from magnetic stray fields being of great importance in situations where a better laboratory space utilisation is required (Fig. 4.12). At the bottom of the sample chamber, there is a 12-pin connector pre-wired to system electronics which allows us to plug in removable sample holders ("pucks") for convenient access to sample mounting as well as to change from different options of physical properties measurements that can involve coilset pucks. Two different options were used in this work: the *Electric-Transport Option* (ETO) and the *Vibrating Sample Magnetometer* (VSM), and will be described in the next two subsections.

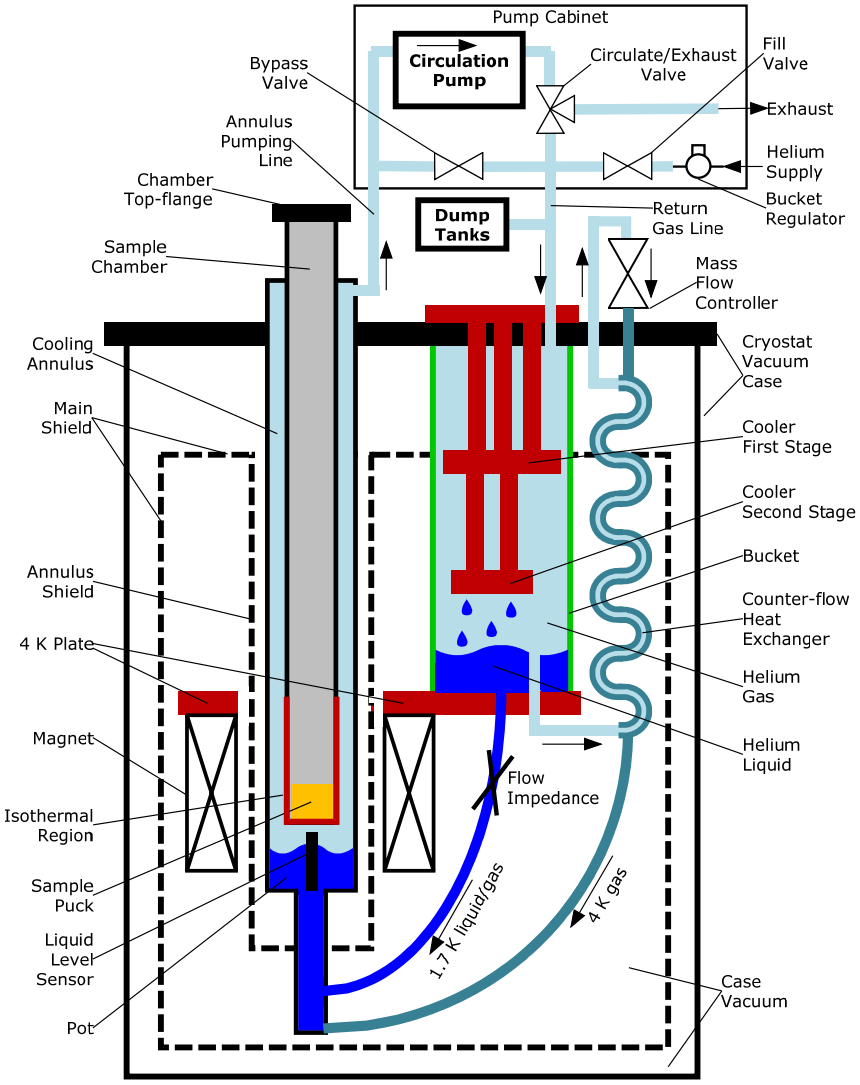

Fig. 4.13 The DynaCool Cryostat showing the components of the Cryostat, Chamber Temperature, and Magnetic Field Control Systems [31].

4.4.2 Resistivity measurements

The resistivity measurements were performed using the ETO option of the PPMS system; it contains two separate channels, each one with dedicated electronics which consists of a precision current source and voltage preamplifier coupled to a digital signal processor and allows a simultaneous, continuous resistance measurement of two different samples. Usually a sinusoidal AC drive current is applied and a AC voltage response is measured that is, the resistance is measured using the typical AC mode, where the digital-signal processor performs the functions of a lock-in amplifier. The advantage of the AC mode is its intrinsic high signal/noise ratio and immunity to spurious, small DC voltages arising from, e.g., thermoelectric effects.

In the ETO option a sample puck with three channels with gold-plated pads (I+, V+, V − and I−) is used to operate in one of two modes: the **2-wire mode**, used for high impedance ($2\,\mathrm{M\Omega} - 5\,\mathrm{G\Omega}$) and the **4-wire mode** (used in this work), for low impedance ($\mu\Omega - 10\,\mathrm{M\Omega}$)measurements. For low impedance samples usually a problem arises when measuring the resistance: the contact resistance due to the wires resistance is indistinguishable from the load resistance. The 4-wire mode overcomes this problem. In this case, the load resistance has four contacts attached: the current is applied via the two outermost contacts while the two innermost are connected to a voltmeter (the input should be at high impedance in order to prevent the flow of current in the innermost wires)(Fig. 4.14). As a result, the voltage drop recorded takes place between the two inner electrodes and any resistive contribution from them is eliminated.

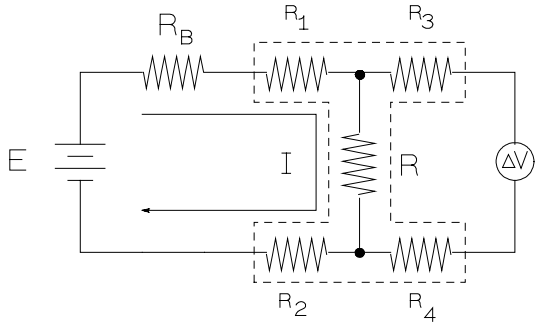

Fig. 4.14 Scheme of a circuit for the 4-wire mode [32].

However, the voltage reading depends on some factors:

- ohmic and low resistance contacts are essential to obtain good data (Ag paint is commonly used to make the contact between the wires - usually Au 25 μm wires - and the sample);

- the sample should have a regular geometry and should be homogeneous and isotropic;

- a good thermal contact between the metallic puck and the sample should be obtained and at the same time the latter should be electrically isolated from the ground - to do so, a thin layer of cigarette paper is paint on both sides with a small amount of GE low-temperature varnish in order to stick to the puck and to the sample;

- for any 4-wire measurement where the gain is higher or equal than 300 (low resistance samples), a frequency of $\sim 18 - 21\,\mathrm{Hz}$ should be used because there is a servo in gain = 300 stage that will attenuate signals slower than $\sim 5\,\mathrm{Hz}$ resulting in hysteresis in $I - V$ and phase shift in resistance measurements [33].

- the common-mode leakthrough of the voltage amplifier (the lower the common-mode rejection ratio of the electronics, the higher its value) is an important term to consider when dealing with small resistance measurements: residual resistance or even negative resistance can be observed for low resistances, specially in superconductors due to this effect. To minimise this problem, the contacts in a sample should have the same distance between each other and a significant difference in contact resistance between the two outermost contacts should be avoided, which sometimes is a hard task to accomplish [33, 34].

According to Ohm's law, $V = RI$, for a given current I that flows through a resistance value R, one can measure the voltage drop and obtain R. From the latter one can calculate the resistivity assuming that the sample has one regular geometry so that

$$\rho = R(\frac{A}{L}) \tag{4.11}$$

where L is the length and A the cross-sectional area of the conductor. When the sample is thick enough that its thickness is much bigger than the probe spacing ($h \gg a$), or when the sample is thin enough that $h \ll a$, different equations have to be taken into account for the resistivity calculation instead of the above one:

$$\rho = 2\pi\, a\, (\frac{\Delta V}{I})\,,\ h \gg a \tag{4.12a}$$

$$\rho = \frac{\pi}{\ln(2)}\, h\, (\frac{\Delta V}{I})\,,\ h \ll a \tag{4.12b}$$

4.4.3 Magnetometry measurements

The magnetometry measurements, such as the zero-field-cooled/field-cooled ZFC/FC susceptibility curves, $M(T)$, and the applied-field dependence of the magnetisation, $M(H)$, were accomplished using a vibrating sample magnetometer, the VSM option of the DynaCool PPMS. This option consists essentially of a VSM linear motor transport (head), which holds the rod (that contains the sample) in place using a magnetic-locking mechanism, a coil set puck, which contains the detection coils and a thermometer for monitoring the sample's temperature, and electronics to operate the linear motor transport and detect the pickup coils' response using the MultiVu software application.

The VSM, in its most usual form credited to Foner [35], works on the following principle: a magnetic sample, mounted on a carbon finer rod, oscillates inside a set of two Cu coils connected in phase opposition (first order gradiometer) and placed in a uniform magnetic field region, producing a changing magnetic flux. As a consequence, an electrical signal is induced in the coils, being amplified and synchronously[3] detected with the sample's movement by a lock-in amplifier, providing a good signal-to-noise ratio. In fact, the lock-in filters out other frequencies different from the vibration frequency, allowing the distinction between very small signals and the background noise. That signal is given by Lenz's law:

$$U = -\frac{d\Phi}{dt} = -\frac{\partial\Phi}{\partial z}\frac{\partial z}{\partial t}, \tag{4.13}$$

with $z(t)$ standing for the vertical position of the sample with respect to the coil. Assuming that the sample vibrates with frequency ω and amplitude A, the signal will be proportional to the magnetic moment, m, of the sample:

$$U = -\frac{d\Phi}{dt} = -k\,m\,G(z)\omega A\cos(\omega t), \tag{4.14}$$

where k is a calibration constant and $G(z)$ is a sensitivity function, i.e., the dependence of VSM output on sample position, with a shape approximately as the one given in Figure 4.15.

In this work, all samples were measured with the same frequency of 40 Hz, and oscillation amplitude, A $\sim$ 2 mm, at the central position of coils, where $G(z)$ is approximately constant, due to a optimal choice of the value of the ratio of

[3]This is only possible to achieve due to an optical linear encoder that controls with precision the position and amplitude of oscillation, the former being used as a reference for the synchronous detection.

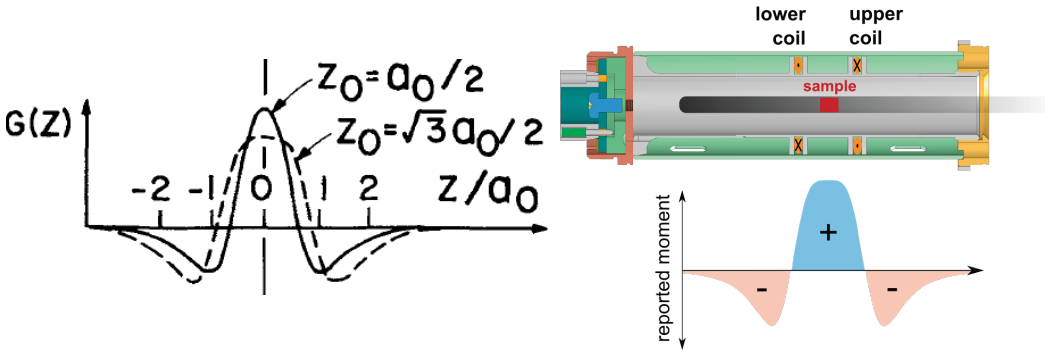

Fig. 4.15 Left: $G(z)$ function for coils with radius a_0, separate by $2z_0$, in the gradiometer configuration. In the case of DynaCool VSM, $z_0 = \sqrt{3}a_0/2$. [36]; Right: View of a sample (red) positioned in the VSM gradiometer with the large bore coil set shown as an example. Below is shown the coil response function (sample's reported magnetic moment as a function of its location in the coils) [37].

the distance between coils to their radius, $2z_0/a_0 = \sqrt{3}$ (Fig. 4.15). The moment is usually reported in *emu* units ($1\,\text{emu} = 1\,\text{erg/Oe}\,(\text{CGS}) = 10^{-3}\text{J/T}\,(\text{SI})$).

Chapter 5

Results

5.1 Exploratory work of the phase diagram

Our work started with the synthesis of three samples of nominal compositions, $FeSe_{0.88}$, $FeSe_{0.85}$, and FeSe labelled samples #1, #2 and #3, respectively. These compositions were chosen as representative of the slightly Se deficient side of the phase diagram around the 1:1 line that was reported to be the most promising for the synthesis of superconducting β-FeSe. As the three syntheses of this exploratory work were successful, the results are reported here. However, one should bear in mind that we were testing the synthetic conditions as well as commissioning new equipment and analytical procedures with this first batch of samples.

5.1.1 Synthesis

The nominal stoichiometric amounts of pure Fe (99.998 %) and Se (99.999 %) were weighted in an analytical balance and subsequently ground and mixed with a pestle and mortar. Both operations were performed under air as we did not have, at that time, access to a glovebox to perform these operations in vacuum or under an inert atmosphere. Therefore, we took care to speed up these operations in order to minimise the exposure to air. The finely ground mixtures were placed inside quartz tubes of 2 mm diameter that were sealed with an oxyacetylene flame. While sealing, we maintained inside the quartz tubes a primary vacuum. The samples were later heated in a TERMOLAB furnace, described in chapter 4. The following temperature profile was used for the syntheses: heating was performed at a constant rate of 1.5 °C/min up to 650 °C. This temperature was held for a period of 24 hours and then decreased to room temperature at a constant

rate of 3 °C/min for the sample #1 and at 1.5 °C/min for the other two samples. The total time in the furnace was 35 hours. The sample #1 was reground and sealed again in a quartz tube for an annealing. The temperature profile for this annealing was similar to that used for the synthesis but with a slower cooling rate of 1.5 °C/min . The other two samples had only one temperature cycle and were in fact produced sharing the same furnace while the sample #1 was doing the annealing. No further cycle in temperature was applied to the samples #1, #2 and #3[1] because after having performed the annealing on sample #1, the results were disappointing as we shall show later on.

5.1.2 XRD analysis

The samples were analysed using the Bruker AXS D8 ADVANCE X-ray diffractometer described in Chapter 4. As the samples came out of the furnace in the shape of solid rods, a small piece of each rod was used for the X-ray analysis. This piece was ground to a powder of fine homogeneous grain size and placed on a low-background amorphous Si sample holder that features a plastic cover (with a small knife-edge to reduce background) that minimises the contact between the sample and air. After carefully determining the height of the sample by scanning the primary beam, to get a correct $2\theta_0$ reference, the diffractograms were obtained in the 2θ range of $10 - 130°$ with a step size of $0.005°$ and an accumulated time per step of 0.5 s. The diffractograms are presented in Figures 5.1, to 5.2. Identification of the phases was performed by the search-match procedure of EVA (version 4.0) on the ICDD/JCPDS database. The composition of the samples was determined by an analysis of the diffractograms using the Rietveld method. The crystallographic data of each phase was input to the Rietveld refinement program TOPAS (version 5.0). The refined model included as parameters the percentage of each phase. Profiles of the Bragg reflections were determined from first principles based on the optics of the instrument. The convolution procedure that determined the shape profiles is that described by Cheary and Coelho [38], known as the *fundamental parameters approach*. The model includes a refinement of the cell parameters, atomic positions, site occupancies, isotopic temperature factors and two parameters to describe grain size and microstrain broadening of the peaks. For the microstructure parameters, we adopted a lorentzian profile for the grain size distribution and a gaussian profile for the microstrain distribution, as these are the most common. For minority phases contributing less than 2% to the diffractogram, these parameters were fixed at the reported ideal values.

[1] For sample #1 we show first the discussion of its first heating cycle.

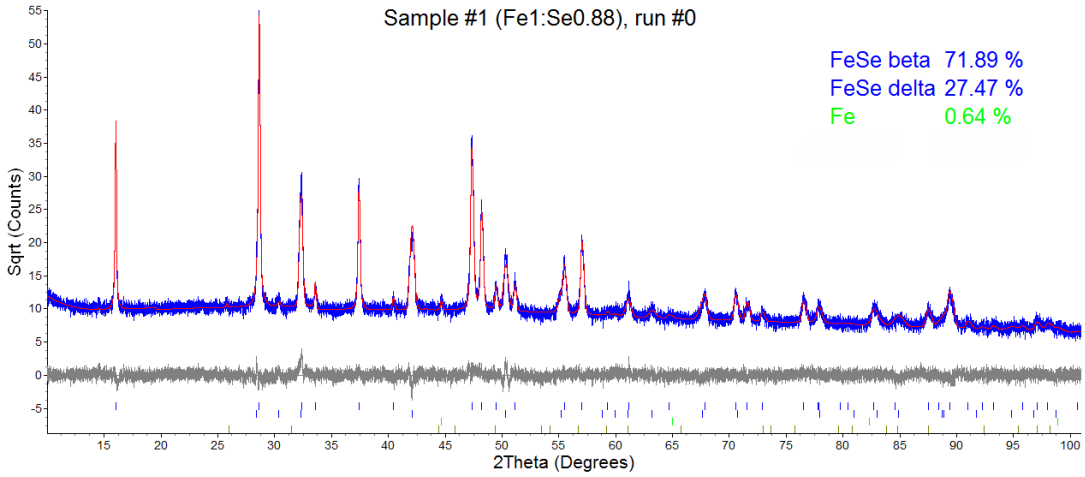

(a)

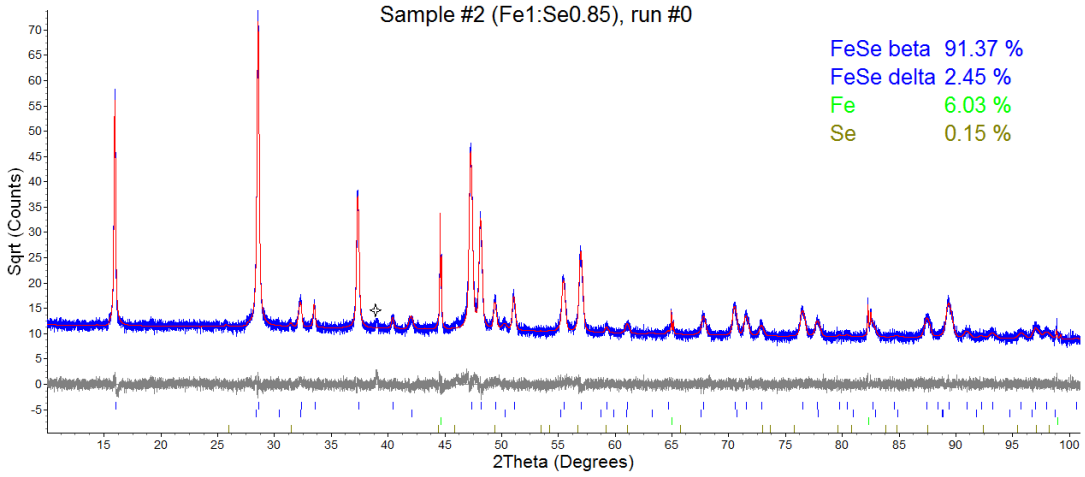

(b)

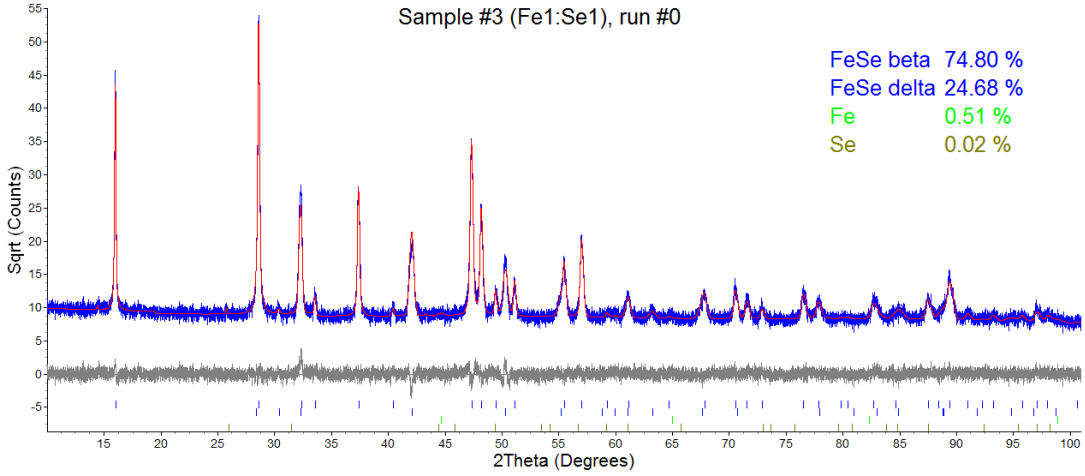

(c)

Fig. 5.1 Diffraction patterns of samples #1, #2 and #3, showing the phases and respective percentage determined by the Rietveld method.

Analysis of the XRD pattern revealed that for the three samples we successfully produced the desired β-FeSe phase as majority phase. The best result was achieved by sample #2 of nominal composition $FeSe_{0.85}$ for which a high amount of $\sim 91.4\%$ of β-phase was reached. For the three cases, the second major phase was the δ-FeSe that was present as $\sim 27\%$ for sample #1 and $\sim 24.7\%$ for sample #3. Free α-Fe was also present in sub-percent level in samples #1 and #3 but reached 6% in sample #2 where it is present in a quantity higher than δ-FeSe. It should be pointed out that the starting deficiency of Se content does not show up as Se vacancies in neither β- or δ-phases but rather as a precipitate of α-Fe of the excess metal. This is in agreement with the reported work on the chemical stability of $FeSe_{1-x}$ using neutron powder diffraction [20]. Small traces of free-Se may be present in samples #2 and #3 but are close to the detection limit of the technique which is typically around 1%. No further extraneous phases were identified and the residual difference in the Rietveld refinement is very clean.

It is worth noting that the presence of the δ-FeSe phase is clearly identified by the Bragg peak at the position $2\theta = 32.33°$ whereas the presence of free-Fe clearly shows up as a sharp peak at $2\theta = 44.67°$. A summary of the results of the XRD analysis are shown in Tables 5.1 and 5.2.

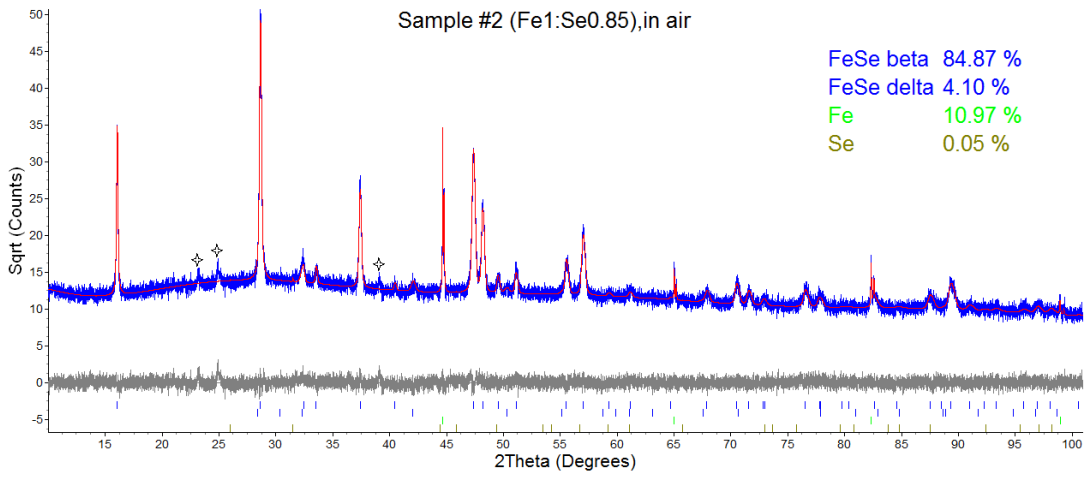

Fig. 5.2 Diffraction pattern of sample #2, after one month of air exposition.

Sample #2 was remeasured after one month of exposure to air in order to test the stability of the samples to air. The XRD pattern is shown in Figure 5.2. Interestingly, and surprisingly, we found that the Fe content increased significantly from 6 to 11% at the expense of β-FeSe phase that decreased to 84.87%. In addition, we can distinguish very small unindexed peaks marked with a star in Figure 5.2 that may belong to an oxide phase of either Fe or Se. The position of

Table 5.1 Summary of the results from the Rietveld refinement of the XRD data for sample #1 to #3 after the preliminary run in furnace.
D, z, o, GOF and R_{wp} stand for crystallite size, fractional coordinate, site occupancy factor, goodness of fit and weighted pattern reliability factor, respectively.

	sample #1 run #0	sample #2 run #0	sample #3 run #0
β-FeSe (%)	71.9(7)	91.37(16)	74.8(6)
a (Å)	3.77239(6)	3.77308(8)	3.77218(6)
c (Å)	5.52285(16))	5.52318(13)	5.22282(15)
z_{Se}	0.2687(2)	0.26567(16)	0.2631(3)
D(nm)	162.8(19)	139.9(11)	163.3(19)
e_0	$7.28(5) \times 10^{-4}$	$8.11(5) \times 10^{-4}$	$7.15(6) \times 10^{-4}$
o_{Se}	1.096(5)	1.014(3)	0.982(4)
δ-FeSe (%)	27.5(7)	2.45(10)	24.7(6)
a (Å)	3.62410(14)	3.6261(7)	3.63442(14)
c (Å)	5.8810(4)	5.877(2)	5.8784(4)
D(nm)	$1.3(8) \times 10^3$	–	$4.8(1) \times 10^2$
e_0	$2.05(2) \times 10^{-3}$	$2.14(11) \times 10^{-3}$	$1.97(2) \times 10^{-3}$
o_{Se}	1.00(6)	1.00(6)	1.00(6)
α-Fe (%)	0.64(6)	6.03(11)	0.51(12)
a (Å)	2.8669(3)	2.86645(5)	2.867(3)
D(nm)	120(19)	266(7)	22(7)
Se (%)	–	0.15(3)	0.02(2)
R_{wp} (%)	11.61	9.49	11.45
GOF	1.13	1.11	1.11

Table 5.2 Summary of the results from the Rietveld refinement of the XRD data for sample #1 after annealing and sample #2 after one month exposure to air.

	sample #1 run #1	sample #2 in air
β-FeSe (%)	34.1(4)	84.9(2)
a (Å)	3.7687(2)	3.77549(10)
c (Å)	5.5164(4)	5.51856(18)
z_{Se}	0.2643(6)	0.2672(3)
D(nm)	222(12)	140(2)
e_0	$1.258(19) \times 10^{-3}$	$8.57(9) \times 10^{-4}$
o_{Se}	1.048(8)	1.108(5)
δ-FeSe (%)	57.9(4)	4.1(2)
a (Å)	3.6215(2)	3.6253(13)
c (Å)	5.8798(4)	5.876(4)
D(nm)	$5.7(9) \times 10^{2}$	$8(3) \times 10^{1}$
e_0	$1.1822(13) \times 10^{-3}$	$1.8(3) \times 10^{-3}$
o_{Se}	1.00(6)	1.00(6)
α-Fe (%)	1.5(3)	10.97(12)
a (Å)	2.943(5)	2.8667(6)
D(nm)	7.6(18)	$4.26(18) \times 10^{2}$
Se (%)	–	0.05(19)
Fe_3O_4 (%)	2.89(11)	–
a (Å)	8.3923(4)	–
D(nm)	$2.6(5) \times 10^{2}$	–
Fe_3Se_4 (%)	3.59(15)	–
R_{wp} (%)	14.03	8.99
GOF	1.57	1.06

the peaks was tested against all iron oxide phases present in the JCPDS database but no good match was found. The same applies to selenium oxides, but as these structures are more complex, no definitive assignment could be made. In addition, mixed iron selenide oxides are known to exist with unidentified crystal structures. In any case, the oxide content appears to be minor after one month of exposure to air. According to the literature [39], FeSe gains a layer of selenium oxide (mainly Se_3O_8) after relatively short (a few days) exposure to air.

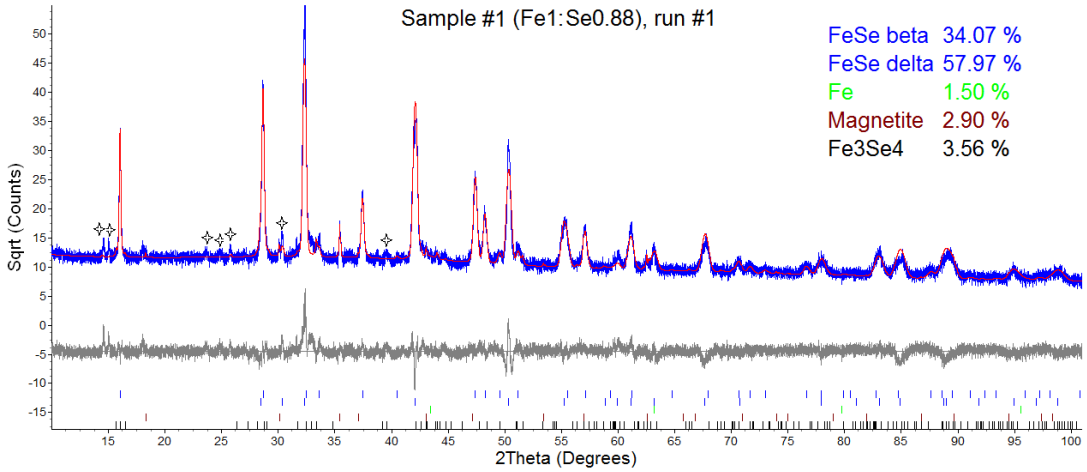

Fig. 5.3 Diffraction pattern of sample #1, after the second heating/cooling cycle.

As stated before, sample #1 was submitted to a second heating/cooling cycle. The X-ray analysis after the second cycle shows a major degradation of the sample (Fig. 5.3). It was found that β content of the sample decreased roughly to half the content after the first cycle, whereas the percentage of the δ-phase roughly doubled. In addition, the free-Fe content increased, even if not enormously, but we now detect the presence of both magnetite (Fe_3O_4) and Fe_3Se_4. Very weak unidentified peaks show up in the diffraction pattern that may correspond to more complex phases.

5.1.3 Resistivity

The resistivity between 1.8 K and room temperature was measured using the ETO option of the PPMS DynaCool system. The Kelvin 4-point technique was used with gold wire contacts that were glued with silver paint on top of small cylindrical samples of $\sim$ 1.5 cm length and 2 mm diameter (Fig.5.4). This simple wiring method proved to result in low-resistance contacts that survived several cooling/heating cycles. Figure 5.5 shows the resistivity (conversion of resistance to resistivity values was performed using equation 4.12b) of sample

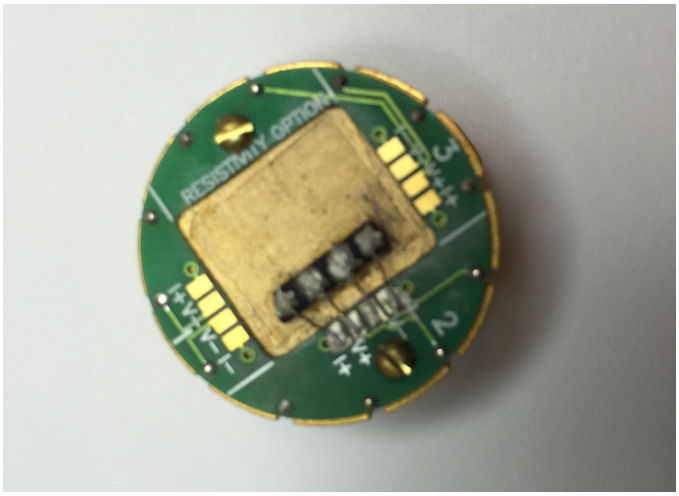

Fig. 5.4 Puck containing a FeSe sample showing the 4-point contacts made between the sample and puck using a gold wire and silver paint.

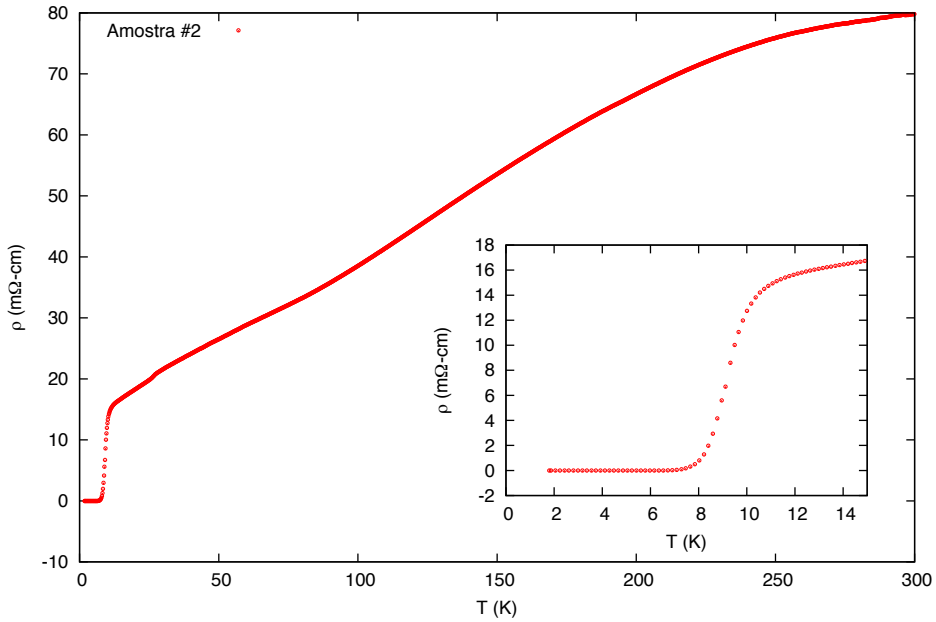

Fig. 5.5 Resistivity measurement performed from 1.8 to 300 K for sample #2. The inset shows the data between 1.8 and 15 K.

#2 after the synthesis. It is clearly superconducting at low-temperature, with a $T_{\text{onset}} = 10\,\text{K}$ and $T_0 = 7.5\,\text{K}$. These values are similar to those obtained in good quality polycrystalline samples reported in the literature. In the normal state the sample displays a metallic behaviour. Between room temperature and the onset of superconductivity, the resistivity decreases $\sim 80\,\%$. In order to better analyse the resistivity curve, we performed a calculation of the derivative of the

resistivity as a function of temperature using a numerical derivative based on a centred 5-point formula. The graph is shown in Figure 5.6.

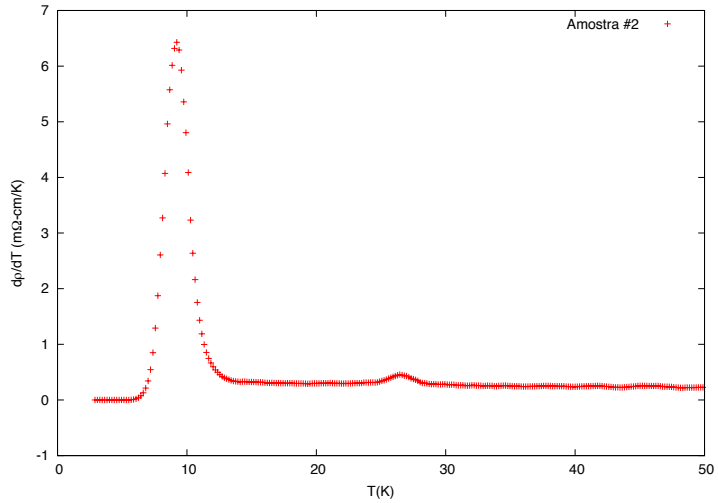

(a)

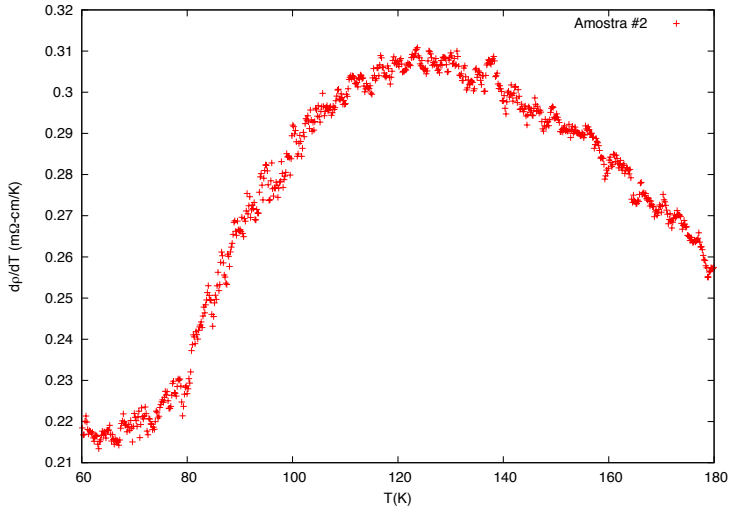

(b)

Fig. 5.6 Temperature derivative of the resistivity using a numerical 5-point centred formula. It shows (a) a large peak at $T_c = 9.2\,\mathrm{K}$ and a small peak at 26.5 K and (b) a small broad peak at $\sim 120\,\mathrm{K}$.

In addition to the big peak in $d\rho/dT$ corresponding to the superconducting transition, another small peak is found at $\sim 25\,\mathrm{K}$. Such a minor anomaly was also observed by Chang *et al.* [15]. There is, at present no sound explanation for such anomaly. It may well be an artefact due to the inconel electrical feedthrough in the sample chamber of Quantum Design PPMS systems that are known to produce a small signal in the 25-35 K region. Another broad peak in $d\rho/dT$ is

observed at $\sim 120\,\mathrm{K}$, probably a signature of the structural transition from the tetragonal β-FeSe to the orthorhombic low-temperature form.

5.1.4 Magnetic hysteresis cycles

The magnetisation curves in a full hysteresis cycle were measured for the three samples with the VSM option of the DynaCool. Figures 5.7, 5.8 and 5.9 depict these hysteresis cycles measured at 1.8 K. Clearly, the three samples show distinct magnetic behaviour. Samples #1 and #3 show a typical ferrimagnetic curve, not saturated, even in the maximum applied field. The remanent magnetisation and the shape of the curves are similar to those of hexagonal δ-FeSe, as reported by Hirone [40]. The high coercivity at low temperature is also characteristic of this phase which has a strong uniaxial anisotropy. The coercivity decreases significantly as the temperature increases, as expected (Fig. 5.10). This is due to a decrease of the barrier for magnetisation reversal, which is determined by the temperature-dependent magnetic anisotropy constant. In contrast, hysteresis cycle of sample #2 is typical of a very soft ferromagnet with a high saturation magnetisation. It is compatible with the expected curve of the small amount of free α-Fe present in the sample. There is almost no hysteresis and the behaviour is superparamagnetic like and results from finely dispersed Fe grains in a mostly inert β-FeSe matrix. Thus these results are fully compatible with the composition determined from the X-ray diffraction analysis.

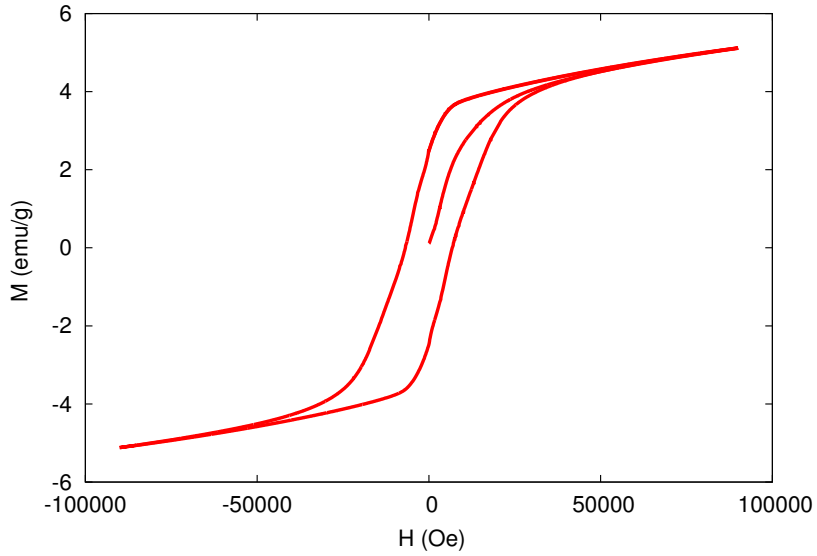

Fig. 5.7 Magnetic hysteresis cycle measured at 1.8 K for sample #1.

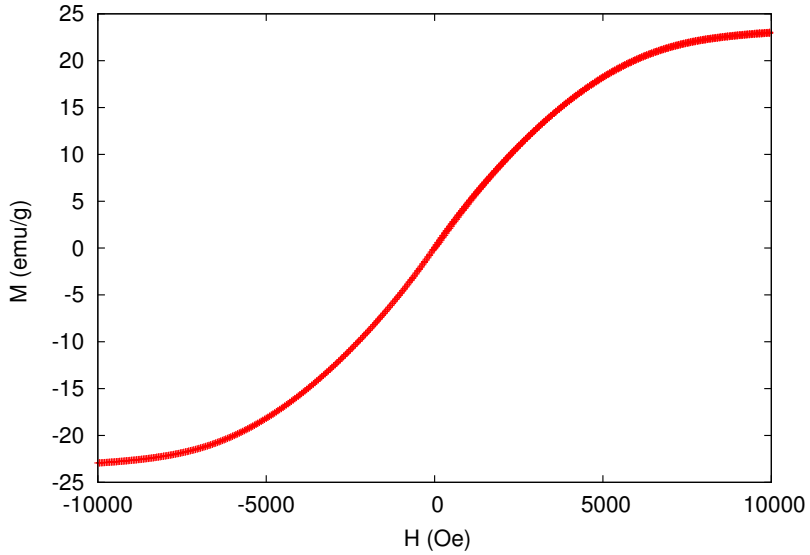

Fig. 5.8 Magnetic hysteresis cycle measured at 1.8 K for sample #2.

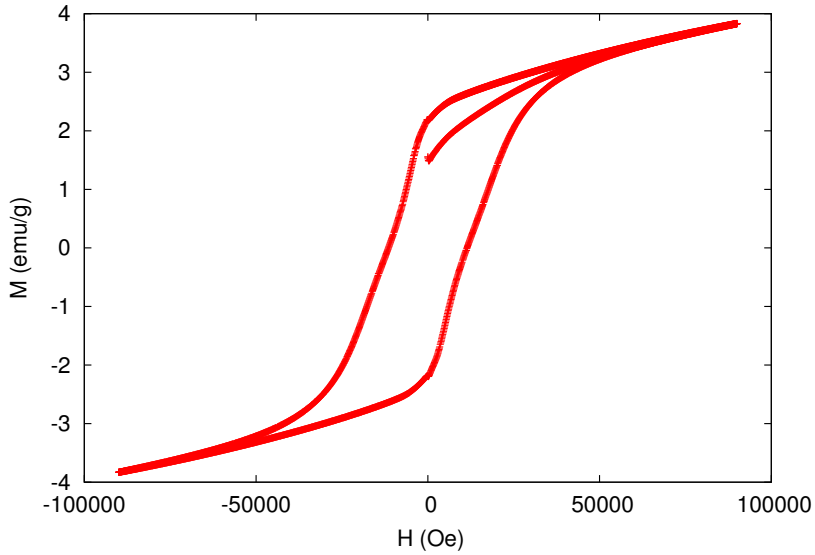

Fig. 5.9 Magnetic hysteresis cycle measured at 1.8 K for sample #3.

5.1.5 Meissner effect

Superconducting samples show the Meissner effect, that is the expulsion of magnetic field below the superconducting transition. As such, the measurement of the thermomagnetic $M(T)$ curves under a small applied magnetic field are an excellent probe of superconductivity because the Meissner effect shows up as a sudden decrease of the magnetisation below T_c. We have measured the $M(T)$ curves with a small applied magnetic field of 100 Oe; the results are shown in Figure 5.11. The three samples clearly exhibit the Meissner effect. Samples

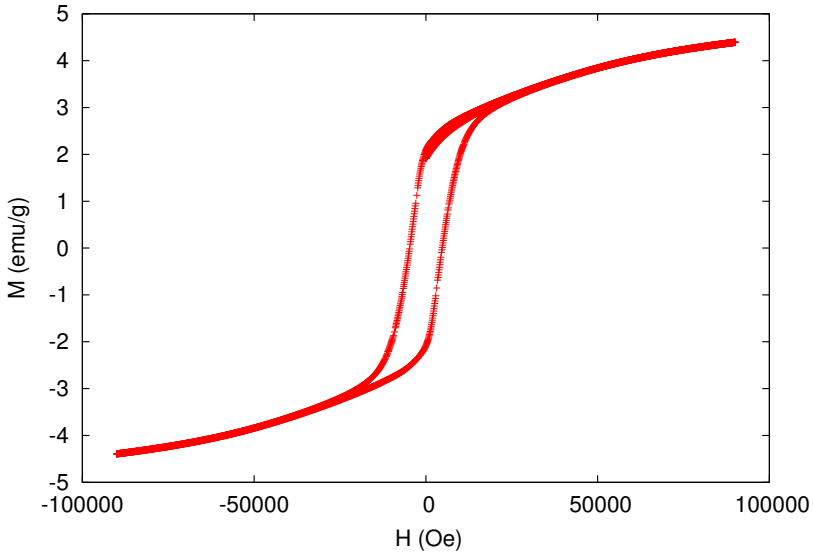

Fig. 5.10 Magnetic hysteresis cycle measured at 100 K for sample #3.

#1 and #3 even show a negative magnetisation. Sample #2, which is strongly ferromagnetic due to the free-Fe contamination, does not achieve a negative magnetisation but nevertheless the Meissner effect is clearly seen as a reduction of the magnetisation. The critical temperatures determined from the Meissner effect coincide with those determined from the resistivity curves.

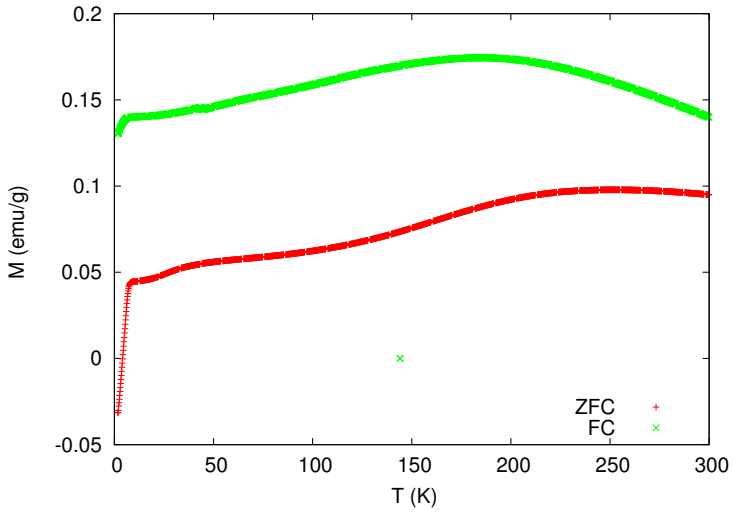

(a)

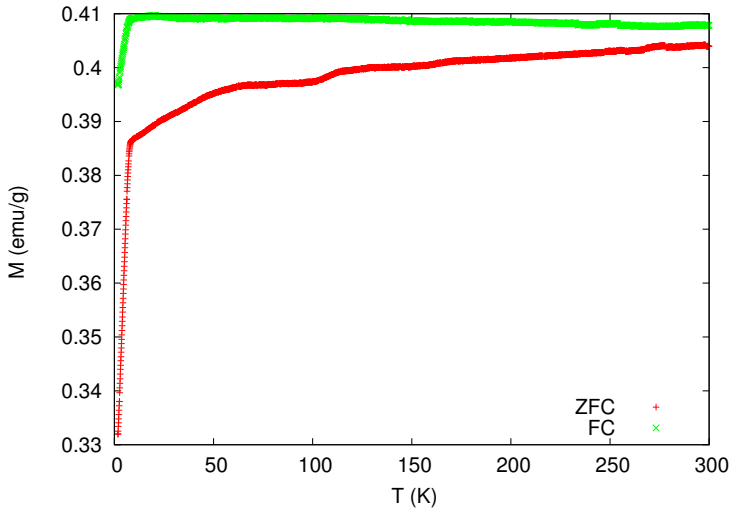

(b)

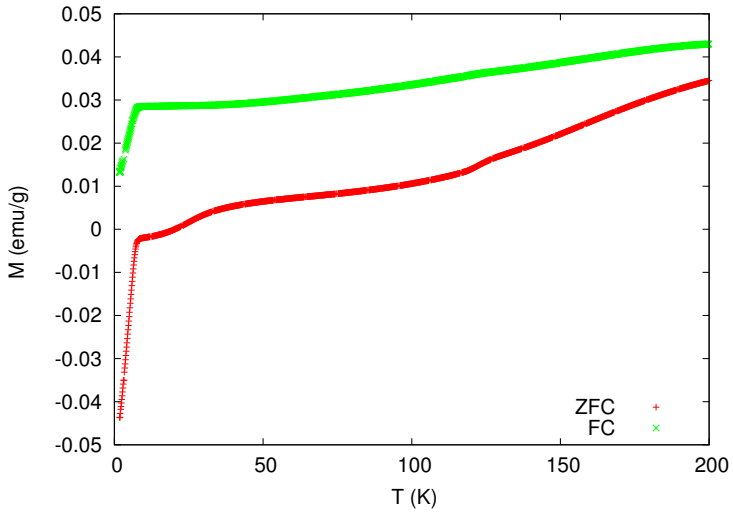

(c)

Fig. 5.11 From top to bottom: ZFC and FC curves for samples #1, #2 and #3 showing the Meissner effect.

5.1.6 Critical field

We have chosen sample #3, the one with the lowest free-Fe content to make a detailed study of the superconducting critical field. This study relies on measurements of small amplitude hysteresis cycles of magnetisation as a function of applied field. Such measurements are not possible for samples with a high remanent magnetisation that precludes a clear observation of the Meissner effect. In our case we have chosen to use a hysteresis cycle with an amplitude of 500 Oe. One such curve, measured at 1.8 K is shown in Figure 5.12. Starting from the

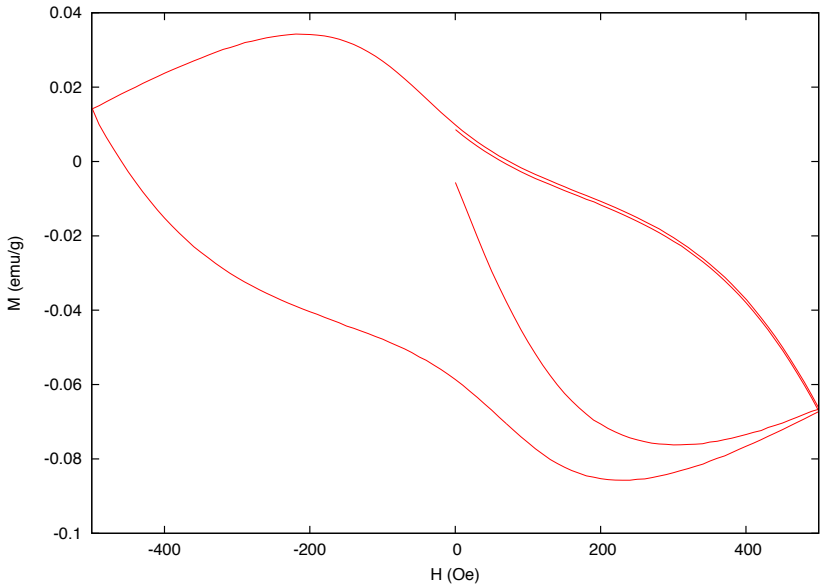

Fig. 5.12 Low-field magnetic hysteresis cycle of sample #3 at 1.8 K.

virgin ZFC state, the magnetisation initially decreases almost linearly with the applied field, that is, the sample shows a perfect diamagnetic behaviour, the magnetisation cancelling the external applied field in the interior of the material. After some field the magnetisation starts decreasing at a slower pace than the field and a minimum of the magnetisation occurs for some critical field H_{c1}. After H_{c1} the magnetisation indeed increases with applied field showing that the magnetic flux penetrates into the sample even if the sample still features zero resistivity. Superconductivity is only destroyed at a much higher field, H_{c2}. While cycling the magnetic field in this low-field region, we obtained the characteristic $M(H)$ hysteresis cycles of a typical hard type-II superconductor. The value of the critical field H_{c1} depends on the temperature. Close to T_c a much smaller field is enough to destroy the Meissner effect. $M(H)$ curves from which the critical H_{c1} values were derived are shown in Figure 5.13. The plot of the critical field H_{c1} as a function of temperature is shown as Figure 5.14. The

usual law

$$H_{c1}(T) = H_{c1}(0)\left(1 - \left(\frac{T}{T_c}\right)^2\right) \tag{5.1}$$

gives a good fit to the data. The fitted parameters are $H_{c1}(0) = 330\,(6)$ Oe and $T_c = 7.16\,(7)$ K. The fit is shown as a solid line in Figure 5.14.

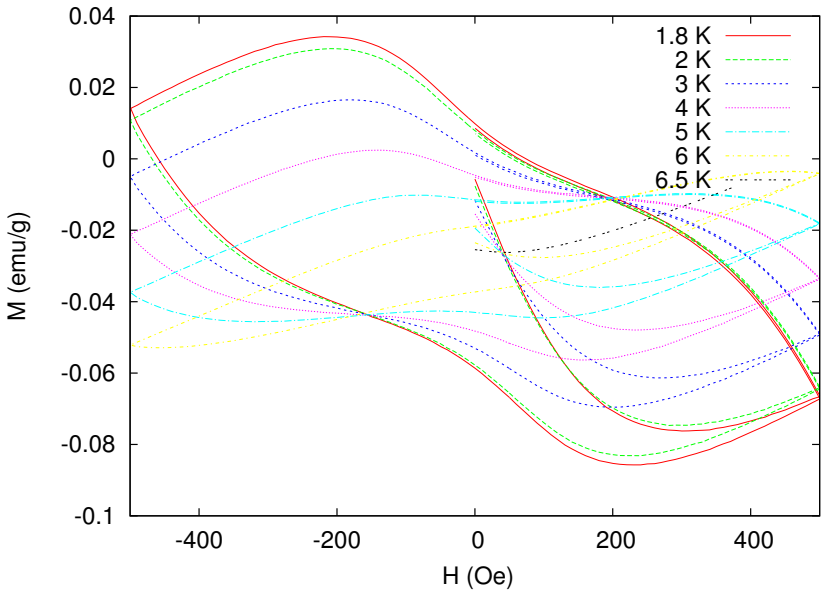

Fig. 5.13 Low-field magnetic hysteresis cycle of sample #3 from 1.8 K to 6.5 K.

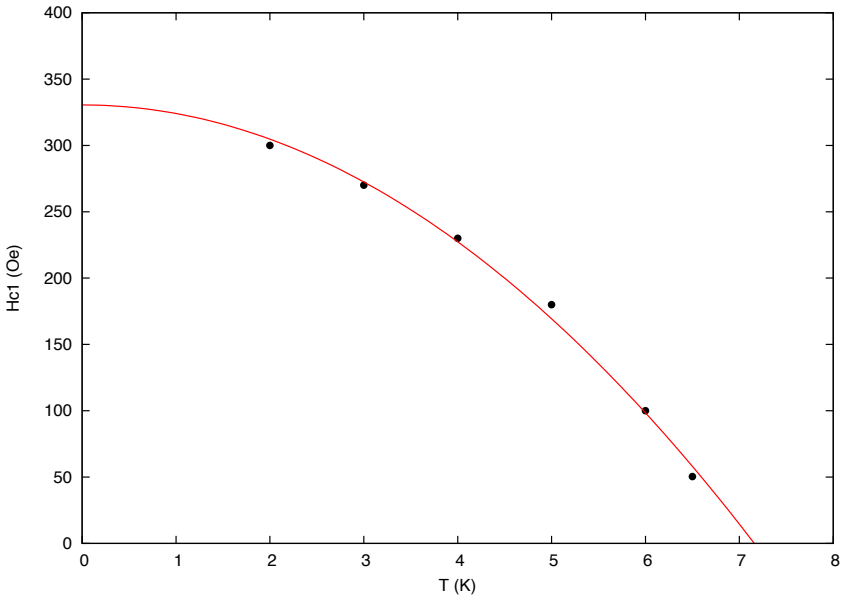

Fig. 5.14 Critical field H_{c1} as function of temperature for sample #3.

The explanation of the reversal magnetisation behaviour (hysteresis) of hard type-II superconductors is explained by the Bean's critical state model developed by C. P. Bean in 1962 [41]. This model is based on the idea that for $H > H_{c1}$ the magnetic field starts to penetrate into the superconductor as flux vortices creating the so-called Shubnikov phase. These vortices are pinned on the surface of the material and in defects (Bean-Livingston-barrier). This model can reproduce the typical shape of the superconductor hysteresis cycle that we found in our samples.

5.1.7 The "dolphin effect"

For samples containing a significant amount of δ-FeSe, exotic magnetisation cycles were measured for fields that are not strong enough to fully align the magnetic domains, bearing in mind the high coercivity of this material. One example of such cycle is depicted in Figure 5.15. As the coercivity increases at

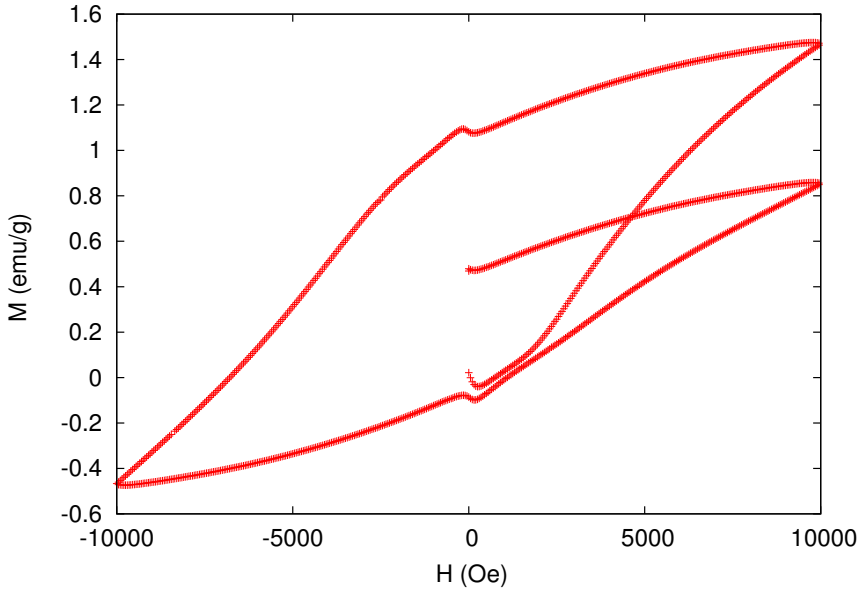

Fig. 5.15 Hysteresis cycle of sample #3 measured up to 10 kOe at 1.8 K.

low temperature, such strangely shaped hysteresis cycles are easier to observe at low temperature. Note that the cycles are off-centred in the vertical axis and are strongly asymmetric. Near the zero crossing point of the field, one observes very clear the Meissner effect. In Figure 5.16 a sequence of hysteresis cycles is presented as a function of temperature, showing the funny-looking cycles transforming into normal cycles as the temperature increases. Of course the "dolphin effect" is not a characteristic of superconductors but rather a characteristic of some

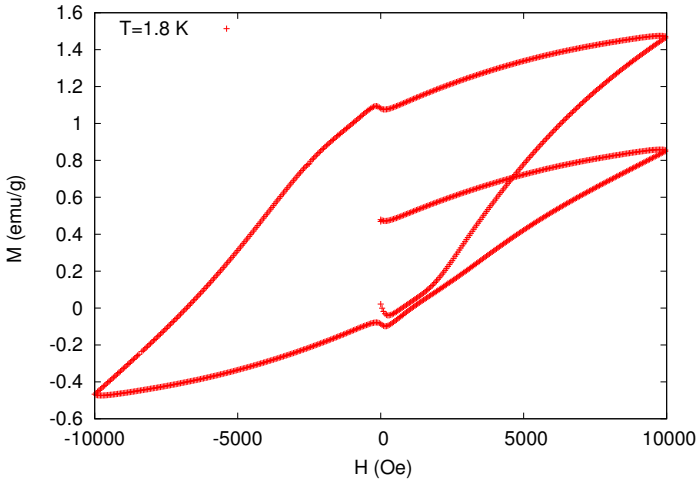

(a)

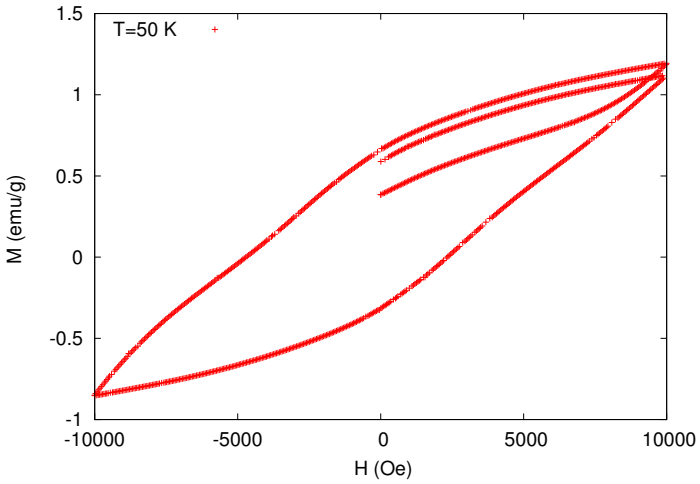

(b)

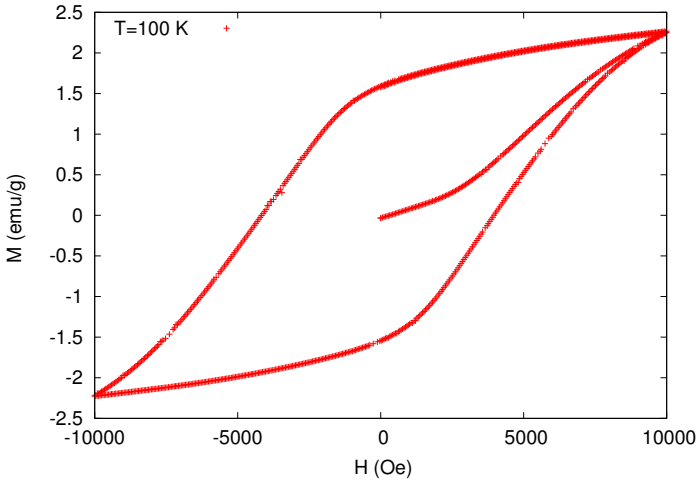

(c)

Fig. 5.16 Sequence of funny-looking hysteresis cycles showing the transformation into normal cycles with increasing temperature.

hard magnetic materials. The fact that we observe both Bean's like hysteresis cycles at low field and dolphin-like hysteresis cycles at higher fields illustrates a peculiar characteristic of FeSe superconductors, the "pacific" coexistence of type-II superconductivity and hard ferro/ferrimagnetism. However, it should be stressed that the magnetism does not originate from the superconducting β-FeSe phase but rather from the non-superconducting but ferrimagnetic δ-FeSe phase.

5.2 Fine-tuning the synthesis of β-FeSe

After the successful exploratory work, we synthesised and characterised six additional samples with a wider range of nominal compositions larger than the previous one: $FeSe_{0.85}$ (#1), $FeSe_{0.88}$ (#2), $FeSe_{0.91}$ (#3), $FeSe_{0.94}$ (#4), $FeSe_{0.97}$ (#5) and FeSe (#6). Compared to the previous one, we also changed the heating/cooling cycles as described below[2]. Samples #1 and #6 of the present run gave similar results to those of samples #2 and #3 from the exploratory run.

5.2.1 Synthesis

Weighting, grinding, etc., were performed following the previously specified procedure. In this run, an intermediate holding step at 430 °C was added to the cooling cycle. Thus, the heating was performed at a constant rate of 1.5 °C/min up to 650 °C, then held for 24 hours at that temperature. Then a cooling at a rate of 1.5 °C/min was performed to reach the intermediate temperature of 430 °C, which was held for 12 hours. After that period the furnace was switched off and the furnace door slightly opened in order to attain the room temperature as quickly as possible. After XRD and other measurements were carried out, the samples (properly sealed) were subjected to a second run of the same heating/cooling cycle to check if it would improve the amount of β-FeSe phase. In between cycles, we took care to store the samples in an evacuated glovebox.

5.2.2 XRD analysis

The diffractograms of the new samples were obtained using the same conditions as before and identification and quantification of the phases followed the same procedure as well. The diffractograms for the first heating/cooling cycle are presented in Figures 5.17a to 5.19b .

Analysis of the XRD patterns revealed the presence of three majority phases in the six samples, the β-FeSe phase at a higher amount, followed by the δ-FeSe and by α-Fe phase, this last one at a small amount. However, with increasing nominal composition of $FeSe_{1-x}$, the percentage of composition of β-FeSe and Fe phases decreases while the percentage of δ-FeSe phase increases (Fig. 5.20) at the expense of the other two, as already was found in run #0. The β-phase

[2]Whenever necessary we specify in addition to the sample batch number an additional number describing the furnace run. Run #0 means the exploratory run and subsequent runs are numbered #1 and #2.

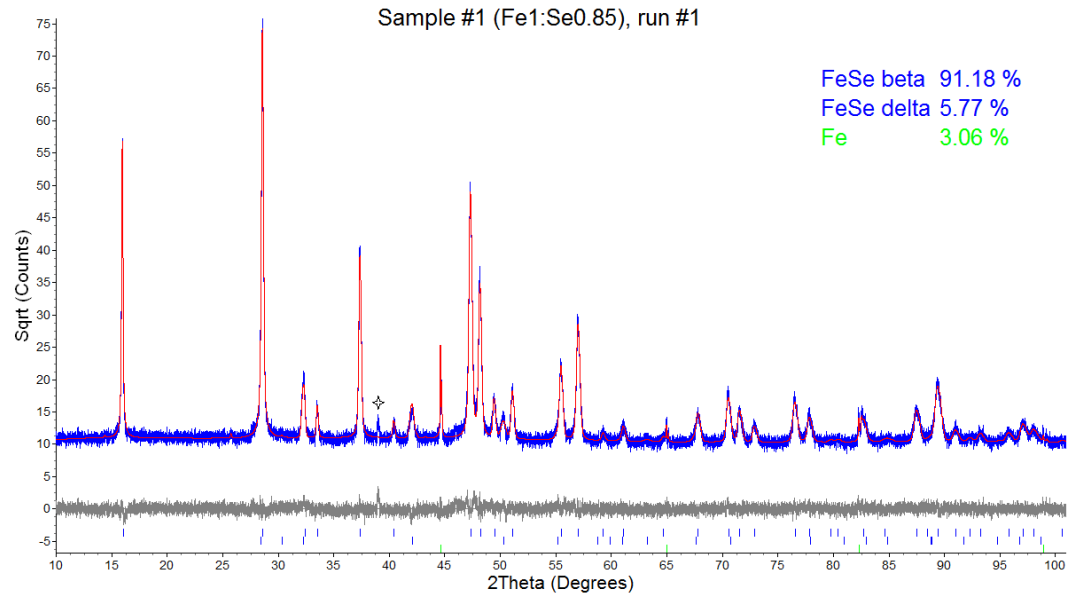

(a)

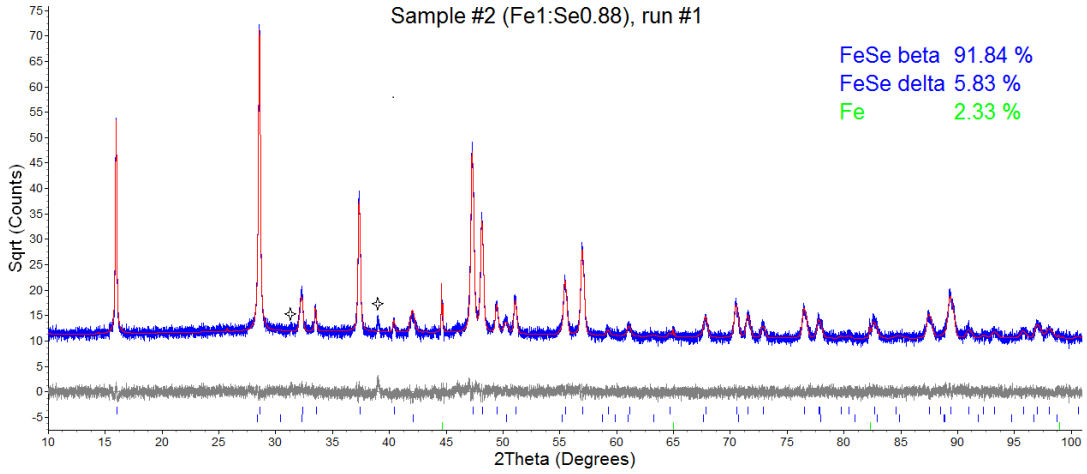

(b)

Fig. 5.17 Diffraction patterns of samples #1 and #2, showing the phases and respective percentage determined by the Rietveld method (run #1).

over δ-phase ratio attains a maximum of $\sim 15\times$ for sample #2 (0.88 at.%Se). Concerning impurity phases, none could be positively identified searching in the ICDD/JCPDS database. However, we noticed in the difference pattern from Rietveld refinements minor unindexed peaks at positions $2\theta \sim 31°$ and $2\theta \sim 39°$ for samples #1 to #4 and even smaller peaks around 14° for sample #6.

The composition of the samples determined from Rietveld refinement are given in Table 5.3. Comparing the results of Table 5.3 and Table 5.1 we can see that the new temperature profile afforded the sample with the highest β-content

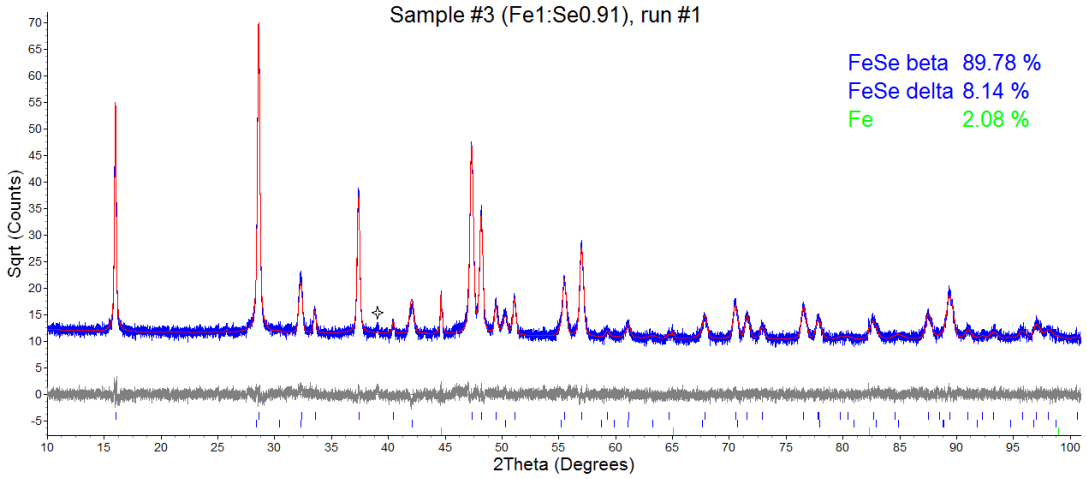

(a)

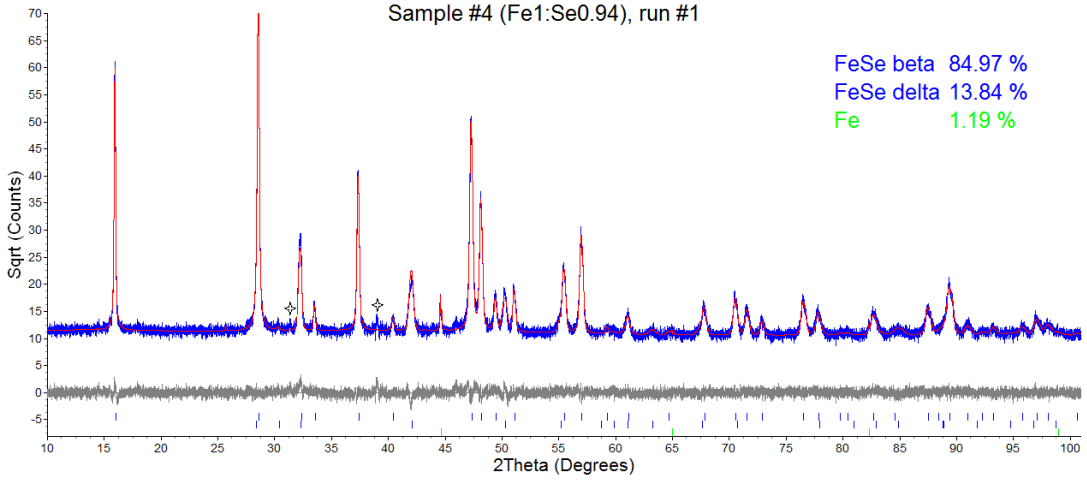

(b)

Fig. 5.18 Diffraction patterns of samples #3 and #4, showing the phases and respective percentage determined by the Rietveld method (run #1).

Table 5.3 Brief summary of the results from the Rietveld refinement of the XRD data for sample #1 to #6, run #1.

Nom. comp.	sample #1 Fe1:Se0.85	sample #2 Fe1:Se0.88	sample #3 Fe1:Se0.91	sample #4 Fe1:Se0.94	sample #5 Fe1:Se0.97	sample #6 Fe1:Se1
β-FeSe (%)	91.18(11)	91.84(13)	89.78(11)	84.97(11)	77.40(13)	77.03(13)
δ-FeSe (%)	5.77(10)	5.83(12)	8.14(10)	13.84(10)	21.77(12)	24.91(13)
α-Fe (%)	3.06(4)	2.33(5)	2.08(4)	1.19(3)	0.84(4)	0.06(3)
R_{wp} (%)	9.00	8.86	8.59	8.95	9.12	9.10

at a slightly different nominal composition (Fe1:Se0.88). For this composition,

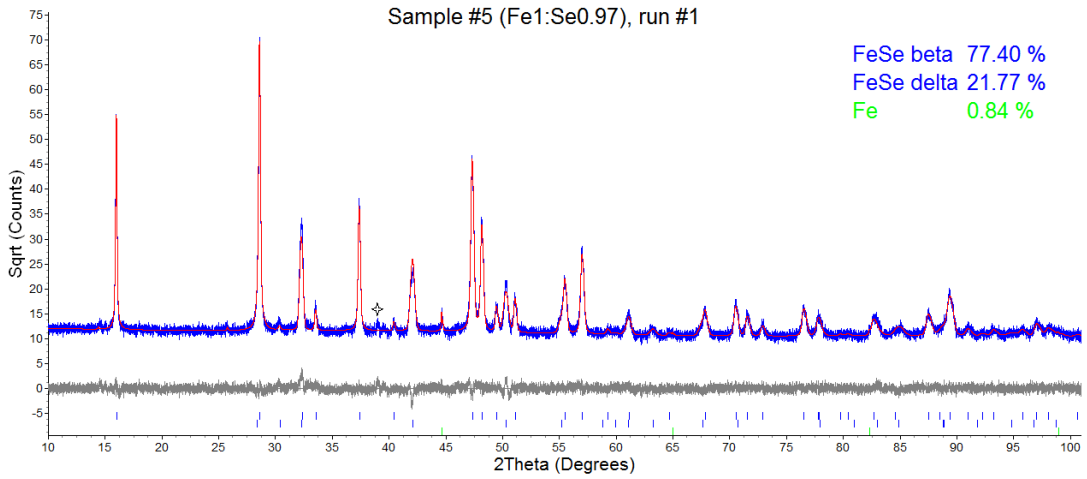

(a)

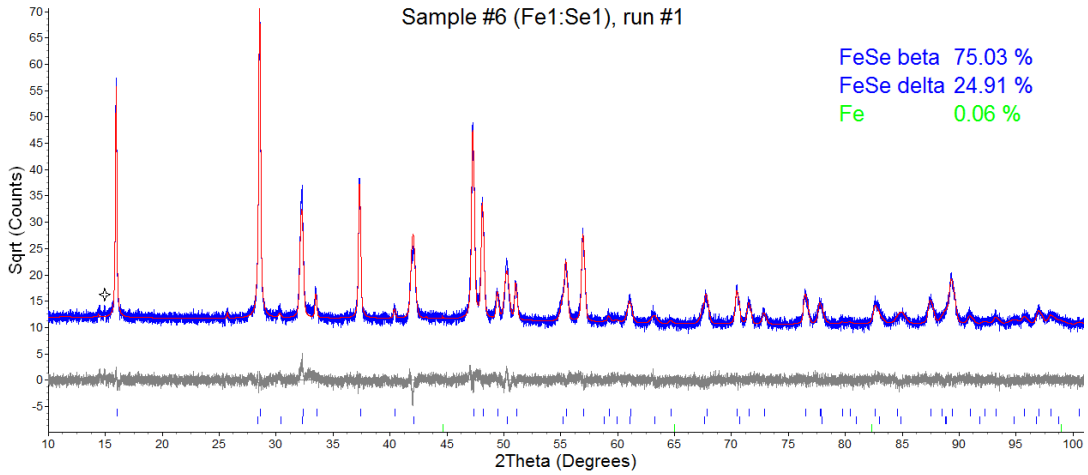

(b)

Fig. 5.19 Diffraction patterns of samples #5 and #6, showing the phases and respective percentage determined by the Rietveld method (run #1).

the new procedure changed the amount of β-FeSe phase from 72 to 92 %. The amount of the β-FeSe phase in sample #2 from run #1 is similar to that of sample #2 from run #0 (Fe1:Se0.85) but with a smaller Fe content (3% versus the former 6%), the amount of the δ-FeSe phase increasing, accordingly from 2.5 to 6%.

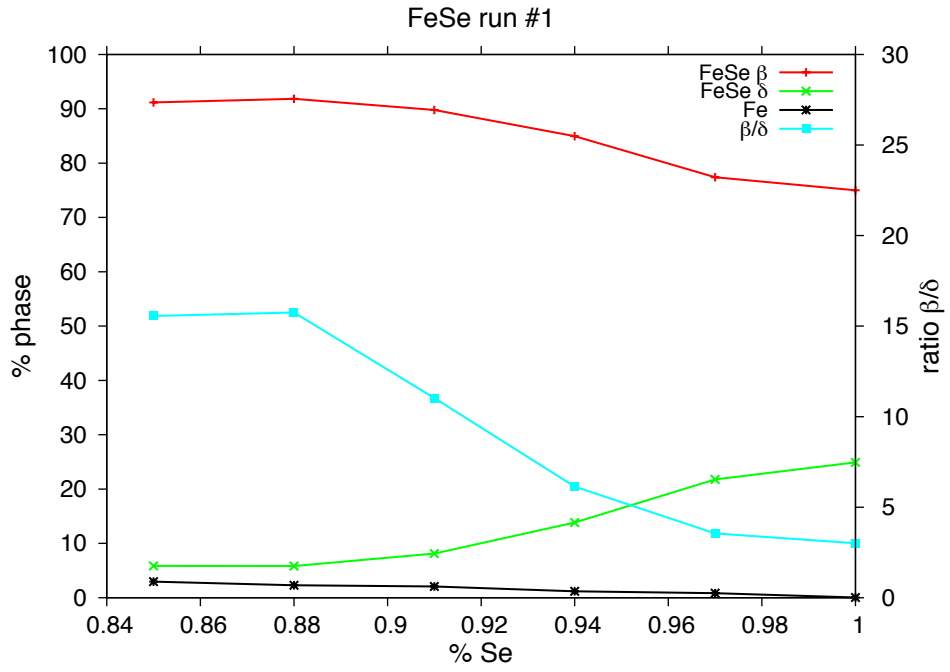

Fig. 5.20 Weight percentage of the phases present in the six samples of run #1 as function of the nominal composition. In addition, the curve of the β over δ ratio is also shown.

5.2.3 Resistivity

The resistivity of the samples was measured as a function of temperature using the same procedure as for run #0. As expected, all six samples were found to be superconducting at low temperature.

We have found that the onset temperature of superconductivity is not very sensitive to the starting nominal composition of the six samples. However, the width of the superconducting transition definitely is wider for those samples which have a lower β-phase fraction or higher Se content in the nominal composition, as shown in Figure 5.21.

5.2.4 SEM/EDS

SEM measurements were performed on all six samples (subjected to a longitudinal cut, in order to observe its inside) from run #1 using the SEM/EDS VEGA TESCAN described in chapter 4, to characterise them in terms of homogeneity and composition. All images were taken using the secondary electrons detector. The measurements were performed with a high voltage of 20 kV and a working distance of 15 mm. In most cases a magnification of 1 k× was used for imaging

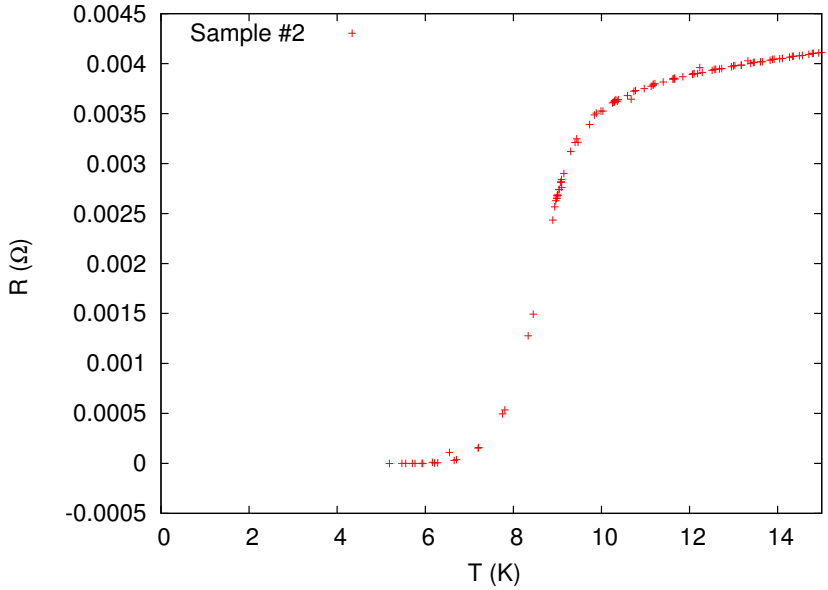

(a)

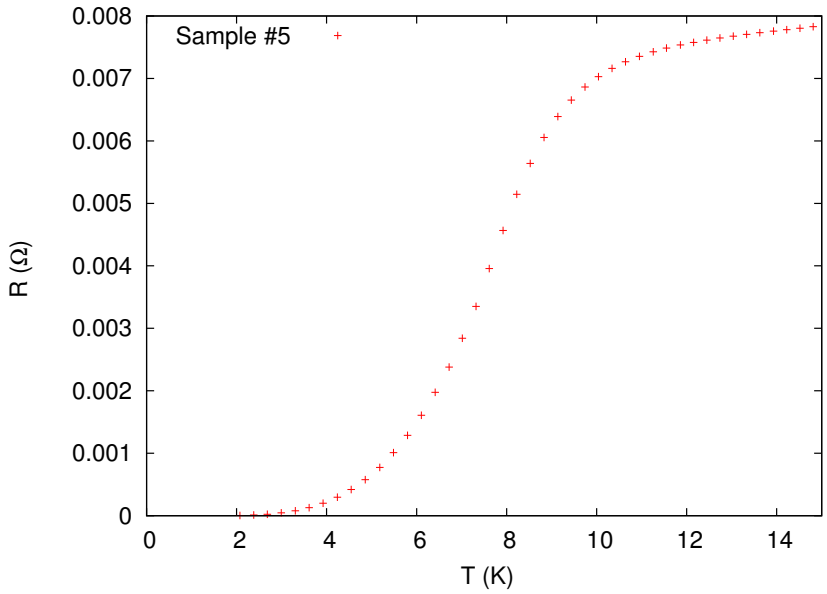

(b)

Fig. 5.21 Resistivity curves in the temperature range from 1.8 to 15 K in samples #2 (top) and #5 (bottom).

and composition mapping while in the particles size measurements (Fig. 5.23) a magnification of 7 k× was needed.

In Figure 5.22a depicting sample #2 we observe a uniform distribution of particles while in the inside (Fig. 5.22b) that does not happen; instead, many voids are observed between the particles. EDS analysis confirmed the presence of Fe and Se in most observed particles with composition close to 1:1 but particles

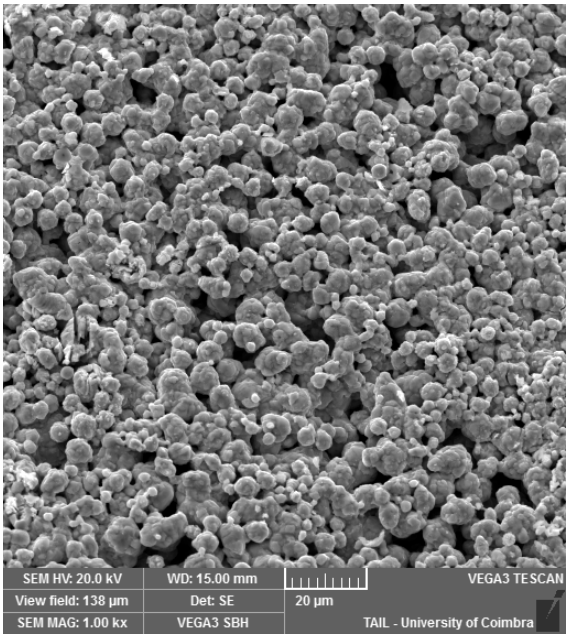

(a)

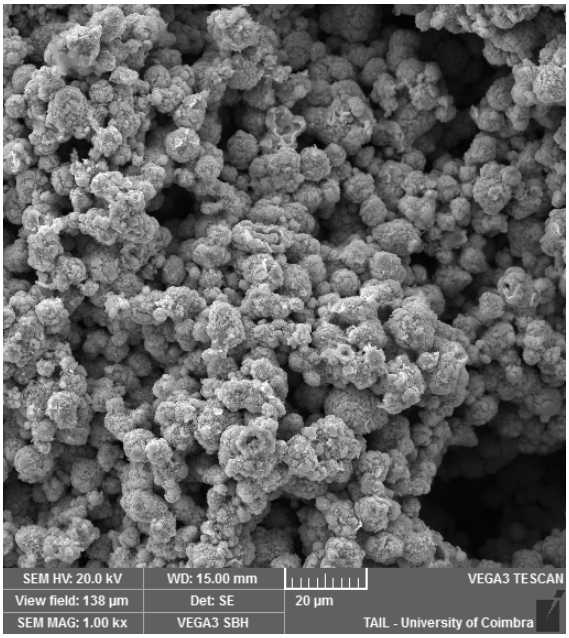

(b)

Fig. 5.22 SEM images of (a) sample #2 at the surface and (b) sample #6 in its inside, taken with a magnification of 1kx.

of free Fe could also be easily found in our samples by this technique. As can be seen in Figures 5.24a and 5.24b obtained by EDS mapping using the Fe and Se Kα lines, samples #1 and #2 have dispersed particles of free α-Fe (green spots) while the others samples do not, which corroborates the XRD results that show a decrease of α-Fe content from sample #1 to #6.

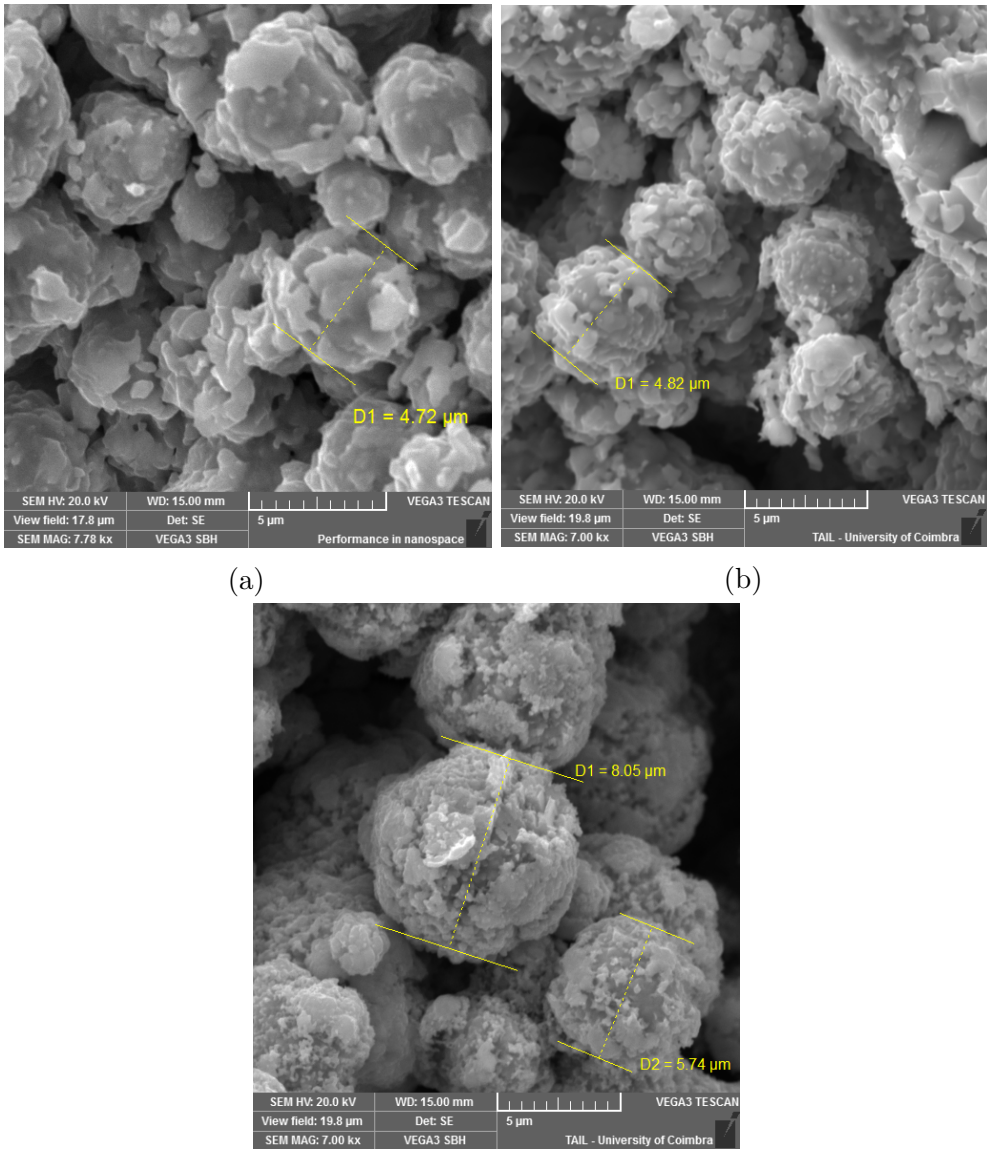

(a) (b)

(c)

Fig. 5.23 SEM images of (a) sample #2 at surface, (b) sample #4 and (c) sample #6 in its inside, showing the size of particles that covers a range from ~ 4 to $\sim 8\,\mu m$.

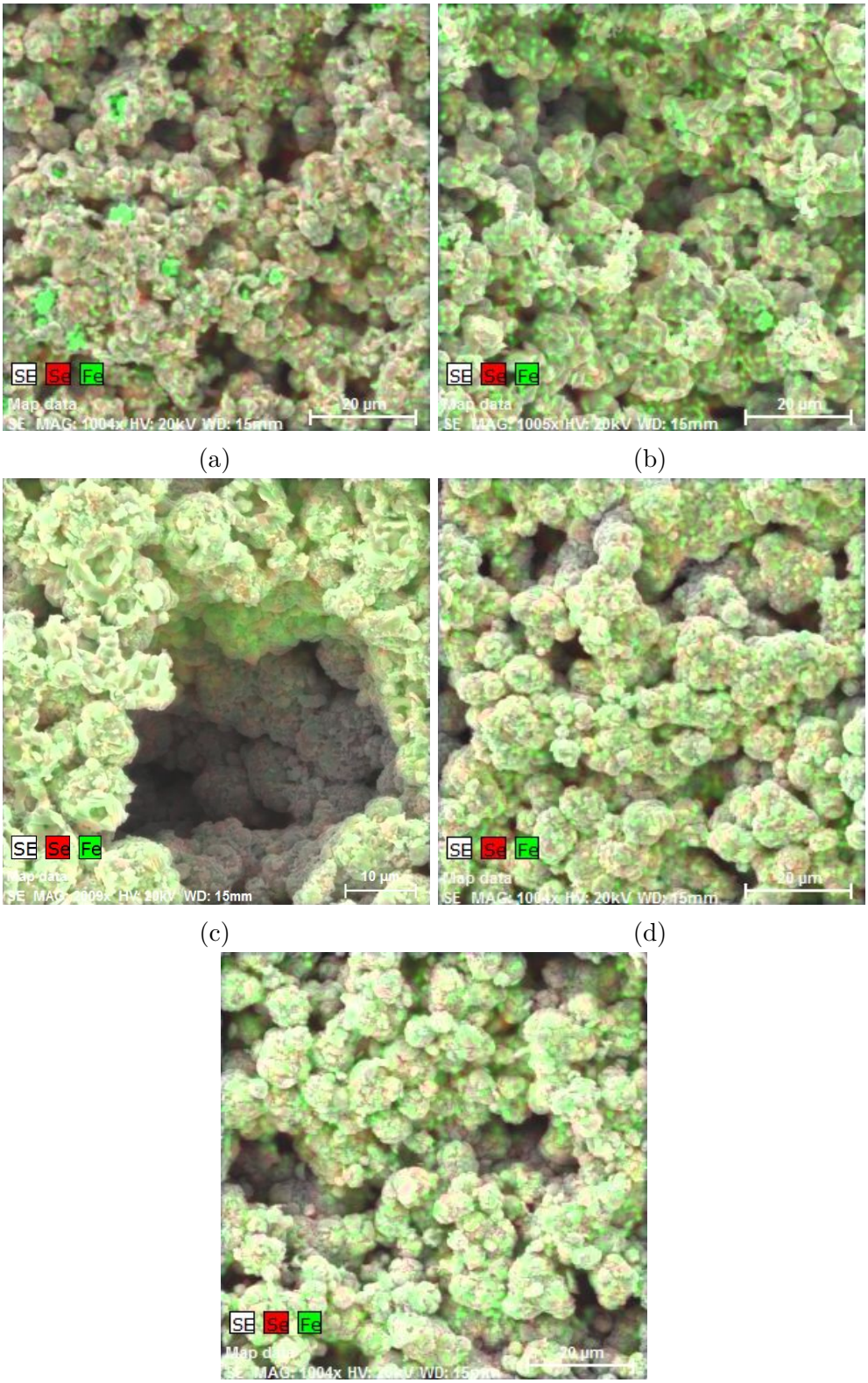

Fig. 5.24 EDS mapping of: (a) sample #1 and (c) sample #4 at its inside; for the other samples, #2, #5 and #6 (with label b, d, e) the mapping was performed at the surface. In sample #4 one can visualise how the particles organise in depth.

5.2.5 Magnetisation measurements

ZFC and FC thermomagnetic curves were measured for the six samples of run #1 in the full temperature range 1.8 to 300 K in an applied magnetic field of 100 Oe. The results for samples #2, #4 and #5 are shown in Figure 5.25.

All samples clearly displayed the Meissner effect. Interestingly, the structural transition occurring at around 100 K in the β-FeSe is clearly seen as an anomaly in the magnetisation in sample #2. The fingerprint of the structural transition broadens as the nominal content of Se increases and the amount of β-phase decreases and that of δ-phase increases, because the δ-phase does not have such structural transition.

Hysteresis cycles up to maximum field of 9 T were measured for a range of temperatures for all samples. In Figure 5.26 the hysteresis cycles at T=130 K are depicted. From these measurements the saturation magnetisation values were extracted and converted to the average atomic moment per formula unit in Bohr magnetons. The results are shown in Figure 5.27. The curve shows a smooth trend of decreasing the moment as the nominal Se content increases. This is expected because the ferromagnetic moment measured in these samples arises, not from the non-magnetic β-FeSe phase, but rather from the ferrimagnetic δ-FeSe phase and from the precipitated free α-Fe.

Compared to the saturation value in α-Fe, 2.2 Bohr magneton per atom, the values of the ferromagnetic component in our samples are compatible, within an experimental error, with assignment of such moment to the free α-Fe impurity. The value measured for the 1:1 nominal composition that is virtually free of free α-Fe should be representative of the induced magnetic moment in the δ-phase. The increase from $0.1\,\mu_B$ per formula unit to $0.3\,\mu_B$ per formula unit agrees well with the estimated percentage of free α-Fe in sample #1, given that a saturated moment per Fe atom is $2.2\,\mu_B$.

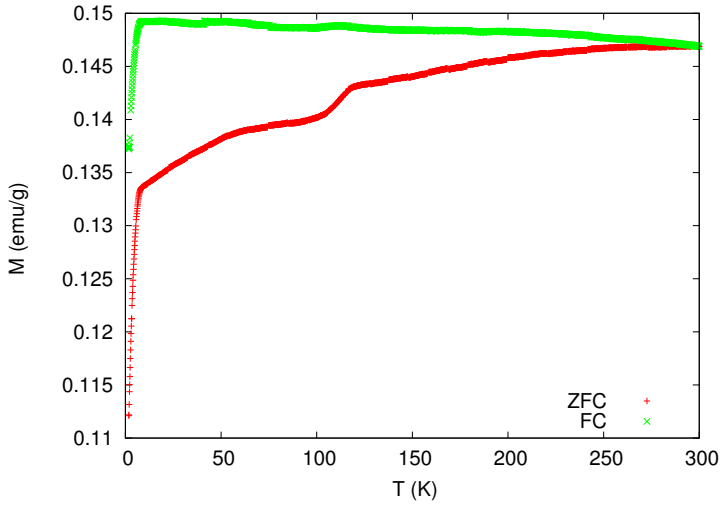

(a)

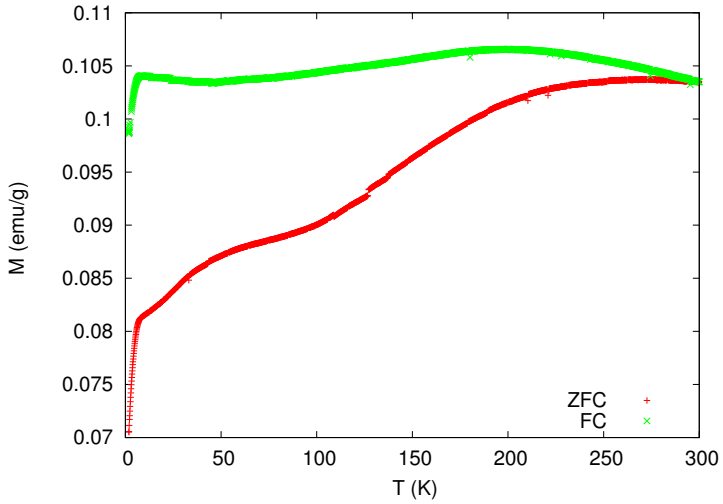

(b)

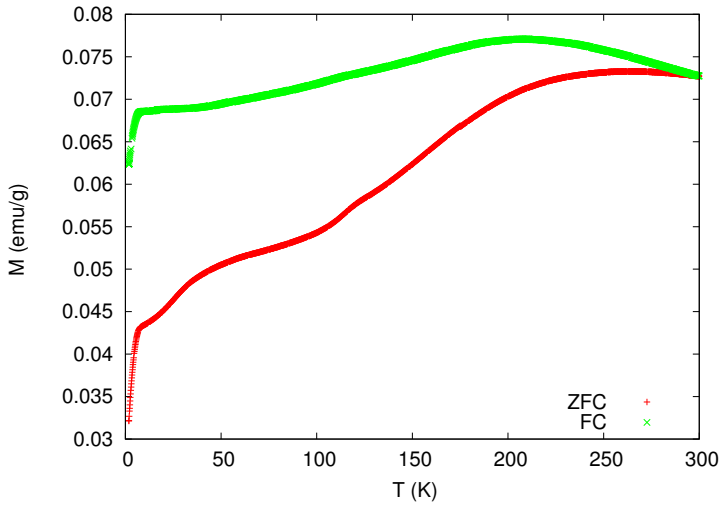

(c)

Fig. 5.25 From top to bottom: ZFC and FC curves for samples #2, #4 and #5 of run #1.

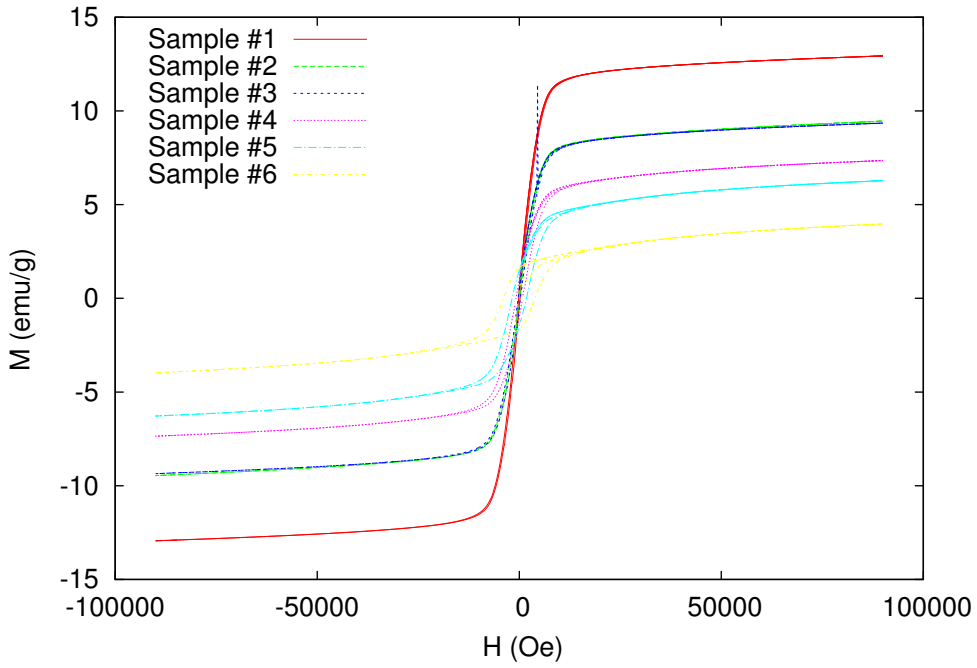

Fig. 5.26 Full hysteresis cycles of samples #1 to #6 of run #1, measured at 130 K.

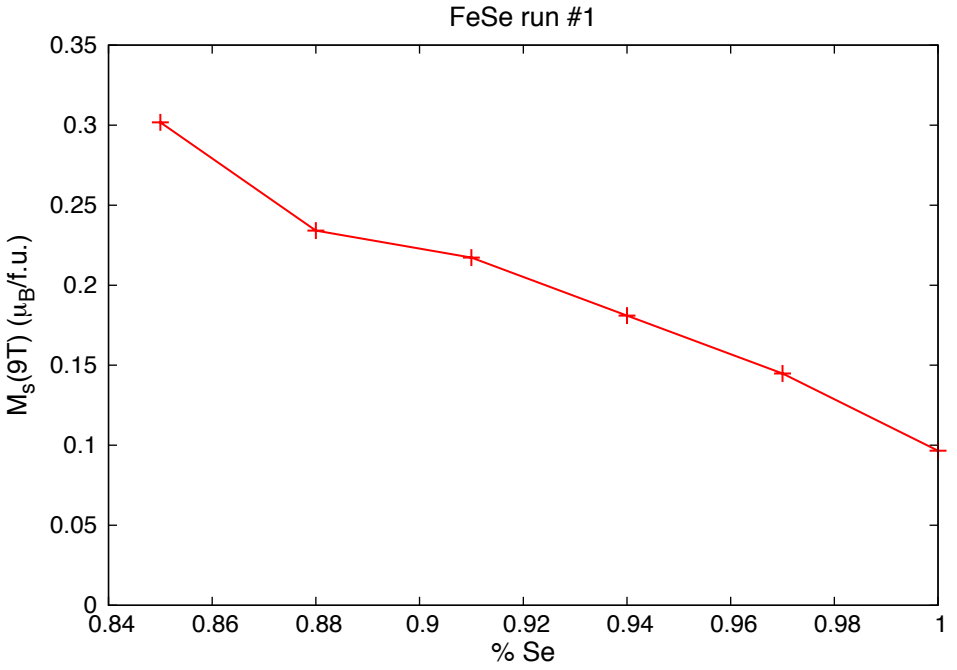

Fig. 5.27 Saturation magnetic moment in μ_B per formula unit of samples #1 to #6 of run #1.

5.3 Results from sample annealing

In the literature it is sometimes prescribed to perform an extended annealing of polycrystalline FeSe samples to improve their quality. Therefore we have annealed the batch of samples from run #1 as described previously. We present now the results we obtained.

5.3.1 XRD analysis

The XRD data shows unambiguously that annealing did not improve the quality of our samples; on the contrary not only the content of the β-phase decreased in all cases (Table 5.4) but also a number of additional parasitic phases showed up (Fig. 5.28 - 5.30) in the XRD patterns, mainly the ferrimagnetic Fe_7Se_8 , Fe_3Se_4, magnetite (Fe_3O_4) and fayalite (Fe_2SiO_4) (Table 5.5). The appearance of magnetite in samples #2 to #6 could only arise from a contamination from oxygen, either from exposure to air during the short periods that the samples were out of the glovebox for measurements or by a deficient vacuum in the quartz tubes used for annealing. More surprisingly, we detected in samples #2 and #3 a significant amount of the mineral that closely resembles fayalite that could only arise from a reaction with the quartz tube (some tubes used in run #1 were reused for the annealing). From all the phases that were detected, magnetite is the strongest ferromagnet. Additional evidence of the presence of magnetite was found in the VSM measurements.

Table 5.4 Comparison of the β-FeSe phase content of the samples before (run#1) and after (run#2) annealing.

	run #1	run #2
Sample #1	91.18(11)	76.4(3)
Sample #2	91.84(13)	41.9(3)
Sample #3	89.78(11)	27.6(3)
Sample #4	84.97(11)	40.4(3)
Sample #5	76.40(13)	15.0(3)
Sample #6	75.03(13)	1.10(13)

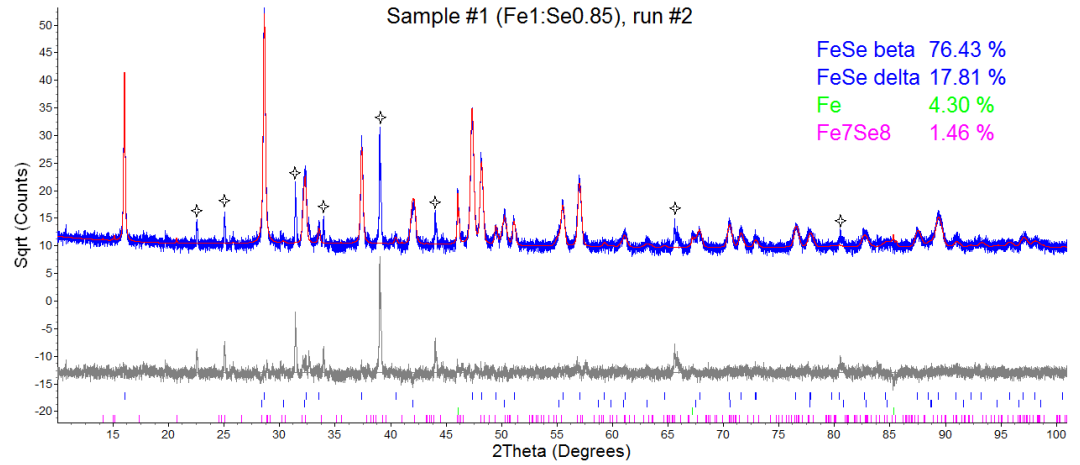

(a)

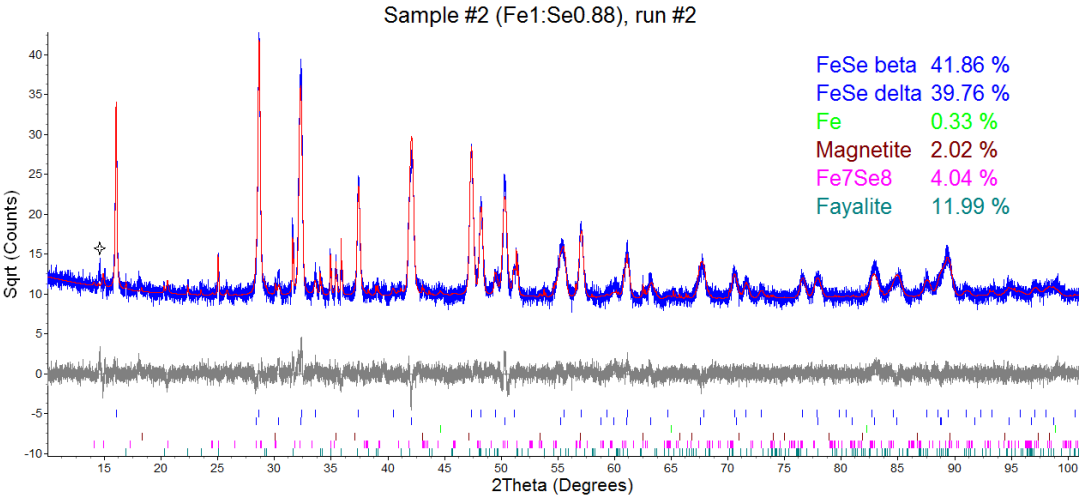

(b)

Fig. 5.28 Diffraction patterns of samples #1 and #2, showing the phases and respective percentage determined by the Rietveld method (run #2).

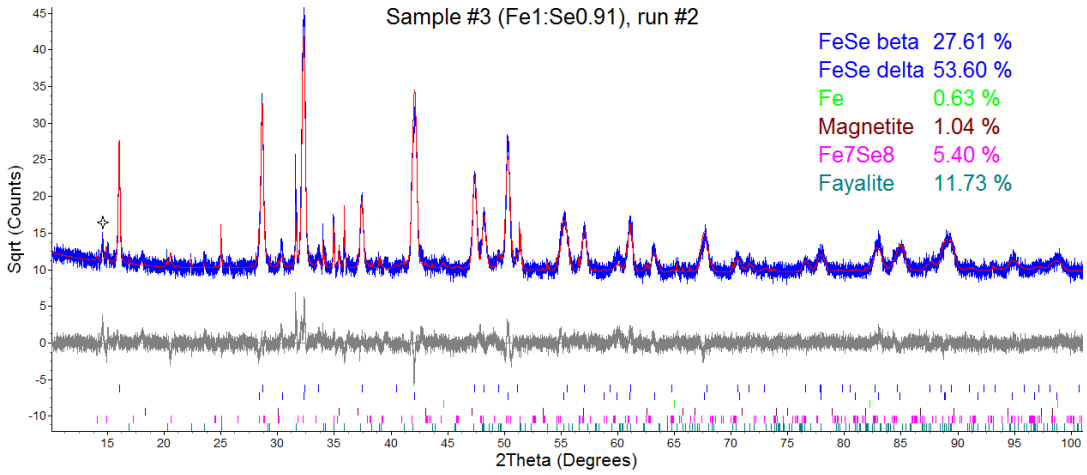

(a)

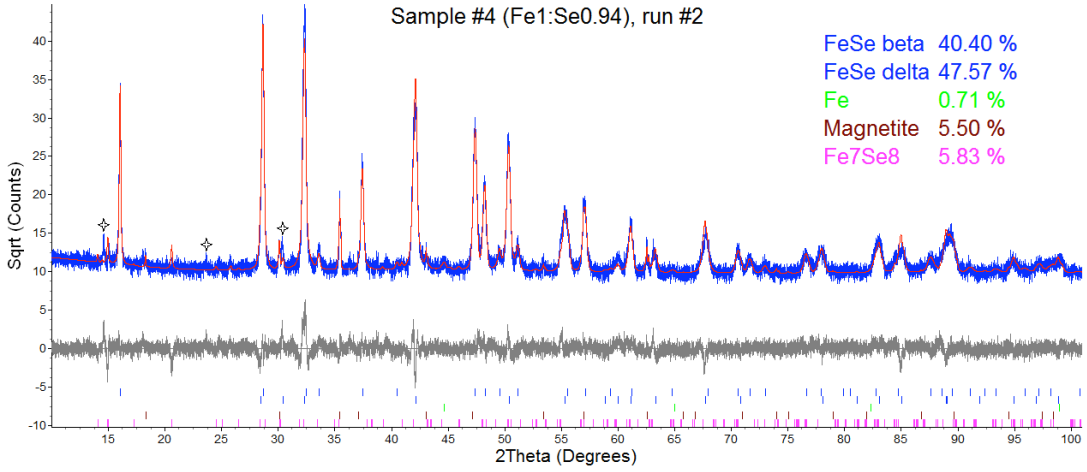

(b)

Fig. 5.29 Diffraction patterns of samples #3 and #4, showing the phases and respective percentage determined by the Rietveld method (run #2).

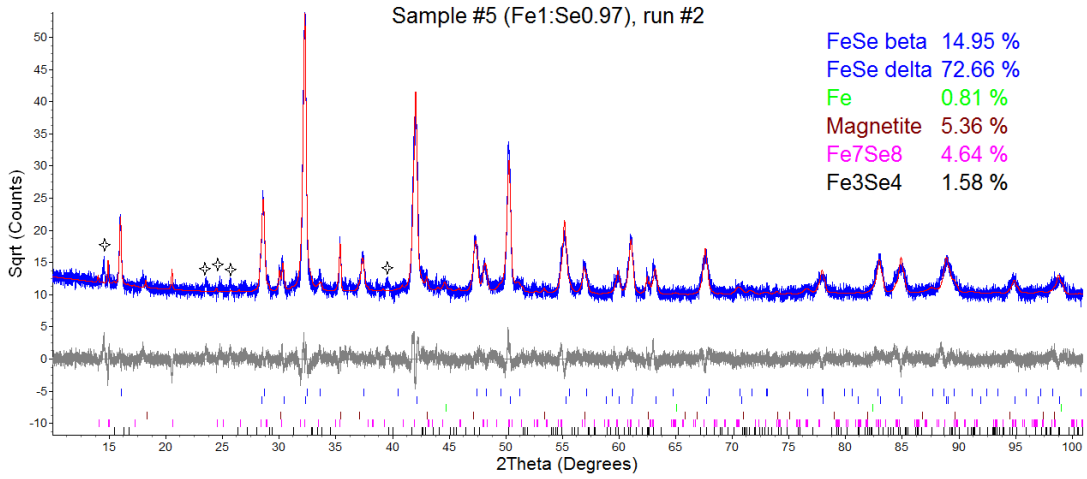

(a)

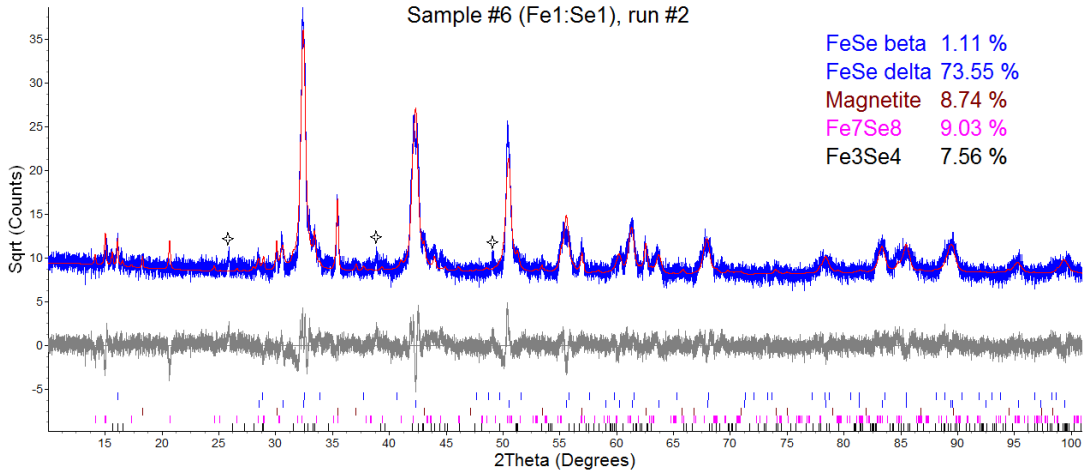

(b)

Fig. 5.30 Diffraction patterns of samples #5 and #6, showing the phases and respective percentage determined by the Rietveld method (run #2).

Table 5.5 Brief summary of the results from the Rietveld refinement of the XRD data for sample #1 to #6, run #2.

Nom. comp.	sample #1 Fe1:Se0.85	sample #2 Fe1:Se0.88	sample #3 Fe1:Se0.91	sample #4 Fe1:Se0.94	sample #5 Fe1:Se0.97	sample #6 Fe1:Se1
β-FeSe (%)	76.4(3)	41.9(3)	27.6(3)	40.4(3)	15.0(3)	1.10(13)
δ-FeSe (%)	17.8(3)	39.8(2)	56.3(3)	47.6(3)	72.7(4)	73.6(1)
α-Fe (%)	4.30(11)	0.33(8)	0.63(10)	0.71(10)	0.81(9)	–
Fe_7Se_8 (%)	1.46(6)	4.0(2)	5.4(2)	5.8(2)	4.6(2)	9.0(3)
Fe_3Se_4 (%)	–	–	–	–	1.58(14)	7.6(3)
Magnetite (%)	–	2.02(9)	1.04(8)	5.50(11)	5.36(13)	8.7(2)
Fayalite (%)	–	11.99(18)	11.73(18)	–	–	–
R_{wp} (%)	14.41	10.65	11.49	11.69	11.72	14.68

5.3.2 Resistivity

In Figure 5.31 we show the results of the resistivity measurements on samples #4 to #6 (samples #1 to #3 had similar results to those of samples #4 and #5). It shows that the amount of the β-phase is insufficient in these samples to percolate the superconducting current throughout the polycrystalline grains. Thus, even if a decrease of the resistivity below T_c can be detected in samples #4 and #5, the resistivity does not attain the zero value, down to 1.8 K.

5.3.3 Magnetisation measurements

The ZFC and FC curves for samples #1 and #6 (samples #2 to #5 had similar behaviour to the one from sample #6) are depicted in Figure 5.32. Sample #1 with 75% of β-phase displays Meissner behaviour below 8 K. In addition, we find an anomaly in the magnetisation in the temperature range from ~ 80 K to ~ 110 K that has been observed by other researchers in samples contaminated with Fe_7Se_8. Interestingly, this anomaly is of different sign in the ZFC and FC curves. Figure 5.32b shows a typical behaviour of magnetite, with an anomaly due to the Verwey transition, occurring at 126 K.

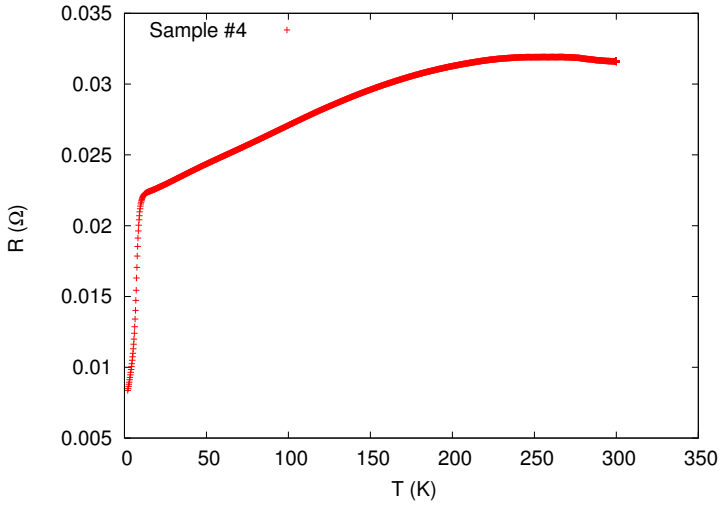

(a)

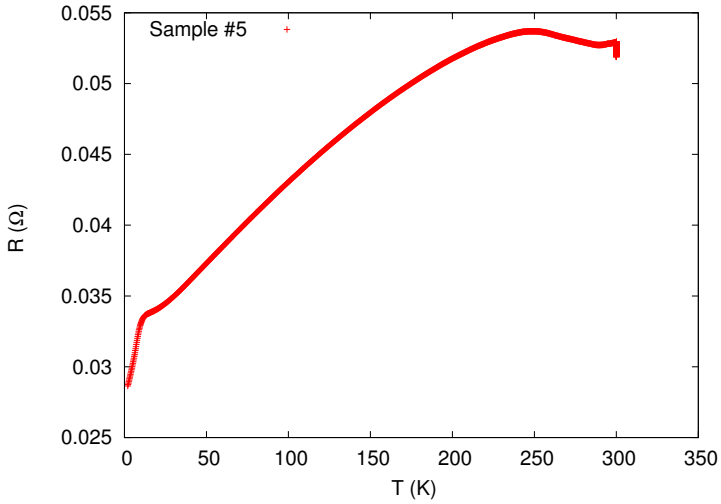

(b)

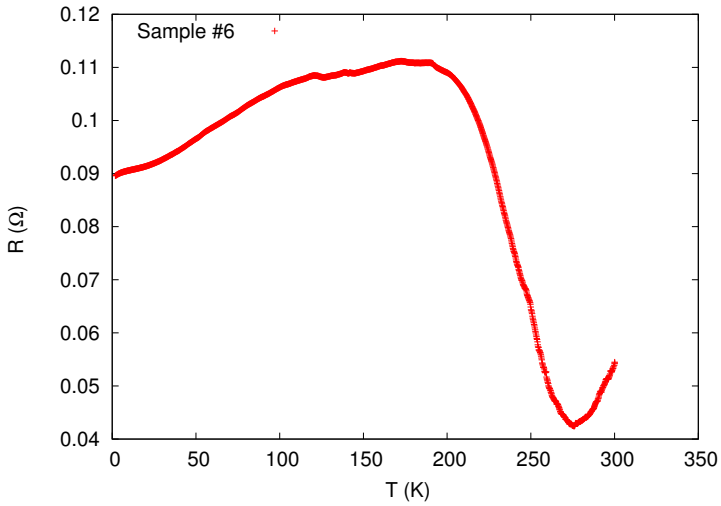

(c)

Fig. 5.31 From top to bottom: Resistivity measurements on samples #4, #5 and #6, run#2.

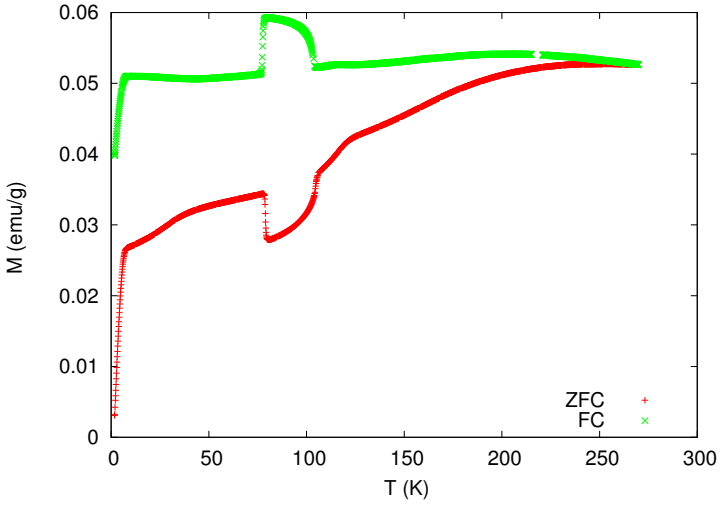

(a)

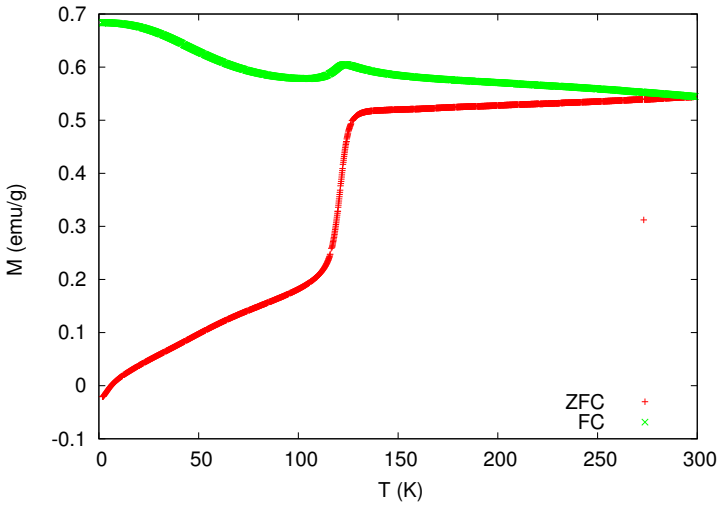

(b)

Fig. 5.32 From top to bottom: ZFC and FC curves of samples #1 and #6 after annealing, run #2.

Chapter 6

Conclusions and future work

We have successfully attained our goal of synthesising good quality superconducting samples of FeSe through a solid-state synthesis route starting from pure elements. These samples are produced in polycrystalline form and, as reported in the literature, always suffer from at least minor contamination from impurity phases, mainly the non-superconducting δ-FeSe, unreacted α-Fe or Se-rich Fe_3Se_4 or Fe_7Se_8 phases. However, choosing carefully the nominal starting composition of the mixture and temperature profiles of the heating and cooling cycles, it is possible to obtain samples that contain in excess of 90% of the desired superconducting β-FeSe phase. Similarly to what has been found by other researches in this field, it is advantageous to start with a composition slightly deficient in Se, the best values being around $Fe : Se_{0.88}$ composition. In this case, we end up with $\sim 6\%$ of non-superconducting δ-FeSe and the excess Fe shows up as $\sim 2\%$ of free α-Fe dispersed in the polycrystalline sample matrix. Contrarily to what is often cited in the literature, neither the β- or δ-phases have a significant amount of Se vacancies in the structure, that is, the stoichiometry of the FeSe phases are close to 1:1 exact stoichiometry, as shown by the refinement of XRD data that give full occupancies to atomic sites in the crystal structure. Our findings are corroborated by detailed studies of site occupancies in β-FeSe performed by neutron scattering in polycrystalline samples and synchrotron radiation studies in single crystals. The advantage of starting from a Se deficient composition is that we preclude the formation of a larger fraction of the δ-FeSe phase that is unavoidable if we start from the exact 1:1 stoichiometry.

Another major conclusion of our work is that even the samples that have been produced with 1:1 nominal composition are superconducting with a T_c that does not differ much from the samples produced starting from the optimal composition. In fact, such 1:1 samples that feature a major portion of δ-FeSe

but virtually no free α-Fe show clearly the Meissner effect and $M(H)$ hystereses cycles in the superconducting phase that have an hysteretic behaviour typical of a hard type-II superconductor well described by the Bean's critical state model. The H_{c1} magnetic field extrapolated to 0 K is 330 Oe. Such hysteretic behaviour occurs due to flux pinning of the vortices in bulk and surface defects. The inert δ-FeSe matrix, even if non-superconducting, plays its role in precluding the motion of the vortices in the Shubnikov phase under applied field. In that sense the presence of δ-FeSe phase is not detrimental but rather beneficial to superconducting properties. On the other hand, those phases with a highest percentage of β-FeSe phase do not display the Meissner behaviour in the $M(H)$ curves because the strong magnetic signal from the ferromagnetic free α-Fe impurity overshadows the diamagnetic signal of the superconducting β-FeSe phase. Therefore, based only on the $M(H)$ curves, these otherwise good samples would have been discarded as non-superconducting.

An issue that is often discussed in the literature is the stability of the FeSe phases, both as ageing in inert atmosphere or when exposed to air. We have found that after one month exposure to air, oxides started to form but are present still in minor quantities. However, the β-FeSe phase slowly converts to free α-Fe, which is surprising.

Concerning suggestions for future work there are clearly some ideas to further develop this new field of iron-based superconductivity at CFisUC. One direction would be to proceed to the synthesis of single crystals. Large crystals would demand new type of equipment but other routes are available such as sol-gel synthesis or microwave synthesis that have been shown to afford small crystals of nano and micro size.

The separation of the different phases from the β-FeSe phase is also a possibility, by the use of a strong magnet which would attract the magnetic phases, leaving only the β-FeSe. The efficiency of such a simple process to remove the magnetic impurities has not been tested but should work at some extent if the material is finely ground.

Last, but not least, the recent exciting reports of high-T_c superconductivity with $T_c = 100$ K in a single layer FeSe deposited on a $SrTiO_3$ substract as well as the proximity effect in a layer of FeSe on top of topological insulators is another interesting subject to be developed.

References

[1] Kamihara, Y. et al. Iron-Based Layered Superconductor: LaOFeP. *Journal of the American Chemical Society*, 128(31):10012–10013, 2006.

[2] Kamihara, Y. et al. Iron-Based Layered Superconductor $La[O_{1-x}F_x]FeAs$ ($x = 0.05 - 0.12$) with $T_c = 26\,K$. *Journal of the American Chemical Society*, 130(11):3296–3297, 2008.

[3] Zhi-An, R. et al. Superconductivity at 55 K in Iron-Based F-Doped Layered Quaternary Compound $Sm[O_{1-x}F_x]FeAs$. *Chinese Physics Letters*, 25(6):2215, 2008.

[4] Rotter, M., Tegel, M., and Johrendt, D. Superconductivity at 38 K in the Iron Arsenide $(Ba_{1-x}K_x)Fe_2As_2$. *Phys. Rev. Lett.*, 101:107006, 2008.

[5] Huiqian, L. et al. Growth and characterization of $(A_{1-x}K_x)Fe_2As_2$(A = Ba, Sr) single crystals with $x = 0 - 0.4$. *Superconductor Science and Technology*, 21(12):125014, 2008.

[6] Tapp, J. H. et al. LiFeAs: An intrinsic FeAs-based superconductor with $T_c = 18\,K$. *Phys. Rev. B*, 78:060505, 2008.

[7] Hsu, F.-C. et al. Superconductivity in the PbO-type structure $\alpha -$ FeSe. *Proceedings of the National Academy of Sciences*, 105(38):14262–14264, 2008.

[8] Khasanov, R. and Guguchia, Z. Probing the multi gap behavior within '11' and '122' families of iron based superconductors: the muon-spin rotation studies. *Superconductor Science and Technology*, 28(3):034003, 2015.

[9] Liu, X., Zhao, L., et al. Electronic structure and superconductivity of FeSe-related superconductors. *Journal of Physics: Condensed Matter*, 27(18):183201, 2015.

[10] McQueen, T. M., Huang, Q., et al. Extreme sensitivity of superconductivity to stoichiometry in $Fe_{1+\delta}Se$. *Physical Review B*, 79:014522, 2009.

[11] McQueen, T. M., Williams, A. J., et al. Tetragonal-to-Orthorhombic Structural Phase Transition at 90 K in the Superconductor $Fe_{1.01}Se$. *Physical Review Letters*, 103:057002, 2009.

[12] Lin, J.-Y., Hsieh, H. S., et al. Coexistence of isotropic and extended s-wave order parameters in FeSe as revealed by low-temperature specific heat. *Phys. Rev. B*, 84:220507(R), 2011.

[13] Medvedev, S., McQueen, T. M., et al. Electronic and magnetic phase diagram of $\beta - Fe_{1.01}Se$ with superconductivity at 36.7 K under pressure. *Nature Materials*, 8:630–633, 2009.

[14] Imai, T., Ahilan, K., et al. Why Does Undoped FeSe Become a High-Tc Superconductor under Pressure? *Phys. Rev. Lett.*, 102:177005, 2009.

[15] Chang, C.-C., Wang, C.-H., et al. Superconductivity in PbO-type tetragonal FeSe nanoparticles. *Solid State Commun.*, 152(8):649–652, 2012.

[16] Ge, J.-F., Liu, Z.-L., et al. Superconductivity above 100 K in single-layer FeSe films on doped $SrTiO_3$. *Nature Materials*, 14:285–289, 2015.

[17] Guo, J., Jin, S., et al. Superconductivity in the iron selenide $K_xFe_2Se_2$. *Phys. Rev. B*, 82:180520(R), 2010.

[18] Onar, K. and Yakinci, M. E. Solid state synthesis and characterization of bulk β-FeSe superconductors. *Journal of Alloys and Compounds*, 620(4):210–216, 2015.

[19] Júnior, J. L. P., Serbena, F. C., and Jurelo, A. R. Characterization of $FeSe_x$ superconductor prepared by different thermal routes by instrumented indentation. *Journal of Superconductivity and Novel Magnetism*, 24(5):1437–1441, 2011.

[20] Pomjakushina, E., Conder, K., Pomjakushin, V., Bendele, M., and Khasanov, R. Synthesis, crystal structure, and chemical stability of the superconductor $FeSe_{1-x}$. *Phys. Rev. B*, 80(2):024517, 2009.

[21] Okamoto, H. The Fe-Se (iron-selenium) system. *Journal of Phase Equilibria*, 12:383, 1991.

[22] Grivel, J.-C., Wulff, A. C., Zhao, Y., Andersen, N. H., Bednarcak, J., and v Zimmermann, M. *Insitu* observation of the formation of FeSe. *Superconductor Science and Technology*, 24(1):015007, 2011.

[23] Sefat, A. S. Bulk synthesis of iron-based superconductors. *Current Opinion in Solid State and Materials Science*, 17(2):59–64, 2013.

[24] Clearfield, A. et al. *Principles and Applications of Powder Diffraction.* John Wiley & Sons, Ltd, 1st edition, 2008.

[25] Pecharsky, V. and Zavalij, P. *X-ray diffraction by polycrystalline materials.* Springer US, 2nd edition, 2009.

[26] NanoPhysics B.V. http://www.nanophysics.nl/Services/semedx.html, n.d.

[27] Goldstein, J. et al. *Scanning electron microscopy and x-ray microanalysis.* Springer US, 3rd edition, 2003.

[28] Frank Krumeich. Properties of Electrons, their Interactions with Matter and Applications in Electron Microscopy. http://www.microscopy.ethz.ch/downloads/Interactions.pdf, n.d.

[29] Bruker Nano GmbH. Bruker QUANTAX EDS Reference Manual, *Introduction to EDS analysis*, 2011.

[30] TESCAN. Scanning Electron Microscope VEGA 3 SEM,*Instructions for use*, 2011.

[31] Quantum Design. DynaCool^{TM}User's Manual, *Physical Property Measurement System®*, 4th edition, 2014.

[32] Scofield, J. H. Four probe resistance primer. http://pec.sjtu.edu.cn/ols/DocumentLib/synthesis/072013010/unprotected-four-probe.pdf, 2000.

[33] Quantum Design Applications Newsletter. Six Things to Consider when Making Electrical Transport Measurements. http://www.qdusa.com/sitedocs/newsletters/Applications_Newsletter_Fall_2013.pdf, Fall 2013.

[34] Quantum Design PPMS Application Notes. Cause and Effects of Common-Mode Leakthrough. http://http://www.qdusa.com/sitedocs/appNotes/ppms/1584-201.pdf, 2000.

[35] Foner, S. Versatile and Sensitive Vibrating-Sample Magnetometer. *Review of Scientific Instruments*, 30(7):548–557, 1959.

[36] Zieba, A. and Foner, S. Detection coil, sensitivity function, and sample geometry effects for vibrating sample magnetometers. *Review of Scientific Instruments*, 53(9):1344–1354, 1982.

[37] Quantum Design Applications Newsletter. How to Get the Most Out of Your Quantum Design VSM. http://www.qdusa.com/sitedocs/newsletters/Applications_Newsletter_Fall_2014.pdf, Fall 2014.

[38] Cheary, R. W. and Coelho, A. A. A fundamental parameters approach to X-ray line-profile fitting. *J. Appl. Cryst.*, 25:109–121, 1992.

[39] Hu, R., Lei, H., et al. Synthesis, crystal structure and magnetism of $\beta - Fe_{1.00(2)}Se_{1.00(3)}$ single crystals. *Phys. Rev. B*, 83:224502, 2011.

[40] Hirone, T. and Chiba, S. The Magnetic Properties of $FeSe_x$ with the NiAs Structure. *Journal of the Physical Society of Japan*, 11(6):666–670, 1956.

[41] Bean, C. P. Magnetization of Hard Superconductors. *Phys. Rev. Lett.*, 8:250, 1962.

Appendix A

STUDY OF THE PHASE DIAGRAM OF FeSe SUPERCONDUCTORS

M. S. C. Henriques,* J. A. Paixão
CEMDRX, Departament of Physics, University of Coimbra
*marta.henriques@gmail.com

INTRODUCTION

The discovery of superconductivity in Fe-based compounds [1] breaks the conventional wisdom that Fe atoms are detrimental to superconductivity. Among the Fe-based compounds, the tetragonal PbO type β-$FeSe_{1-x}$ has the simplest structure and is ideal to investigate the origin of superconductivity in these compounds. Unfortunately, the phase diagram of FeSe is somewhat complex and the superconducting properties are sensitive to minor deviations from the optimal stoichiometry ($x \sim 0.12$) and it is difficult to avoid the presence of other non-superconducting phases, namely the hexagonal α-FeSe phase during the synthesis of the superconducting compound [2].

METHOD

To investigate the phase diagram, several synthesis conditions were tested, starting from the pure elements, with different heating and cooling cycles, aiming to produce single-phase β-$FeSe_{1-x}$. The different phases were identified by XRD using a Bruker D8 Advance diffractometer with Ni-filtered Cu K_α radiation. Composition and stoichiometry of the phases were determined from Rietveld refinements. The superconducting and magnetic properties were measured by AC resistivity and VSM magnetometry performed with a cryogen-free physical property measurement system (Dynacool, Quantum Design). The results of two samples will be presented in detail (samples # 2 and #4).

RESULTS - RESISTIVITY

AC resistivity measurements confirm our samples are superconducting. Sample #2 has a higher transition temperature ($T_{onset} = 9.0\,K$, $T_0 = 7.5\,K$). The resistivity curve shows signs of two other transitions, in addition to the superconducting one, at 27 K and 120 K, detected as a sharp and a broad peaks, respectively, in $d\rho(T)/dT$. The latter is probably a signature of the structural transition occurring in the α-phase around this temperature.

Sample #2 ($x = 0.12$)

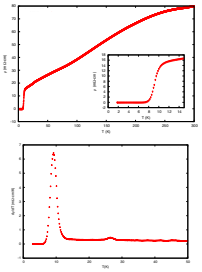

Figure 4. Temperature-dependence of resistivity (top). The insert shows in detail the low-T region. Calculated values of $d\rho(T)/dT$ (bottom).

RESULTS - X-RAY DIFFRACTION

Sample #2 ($x = 0.12$) Sample #4 ($x = 0.0$)

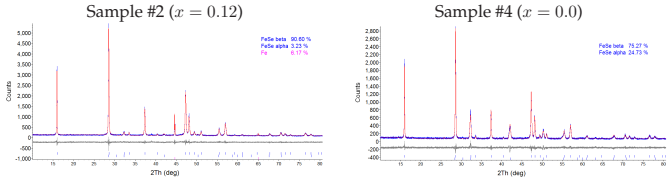

Figure 1. XRD powder diffractograms of two FeSe samples; sample #2 has a high content of β phase and some excess Fe, sample #4 contains a high amount of the parasitic α phase.

RESULTS - MAGNETOMETRY 1

Sample #2 ($x = 0.12$) Sample #4 ($x = 0.0$)

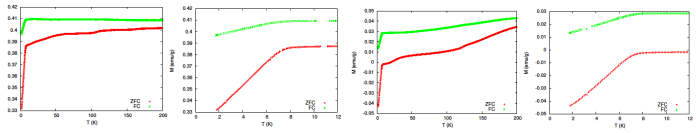

Figure 2. Temperature-dependence of magnetization for an applied field $H = 100\,Oe$. In addition to the diamagnetic signal at the onset of superconductivity, an anomaly at $\sim$ 100 K is seen, as a signature the low-temperature structural phase transition.

RESULTS - MAGNETOMETRY 2

Sample #2 ($x = 0.12$) Sample #4 ($x = 0.0$)

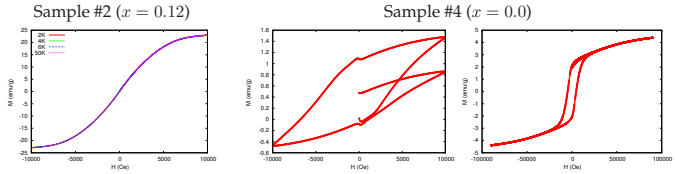

Figure 3. Sample #2 shows a high magnetization and a soft magnetic behaviour, arising mainly from the small amount of free Fe; sample #4 has ferrimagnetic behaviour arising from the α phase (left: 1.8K, low field; right: 100K.)

RESULTS - MAGNETOMETRY 3

$M(H)$ cycles enabled the determination of the critical field $Hc_1(T)$. T_c for sample #4, determined from the fit of $Hc_1(T)$ law is 7.1 K, a lower value than T_c of sample #2.

Sample #4 ($x = 0.0$)

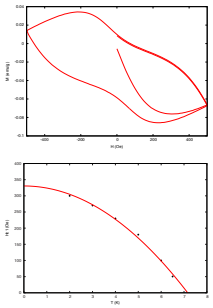

Figure 5. $M(H)$ at 1.8 K (top) and T-dependence of critical field Hc_1 (bottom).

[1] F.-C. Hsu, *et al.*, *Proc.Natl.Acad.Sci.* 105, 2008, 14262-14264.
[2] H. Okamoto, *J. Phase Equilib.*, 12, 1991, 383-389.

CONCLUSIONS

Our study of the Fe/Se phase diagram shows that stoichiometry of the starting mixture of the elements as well as the heating and cooling cycles during the synthesis are crucial to maximize the amount of the superconducting β-phase; the critical temperature is sensitive to both exact stoichiometry and the presence of small amounts of extraneous phases. A slight deficiency of Se in $FeSe_{1-x}$, $x \sim 0.12 - 0.15$ is required to obtain the best superconducting samples.

ACKNOWLEDGEMENTS

This work was supported by funds from FEDER (Programa Operacional Factores de Competitividade COMPETE) and from FCT-Fundação para a Ciência e Tecnologia under the project PEst-C/FIS/UI0036/2014. Access to TAIL-UC facility funded under QREN-Mais Centro Project ICT_2009_02_012_1890 is gratefully acknowledged.

Fig. A.1 Poster presented at the 41st Conference on Phase Equilibria, Coimbra.